Convective Power Loss Measurements in a Field Reversed Configuration with Rotating Magnetic Field Current Drive

Paul Melnik

A dissertation

submitted in partial fulfillment of the

requirements for the degree of

Doctor of Philosophy

University of Washington

2014

Reading Committee:

Alan L. Hoffman, Chair

Richard D. Milroy

Brian A. Nelson

Program Authorized to Offer Degree:

Department of Aeronautics and Astronautics

University of Washington

Abstract

Convective Power Loss Measurements in a Field Reversed Configuration with Rotating Magnetic Field Current Drive

Paul Melnik

Chair of the Supervisory Committee:
Professor Alan L. Hoffman
Department of Aeronautics and Astronautics

The Translation, Confinement, and Sustainment Upgrade (TCSU) experiment achieves direct formation and sustainment of a field reversed configuration (FRC) plasma through rotating magnetic fields (RMF). The pre-ionized gas necessary for FRC formation is supplied by a magnetized cascade arc source that has been developed for TCSU. To ensure ideal FRC performance, the condition of the vacuum chamber prior to RMF start-up has been characterized with the use of a fast response ion gauge. A circuit capable of gating the puff valves with initial high voltage for quick response and then indefinite operational voltage was also designed. A fully translatable combination Langmuir / Mach probe was also built to measure the electron temperature, electron density, and ion velocity of the FRC. These measurements were also successfully completed in the FRC exhaust jets allowing for an accurate analysis of the FRC power loss through convection.

TABLE OF CONTENTS

Page

ACKNOWLEDGEMENTS

I would first like to thank my wife Jane Kuramoto Melnik and my mother Louise Melnik for their continued support during my studies. This dissertation would not have been possible without the guidance and patience of my graduate advisor Prof. Alan Hoffman, and Prof. Richard Milroy whose insight has been invaluable. My sincerest thanks goes out to the entire RPPL staff whose knowledge and expertise made the TCSU experiment a success and this dissertation a reality. To George Vlases for helping understand the most complex problems and to Bob Brooks who can solve any challenge no matter how daunting. Houyang Guo and James Grossnickle for helping me operate the machine. To Kennith Miller for helping simplify difficult engineering designs. Terry Dehart and Dan Lotz without whom the combination probe would not have been possible. Jon Hayward, Scott Kimball, Matthew Fishburn, and Mike Dellinger are all experts at what they do and kept the TCSU experiment running. I would also like to thank Dennis Peterson and Dzung Tran at the Guggenheim machine shop who can make complicated designs a reality and are quick to spot potential improvements. And a special thanks goes out to George Votroubek, Chris Deards, Kiyong Lee, Aydin Tankut, and Katherine Velas who have made RPPL the great place that it was.

Chapter I: Introduction to Plasma Confinement and the TCSU Experiment

1.1 Introduction

Thermonuclear fusion will potentially be the Earth's energy source of the future. Fusion of the hydrogen isotopes, deuterium and tritium, has the lowest ignition temperature which means it requires the lowest amount of input energy for a reaction to occur. Hydrogen in the most abundant element in the universe and it is very plentiful on Earth so the typical fusion reactants will always be available and in almost limitless quantities. For a D-T fusion reaction to occur a deuterium ion must collide with a tritium ion with enough energy to overcome their electrostatic repulsion. The P-P solar fusion chain is the process that powers all of the stars in the universe, including the Sun. The appreciable reaction cross-section in the Sun's core allows for nuclear fusion to occur because an extremely high density of high temperature ions is confined for a long time by gravity. In a terrestrial based fusion experiment we do not have the luxury of gravity to confine the high temperature reactants so magnetic fields are used for steady state confinement.

The most common magnetic confinement fusion concept is the tokamak [1], in which the high temperature, ionized gas called plasma is confined in a torus shape around a central conductor. The plasma in a tokamak is stabilized by a large toroidal magnetic field generated by magnet coils that surround the torus shaped vacuum chamber. The central conductor is a solenoid that is essentially the backbone of the magnetic configuration. The change of magnetic flux in the center solenoid induces a toroidal electric field via Faraday's law which drives the plasma current. The plasma current is responsible for the generation of a poloidal magnetic field that confines the plasma and is necessary for an equilibrium in which the plasma pressure is balanced by the magnetic

forces. The poloidal field is also used to counteract the particle drifts inherent in toroidal plasma geometry. The doubly connected geometry of a tokamak is difficult to design and build and may not be the ideal confinement geometry of fusion plasma. To this end, a range of Innovative Confinement Concepts (ICC) such as the field reversed configuration have been explored.

1.2 The Field Reversed Configuration

1.2.1 FRC Introduction

The simply connected plasma confinement concept known as the field reversed configuration (FRC) consists of an elongated azimuthal current ring confined by an axial magnetic field [2,3]. The cylindrical geometry of the FRC (r,θ,z coordinates) is a major advantage over other magnetic confinement concepts in that there is no vacuum boundary or magnetic field coil linking the hole of the plasma torus. This offers a beneficial reduction in the engineering complexity and constructions costs of the vacuum chamber and magnetic coils. The FRC also has a natural divertor so any particles lost are incorporated into the exhaust jets streaming away from the FRC at both ends. The effect of the natural divertor is advantageous is many ways; simply because the divertor plates can be located far from the FRC or, in a more ambitious, far-reaching sense the exhaust jets could be an ideal space propulsion device.

A schematic of a fully formed FRC is shown in Fig. 1.1. The radius of the flux conserver is given as r_c. The separatrix radius r_s is defined as the radius of the last closed poloidal field line which differentiates the closed field line FRC from the open field lines. The field null radius is denoted as R where $B_z = 0$. The FRC acts to exclude flux which compresses the axial magnetic field from the vacuum value B_o to the excluded value B_e. The initial flux $\Phi_o = \pi r_c^2 B_o$ must equal the excluded flux $\Phi_e = \pi(r_c^2 - r_s^2)B_e$ due to flux conservation. If we define the ratio of the seperatrix radius to flux conserving radius as $x_s = r_s/r_c$ then we can write the external magnetic field in terms of the vacuum field as $B_e = B_o / (1 - x_s^2)$.

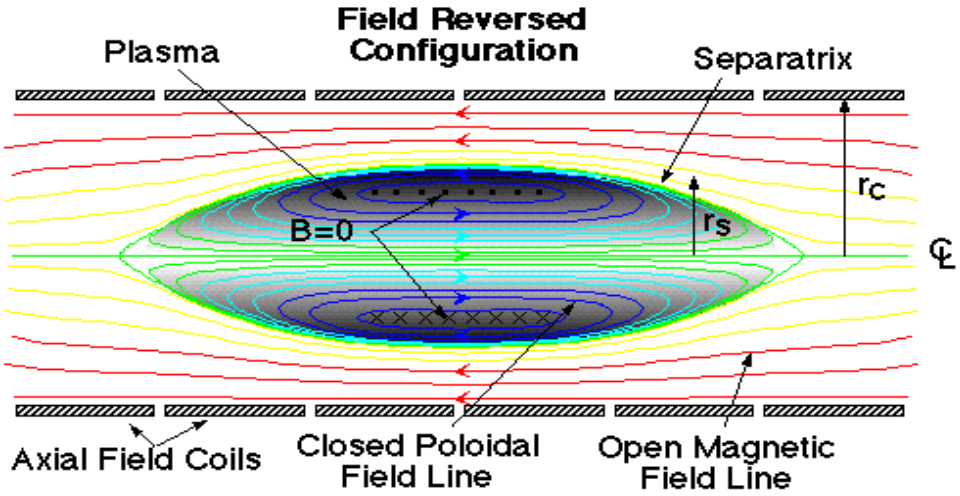

FIG. 1.1 Schematic of the field reversed configuration.

Another advantage of the FRC is an inherently high beta which is the ratio of plasma pressure to magnetic pressure. This is basically a measure of how efficient the applied magnetic field is at confining the plasma pressure. If we assume the FRC is sufficiently elongated so the axial magnetic field lines are straight at the midplane and the flux is constant from the midplane to beyond the end of the FRC then the average beta relation can be expressed by Eq. (1.1).

$$\langle \beta \rangle \equiv \frac{\langle p \rangle}{B_e^2 / 2\mu_o} = 1 - \frac{x_s^2}{2} \tag{1.1}$$

1.2.2 FRTP Formation

At the Redmond Plasma Physics Laboratory (RPPL), FRC formation is accomplished using multiple techniques. The more conventional method is the field reversed theta-pinch (FRTP). A FRC formed in this method starts as a pre-ionized gas in the presence of an axial magnetic field called the bias field. The pre-ionized gas is created from neutral deuterium injected into the vacuum chamber that is excited by nearby radio frequency antennas. This results in a cold plasma that is sufficiently conducting such that it is magnetized by the bias field. At this point the current in the bias field coils is rapidly reversed causing the external magnetic field to change polarity. By Faraday's Law, the change in the axial magnetic field creates a toroidal electric field which drives a current in the theta direction that traps the original bias field. The external magnetic field is increased which compress the plasma current ring until the enclosed reverse bias field lines connect with the external magnetic field lines. The closed poloidal magnetic field lines confine the plasma within. FRC formation by the FRTP method can result in hot, dense plasma with total temperatures of 1 keV and densities on the order of 10^{21} m^{-3} [4].

FRCs formed by the FRTP method are subject to a few limitations. As the poloidal magnetic field lines close the FRC undergoes a violent axial contraction and the resulting plasma is highly sensitive to the symmetry and timing of the formation. As such, FRC repeatability is extremely difficult to attain. Also any plasma formed by FRTP is limited in energy and size by the high voltage and fast switching required as seen in the Large-S Experiment (LSX) [5]. Finally, the plasma current cannot be sustained inductively so the FRC resistively decays away soon after formation.

1.2.3 RMF Formation and Current Drive

Originally proposed by Blevin and Thonemann [6] in 1962, the idea of a transverse rotating magnetic field (RMF) to drive toroidal current has been explored both theoretically and experimentally. Years later at Flinders University extensive experimentation with RMF current drive was done in a spherical device called a rotomak [7]. RMF research continued at RPPL with experiments using cylindrical geometry like the Translation, Confinement, and Sustainment experiment (TCS) [8], and the Star-Thrust experiment (STX) [9].

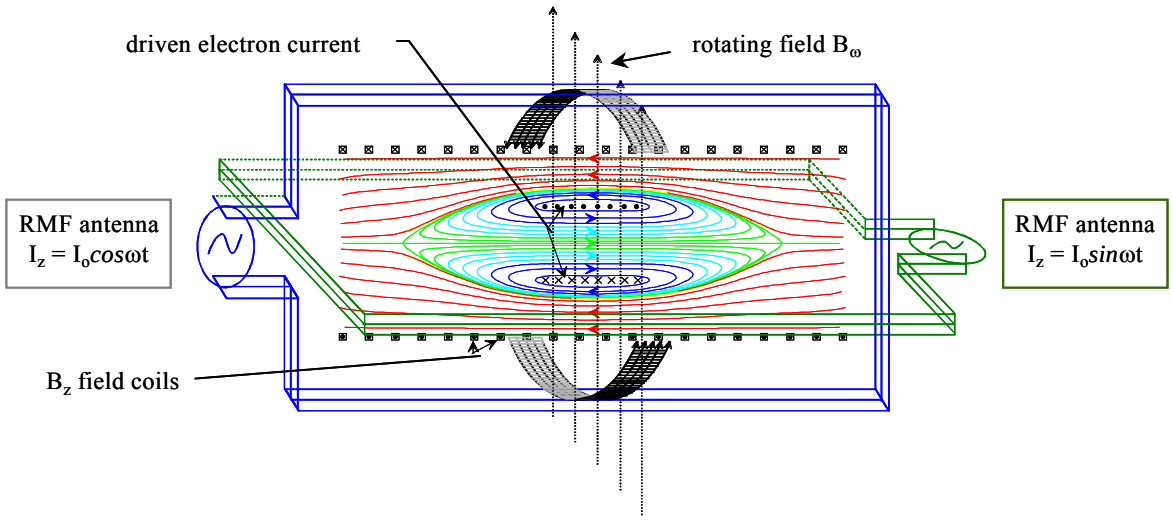

FIG. 1.2 Schematic of the rotating magnetic field antennas

Two sets of RMF antennas are driven at a frequency ω to create a transverse magnetic field outlined in the schematic shown in Fig. 1.2. The field is rotated azimuthally in time by phasing the current in the pair of dipole antennas apart by 90°. The RMF frequency ω is chosen so it is too fast for the ions to respond but slow enough to act on the electrons. This is achieved by the setting the RMF frequency to a value between the cyclotron frequency of each species as such $\omega_{ci} < \omega << \omega_{ce}$. In this way the

electrons are magnetized in the transverse field and thus rotate near synchronously with the RMF. The electron rotation creates an azimuthal current which reverses the applied axial bias field characteristic of an FRC.

The influence of the RMF is strong enough that not only will it sustain the FRC current ring but it can actually create a FRC from a supply of pre-ionized gas in the presence of an axial magnetic field. Direct formation of an FRC relies on a build up of poloidal flux and this can be accomplished if the RMF current drive is greater than the resistive decay of the FRC. This was noticed in the Tokamak Refueling by Accelerated Plasmoids experiments (TRAP) in which an FRC was created by FRTP and translated into the confinement region [10] where the RMF was used to sustain the existing current ring. The early method of operation in the TCS experiment also incorporated FRTP formation but later began direct FRC formation by RMF alone. The injected gas was again pre-ionized using radio frequency antennas until the TCSU experiment was built and the pre-ionized gas was supplied by a magnetized cascade arc source described in Chapter 3.

The RMF antennas are often referred to as horizontal and vertical because each antenna loop is really a cradle that wraps around a part of the quartz TCSU confinement section. The cradles used to create the horizontal RMF are on the sides of the confinement section while the vertical field is created by the cradles on the top and bottom of the machine. An elevated side view of the vertical RMF antenna is shown in Fig. 1.3.

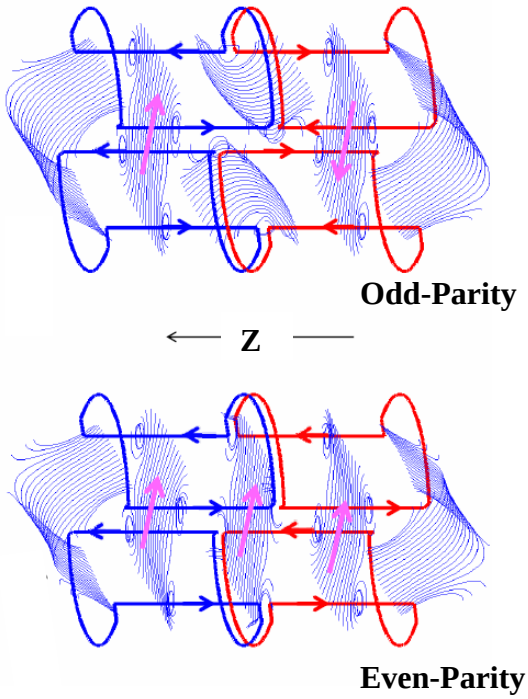

FIG. 1.3 Schematic of the vertical RMF antenna depicting the difference between even and odd parity RMF operation. The sections of the vertical antenna are differentiated by their color.

The horizontal and vertical RMF antennas are also split into two sections so they can be operated in either even-parity or odd-parity mode. Fig. 1.3 also shows each section of the vertical RMF antenna in red and blue. To create the odd-parity rotating magnetic field the sections of an antenna cradle are driven 180° out of phase. In splitting the antennas into sections, a conducting part is now located at the midplane. For even-parity RMF there is no induced magnetic field from the midplane conductor because the current from each antenna section flows in opposite directions. However for odd-parity RMF, the current in the midplane conductor is in the same direction. This induces an oscillating B_z at the midplane which is localized to the vicinity near the FRC seperatrix out to the vacuum chamber wall. The oscillating axial magnetic field is clearly shown in

the odd-parity portion of Fig. 1.3. The drawing in Fig. 1.4 shows the direction of the transverse field created by each RMF antenna section. The details of the midplane conductor are highlighted as well elucidating the oscillating B_z.

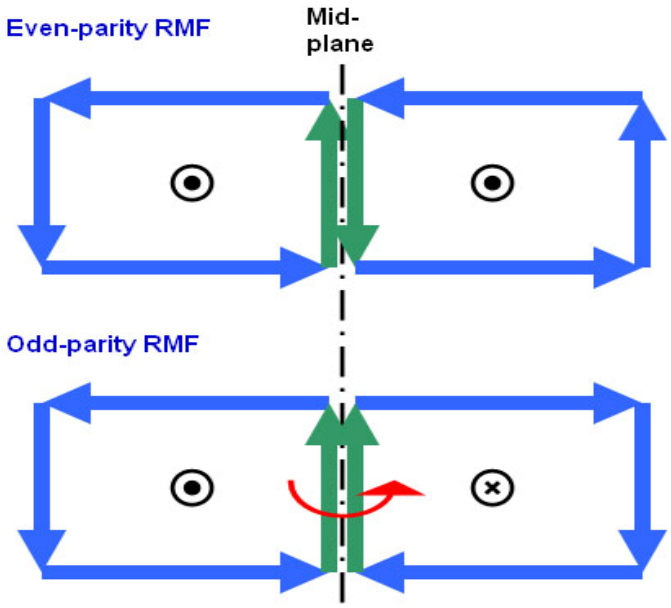

FIG. 1.4 A top view drawing of the current in an RMF antenna and the resultant magnetic field for even-parity and odd-parity operation.

1.3 The Translation, Confinement, and Sustainment Upgrade Experiment

The TCSU experiment was built to reduce the impurity levels which hampered the performance of the FRCs created in TCS. A new ultra-high vacuum (UHV) system was constructed for TCSU. The vacuum chamber assembly was done in a clean room following strict UHV protocol. The end result was a 3.5 m^3 vacuum chamber with a base pressure of approximately 1 x 10^{-8} Torr with constant wall heating at 120 °C. With the wall heating removed and the vacuum chamber at room temperature the pressure fell to roughly 1 x 10^{-9} Torr [11].

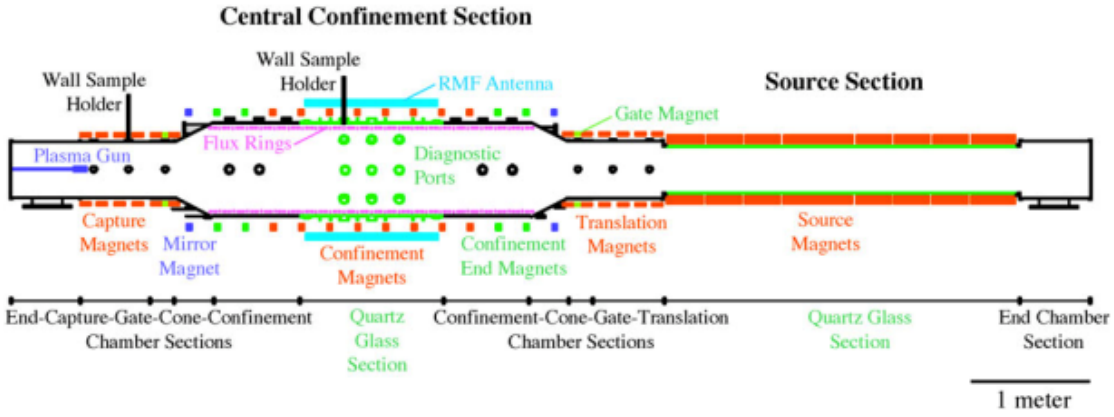

FIG. 1.5 Schematic of the TCSU experiment. The green areas represent quartz vacuum chambers.

The schematic shown in Fig. 1.5 is a scaled drawing of the TCSU experiment which consists of two main sections. The source section was built for FRC formation by the FRTP method but was never used because the plasma gun mounted on the end flange at the far left of the drawing was capable of supplying the necessary pre-ionized gas required for direct FRC formation with RMF. In the drawing the plasma gun is shown in

the fully extended position. The plasma gun is a magnetized cascade arc source and in this position the axial magnetic field from the capture magnets acts upon the arc to reduce hot spots on the electrode which minimizes the impurity level of the ionized gas streaming out of the gun. The plasma gun is in the fully extended position during FRC operation but is retracted to sit behind a closed gate valve during wall conditioning, such as Ti-gettering or He glow discharge cleaning.

The central confinement section consists of a quartz tube 125 cm long with an inner diameter of 80 cm. The RMF antennas encircle the quartz tube and the FRC is formed and sustained in this section. Attached to either end of the large quartz confinement section are stainless steel sections each 75 cm long and 80 cm diameter. All vacuum seals in TCSU are metal except vacuum seals made to the quartz. Stainless steel bellows with standard ConFlat flanges welded to one end are attached to the quartz with a silicone RTV. The silicone RTV responsible for the quartz to metal seals is differentially pumped so their leak rate falls below 10^{-8} Torr.liter/sec and into the acceptable UHV range.

A set of internal flux conserving rings were installed in the central confinement chamber. A total of 78 tantalum coated aluminum flux rings, each spaced 3 cm apart and enclosing an internal diameter of 76 cm spanned the entire length of the confinement chamber ensuring that the FRC was always within the flux rings. Without a flux conserver the FRC would expand radially and break apart in microseconds. Conventionally, flux conservation has been accomplished with external rings or close fitting axial magnetic field coils. In TCSU internal flux rings were used to further reduce the plasma impurity content by keeping the FRC off the vacuum chamber walls. As the plasma moves towards the wall a current is induced in the rings to resist the penetration of the magnetic field which pushes the FRC back towards the center axis. The rings were mechanically held together but electrically isolated with alumina spacers to eliminate the possibility of an axial current running from ring to ring. This chapter concludes with a

photograph of the internal flux conserving rings in Fig. 1.6 and a wide field shot of the TCSU experiment in Fig. 1.7.

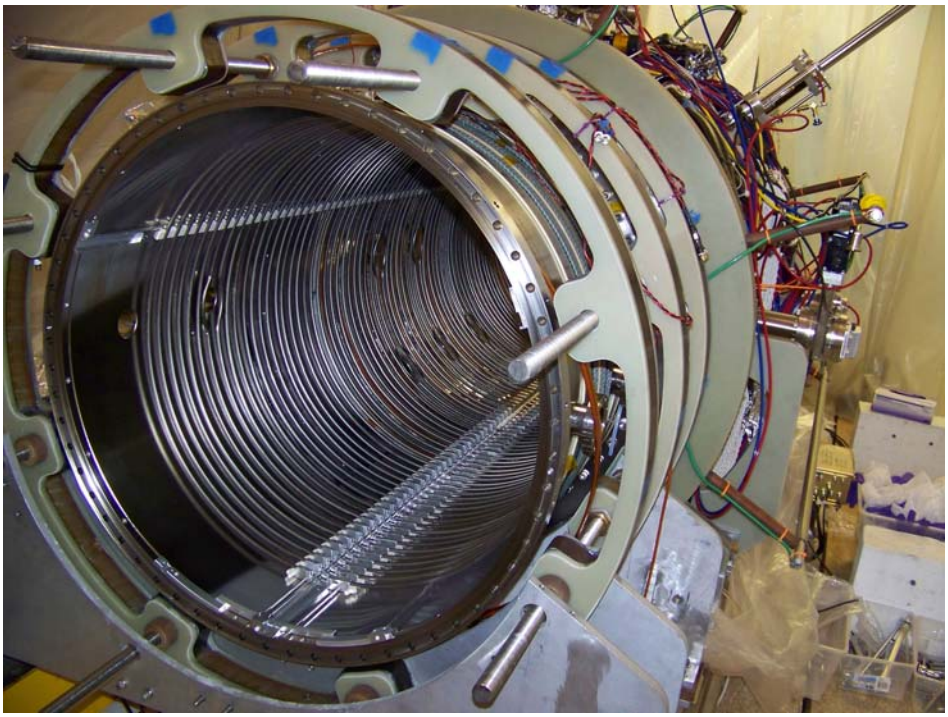

FIG. 1.6 Picture of the internal flux rings taken during a vacuum break.

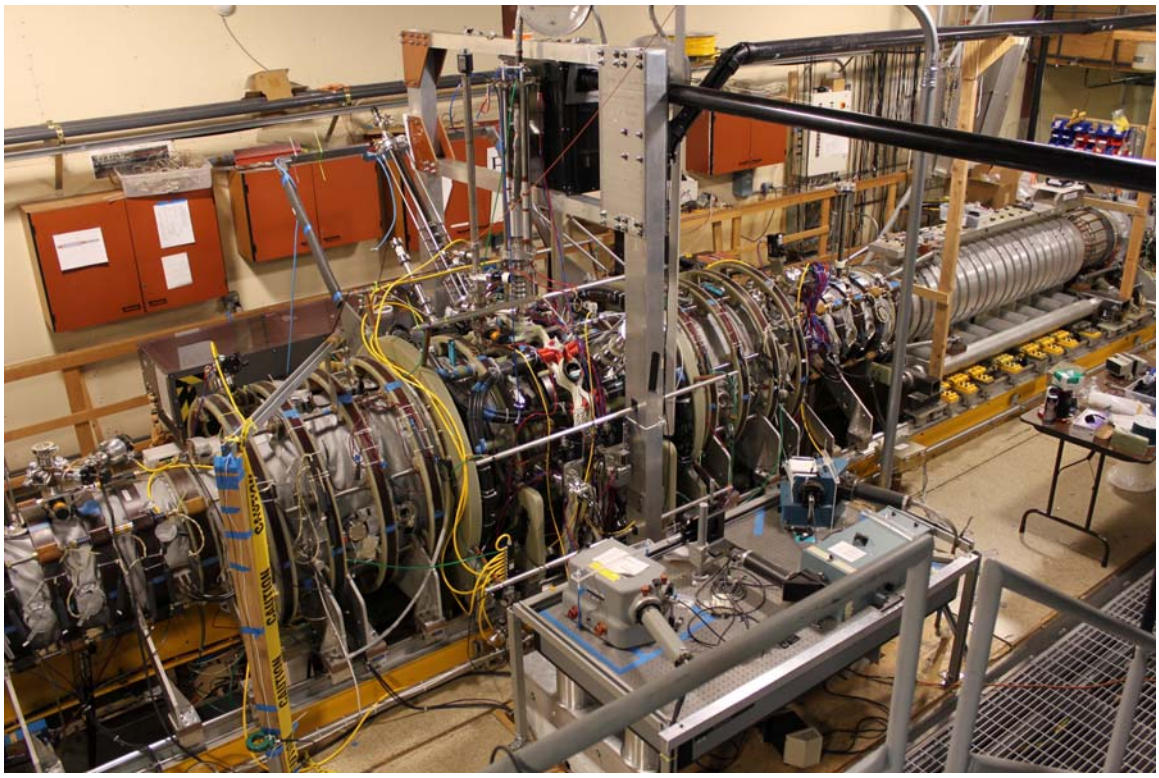

FIG. 1.7 Picture of the TCSU experiment. The central confinement section is in the center and the source section can be seen to the right.

Chapter II: Fast Response Ion Gauge (FIG)

2.1 FIG Design and Operation

A fast response ion gauge (FIG) was built to measure the neutral pressure in the confinement section. The FIG is comprised of the mechanical gauge in the vacuum chamber which is a Granville-Phillips model number 355001-YE, and the drive electronics and signal detection electronics which were designed and built by the author. The gauge used in TCSU is a Bayard-Alpert type otherwise known as an inverted triode gauge shown in Fig. 2.1. Like all ionization gauges, it operates by ionizing a fraction of the gas molecules present in the gauge and collecting the resulting ions. These positively charged gas ions produce an electrical current flow on the ion collector. The magnitude of this current is directly proportional to the density of gas molecules. A higher density of gas molecules will cause a larger ionization rate, resulting in a greater ion current on the collector. The voltage across a resistor in series with the collector is run through an isolation amplifier and then recorded by a digitizer.

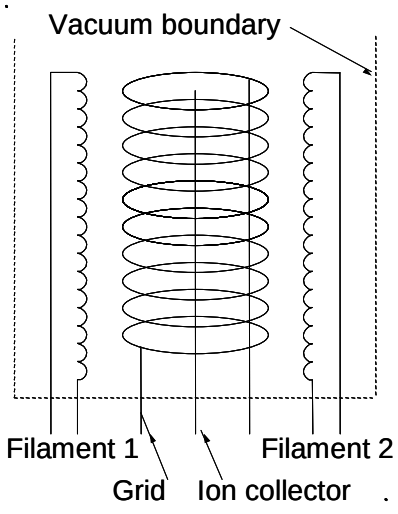

FIG 2.1 Schematic of an inverted triode gauge

The wiring diagram in Fig. 2.2 shows the power supply used to drive the filament and the DC-DC converters used to bias the filament and grid. A regulated DC power source is used to deliver the 2.7 amps necessary for thermionic emission of electrons from the filament. The regulated DC power supply is connected to an isolation transformer to prevent a ground loop. The filament is also biased to +30 volts with respect to the ion collector. A DC-DC converter is used to produce this bias voltage. The grid must be biased to +200 volts with respect to the ion collector. These bias voltages are necessary to impart enough energy to the electrons so they can ionize any neutrals present in the gauge tube. Separate 5.7 amp-hour 12-volt batteries power each DC-DC converter. Batteries were used to isolate each component and to reduce the noise on the collector.

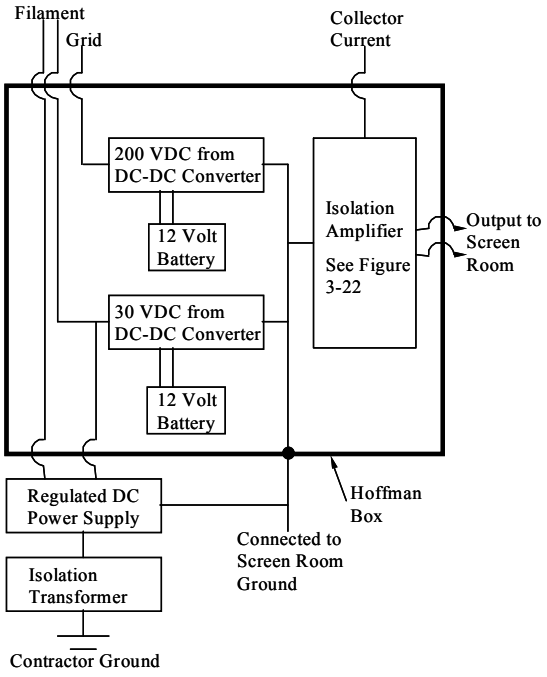

FIG. 2.2 Fast ion gauge wiring diagram.

The circuit used for the pressure measurements is shown in Fig. 2.3. This circuit features an optical isolation amplifier necessary to prevent a ground loop. The circuit has a net gain of approximately 16, a rise time of approximately 5 μsec, and offset control using the 5 kΩ potentiometer. An R1 value of 125 kΩ allows for accurate pressure measurements from 10^{-6} to $4x10^{-3}$ Torr. This range can be shifted towards lower pressures by increasing the value of R1.

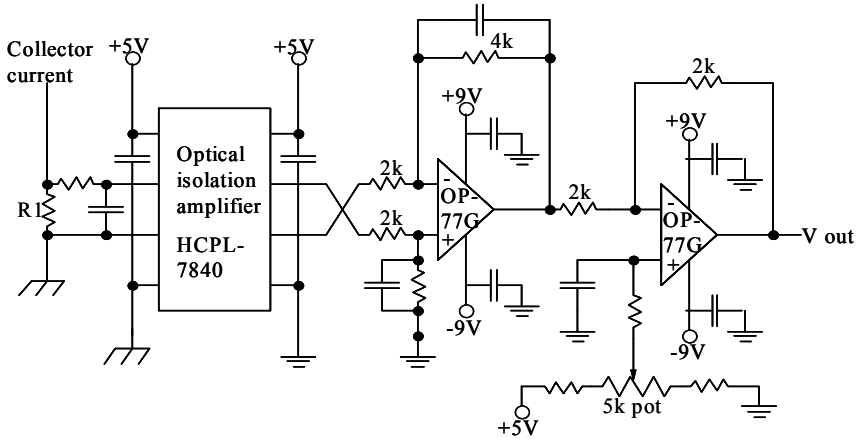

FIG. 2.3 Optical isolation circuit designed to measure the ion collection current.

The fast ion gauge (FIG) has been used on TCSU to measure the pressure in the confinement section during a typical pulse. Fig. 2.4 shows four different FIG traces. All traces show two pressure peaks; the first peak is from a 2.5 ms, 7.5 psia west mid-plane neutral gas puff and the second peak is from a 3 ms, 6 psia plasma gun puff mounted on the downstream end flange. These four FIG traces all have the same gas settings but they do not lie on top of each other because the vacuum conditions are different. The red trace (top trace) was taken with the gate valves to all vacuum pumps closed and the vacuum base pressure before the puffs at $1x10^{-5}$ Torr. The pressure is dropping because the vacuum chamber walls are clean and the puffed gas is being adsorbed by the chamber walls. The blue trace (bottom trace) was taken with the vacuum base pressure at $4x10^{-7}$ Torr and the gate valves for the 1100 l/s turbo pump and 3000 l/s cryopump open. The

middle traces, black and green, were both taken with the cryopump gate valve closed and at the same initial vacuum pressure but the turbo pump gate valve is open for the black trace and closed for the green trace. This indicates that the wall pumping is much better than the turbo pump when the wall is very clean.

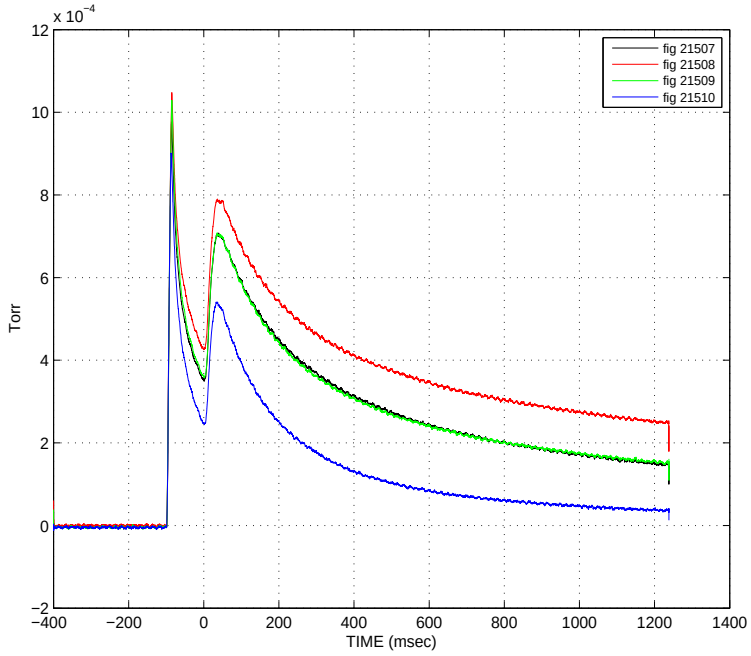

FIG. 2.4 Fast ion gauge measurement of the pressure in TCSU resulting from the same puff pressure and duration but different vacuum conditions indicating how well the chamber walls adsorb gas.

2.2 TCSU Puff Valve Analysis

The fast ion gauge has made possible the approximation of the flow rate of each puff valve in use on TCSU. Originally four puff valves were installed in the midplane of TCSU but it was found that no more than two were ever needed so the additional valves were removed and used as spares. All puff valves installed on TCSU were Series 9 Pulse Valves made by Parker. The vacuum interface orifice diameter of the valves is 0.031" and the poppet which seals the orifice is made of Vespel® a semi-rigid material capable of operation at temperatures up to 200 °C. The poppet is normally held closed with a spring and is opened by applying a current to an electromagnet in the valve body which acts on a ferrous armature on which the poppet is mounted. A cross-section schematic of the puff valve is shown in Fig. 2.5.

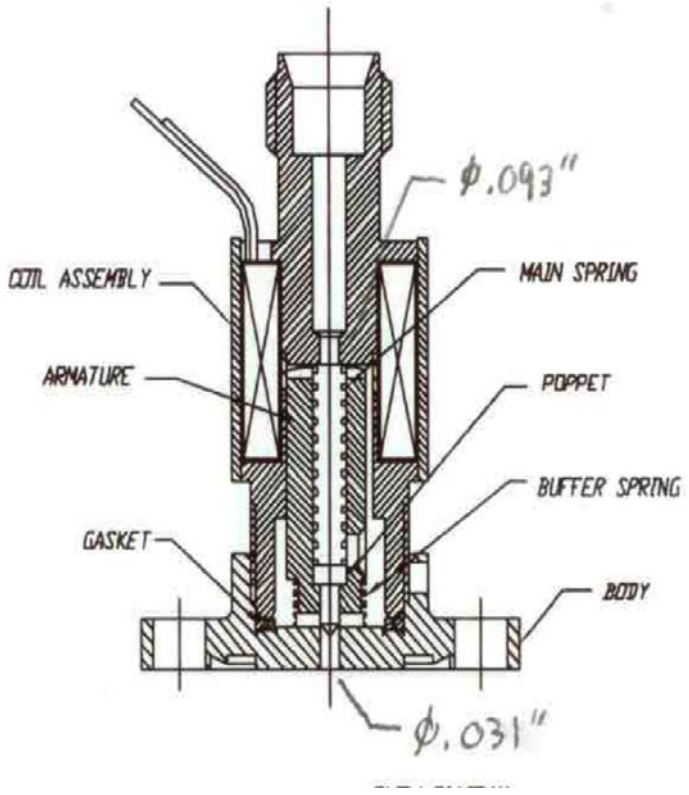

FIG. 2.5 Cross-section of a Parker Series 9 Pulse Valve in use on TCSU.

It has been known that the puff valves in use on TCSU take a long time to close relative to the gate applied. The approximate closing time of the puff valve was explored using the fast ion gauge. The plenum behind the puff valve was pressurized to 10 psia of deuterium gas and the puff gate was varied to highlight the time required for the puff valves to fully close. Typically the vacuum chamber walls pump neutral deuterium very well due to the rigorous schedule of He glow discharge cleaning which was usually switched on every night. The occasional Ti-gettering deposited on the chamber is also an excellent pump. If the He glow is not used for a few days and deuterium is regularly injected into the machine, as is the case during typical FRC formation, the walls saturate over time and are unable to pump. The gate valves protecting the turbo-pump and cryo-pumps are shut and gas is puffed in. In Fig. 2.6 a 10 psia puff is injected with different applied gates. It is clear to see that the chamber pressure is inordinately high for the short duration puffs compared with the longer duration puffs. Further experimentation has shown that the poppet requires approximately 8 ms to fully close after the gate applied to the puff valve terminates. The puff valve closure time is so long because the magnetic field acting on the armature saturates it so a residual magnetic field remains in the armature even after the electromagnet is shut off. It has been seen that this begins to happen after for an applied gate of 400 μs or more. The puff valve driver circuit was designed by the author and is covered in detail in Chapter 3. It supplies an initial pulse of 300 V to force the poppet open quickly and then delivers a steady 25 V to keep the poppet open indefinitely without damaging the puff valve.

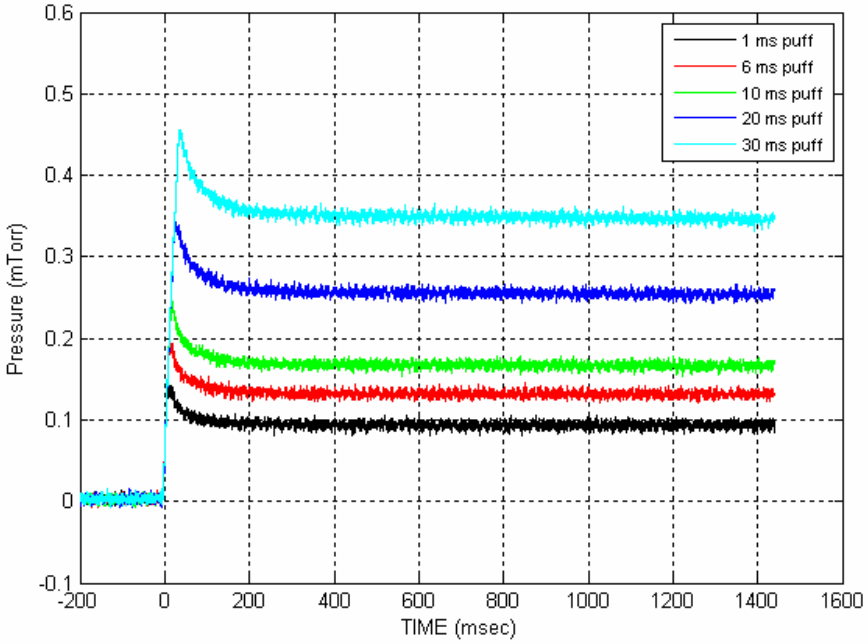

FIG. 2.6 FIG measurement of the TCSU chamber pressure for a 10 psia puff with a duration in the range from 1 ms to 30 ms.

When the puff valve gate duration is reduced below 400 μs the armature does not delay the main spring from closing the poppet. This is detailed in Fig. 2.7 where a 10 psia puff is injected but the gate duration is now varied from 1000 μs to 105 μs. It has been determined that the main spring will fully close the poppet in roughly 2.5 ms when the applied gate duration to the puff valve is below 400 μs. These traces are completely repeatable and in this way the puff valves can operate effectively for a shorter duration. Driving the puff valves in this way not only saves gas but also protects the vacuum chamber walls from adsorbing unnecessary deuterium so in essence the walls stay cleaner for longer and the benefits of wall conditioning like He glow discharge cleaning are preserved.

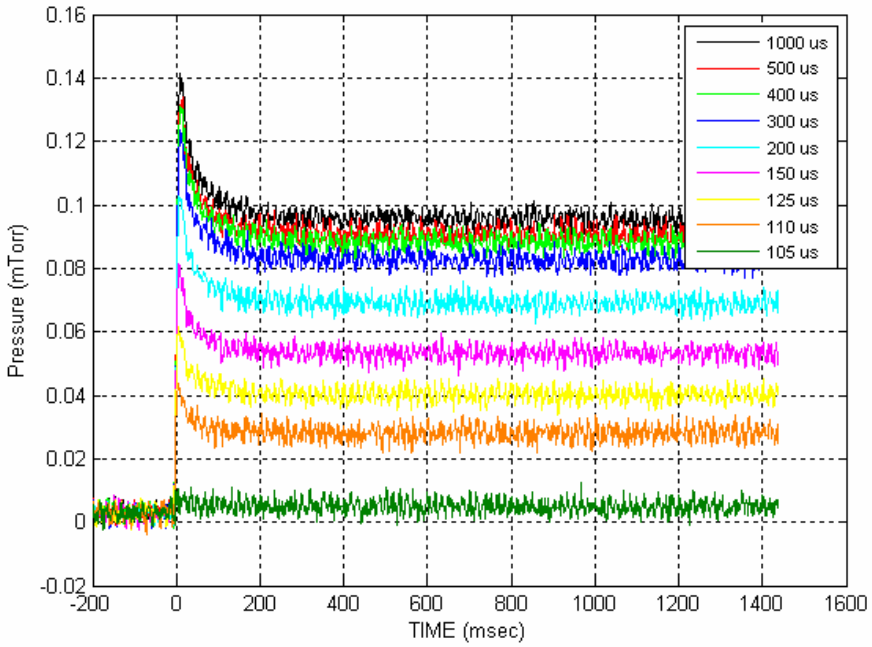

FIG. 2.7 FIG measurement of the TCSU chamber pressure for a 10 psia puff with a duration in the range from 105 µs to 1000 µs.

The fast ion gauge has been used to measure the vacuum chamber pressure for a range of applied gate timings and puff valve plenum pressures. This data has been used to characterize the puff valves on TCSU. By varying the plenum pressure for a set gate duration and doing this for multiple gate durations the vacuum chamber pressure can be determined for any plenum pressure and applied gate duration. Fig. 2.8 is the TCSU vacuum chamber pressure as measured by the FIG normalized to the puff valve plenum pressure. This graph can be used to determine what the resulting chamber pressure will be in mTorr for any puff valve plenum pressure (80 psia max tested) and gate duration.

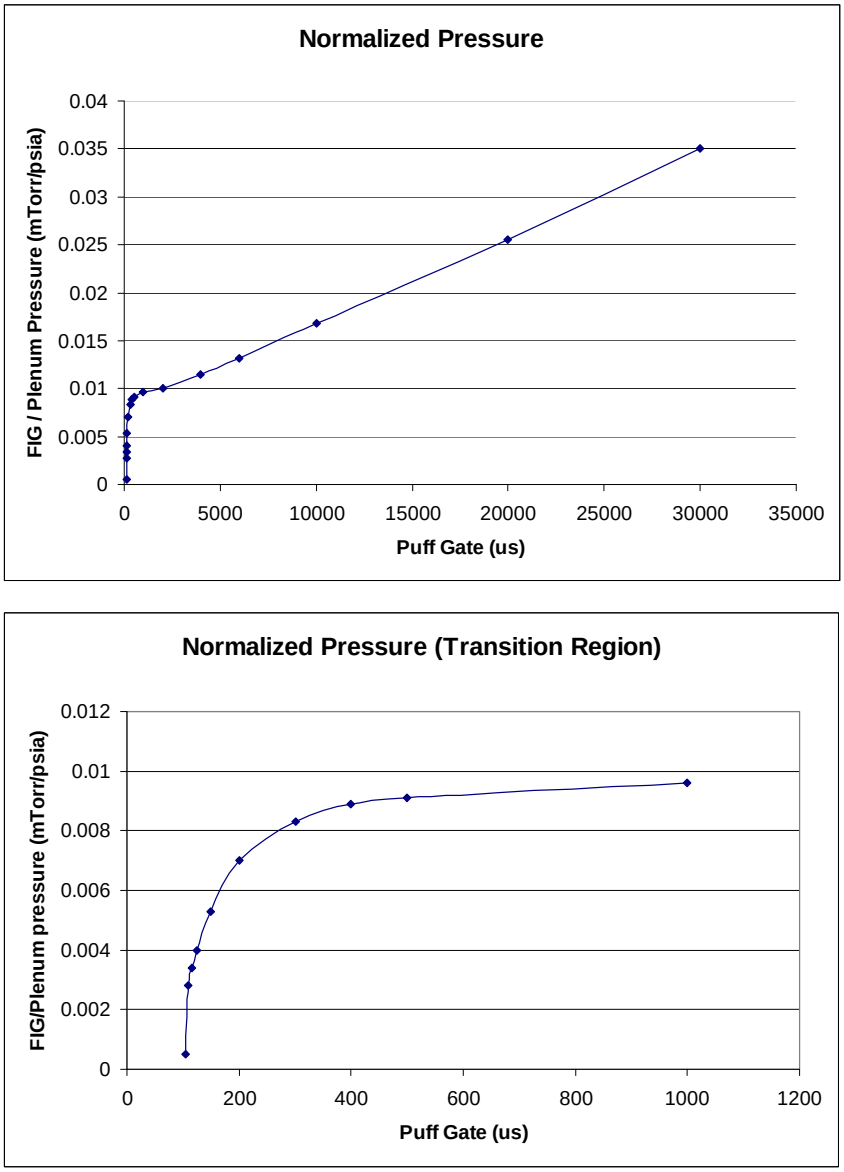

FIG 2.8 The resultant TCSU chamber pressure for a range puff valve gate durations and any plenum pressure. The bottom graph is a close up the transition region in the top graph from 0 µs to 1000 µs.

Chapter III: Magnetized Cascade Arc Source

3.1 Introduction

A translatable, ultra-high vacuum compatible, magnetized cascade arc source (MCAS) has been designed and constructed to inject a directional plasma beam used as source plasma for RMF driven FRCs in the TCSU experiment [12, 13]. The arc source, also known as a washer gun, can produce clean plasma by flowing deuterium across an arc discharge. The arc is formed between the two principal electrodes; the cathode, which is on the upstream side, and the anode. A stack of alternating insulating and conducting washers is used to confine and sustain the arc. The conducting washers are usually made of the same material as the electrodes and they provide a partially conducting boundary that stabilizes the discharge plasma. The insulating washers are made of boron nitride and have a much larger inner diameter than the conducting washers. They are used to electrically isolate the conducting washers so they cannot short the anode to the cathode. With the washer stack in place the arc source is very reproducible. A 3 millisecond arc discharge is shown in Fig. 3.1.

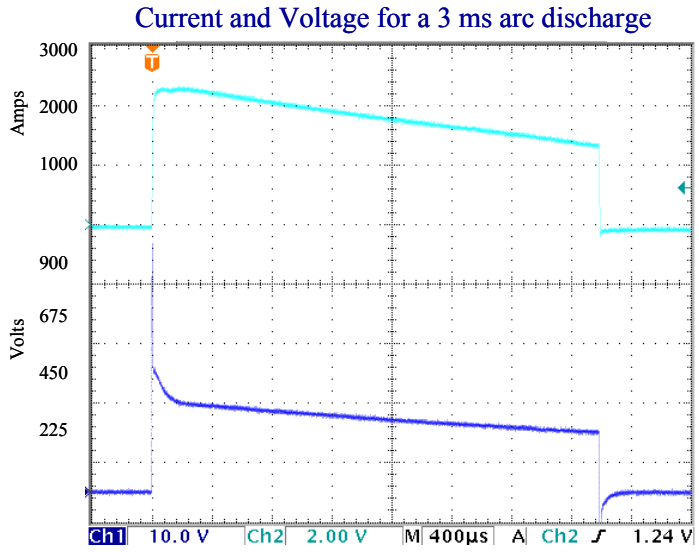

FIG 3.1 Current and voltage for a 3 ms arc discharge.

The plasma gun to be used on TCSU was designed to be used in a clean, ultra-high vacuum environment. The plasma gun was also designed to be translatable and as robust as possible. Fig. 3.2 shows a cross-sectional view of the plasma gun. The cathode and washer stack fit inside a Macor, or machinable glass ceramic, sheath and the anode is held in place by a boron nitride ferrule. All of the components are contained within a stainless steel pipe and are compressed using a retaining ring. This robust design not only makes it easy to change the dimensions of the plasma discharge chamber but the anode and cathode are easily replaced also. The electrode material is chosen to have the lowest possible electrical erosion rate but must still be machinable. All arc discharges to date with this plasma gun have been made using molybdenum but carbon electrodes and washers were also made but were never tested before the TCSU experiment was shut down. More exotic materials such as silver tungsten alloys can also be used.

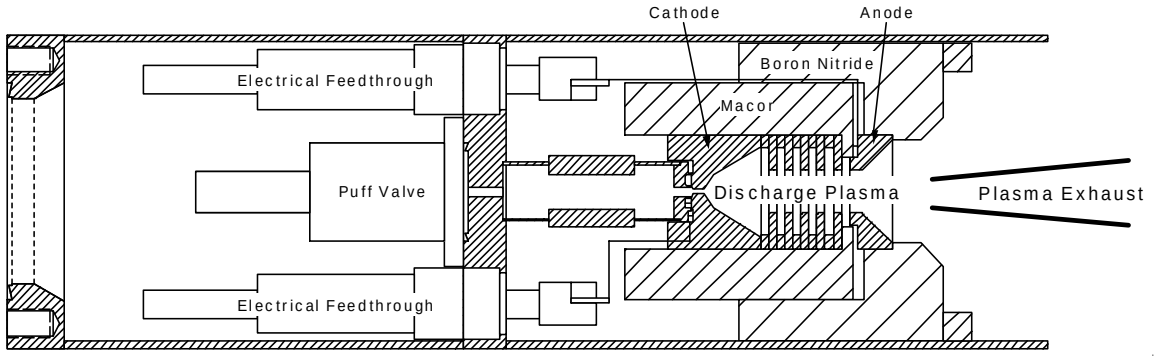

FIG 3.2 Schematic of the plasma gun in use on TCSU.

A 3 kilojoule, IGBT (integrated gate bi-polar transistor) controlled power supply has also been built and is used for initial breakdown and arc sustainment. The use of IGBTs makes it possible to vary the plasma discharge time from as little as 100 microseconds to nearly 10 milliseconds. A 900 volt potential is applied across the anode

and cathode for initial breakdown. This initial voltage is supplied by high voltage 4 microfarad capacitors. After the initial breakdown is achieved the 30 millifarad capacitors supply the charge necessary for arc sustainment. The IGBTs are protected by a 24 microfarad snubber circuit. Two Pearson probes are mounted inside the power supply enclosure to measure the plasma discharge voltage and current. A wiring diagram of the power supply is shown in Fig. 3.3.

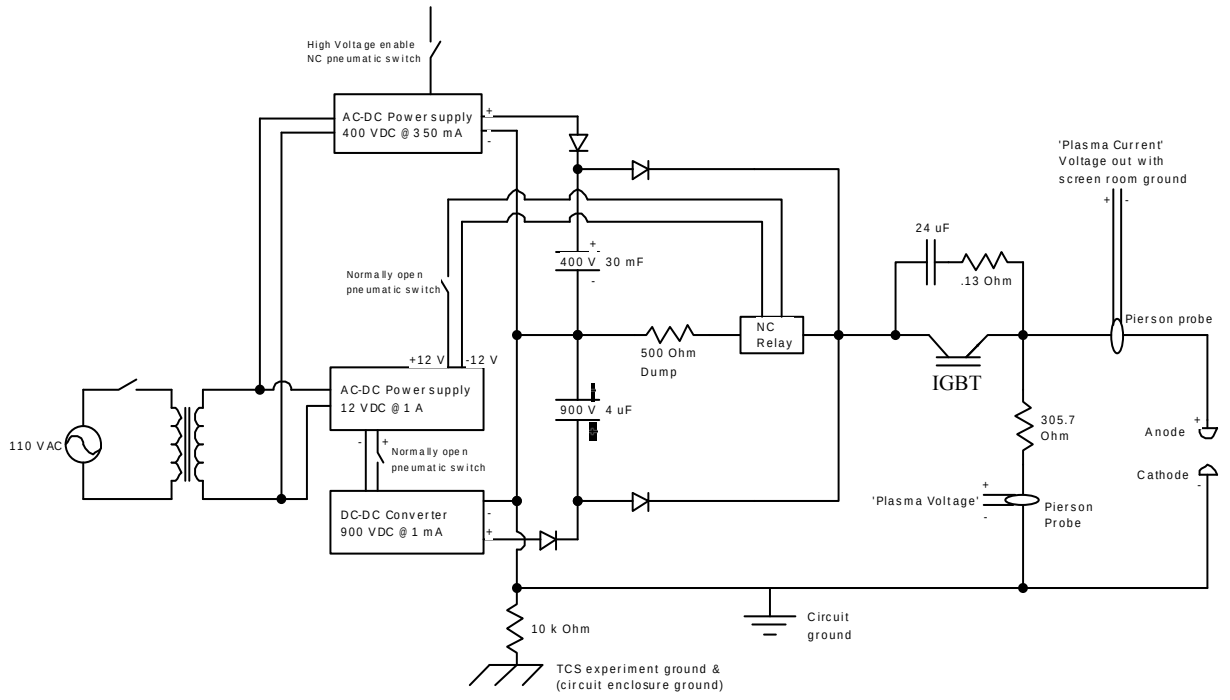

FIG 3.3 Wiring diagram of the power supply used with the plasma gun.

Before TCSU operation began the plasma gun was test fired on a 90 liter vacuum chamber to determine its reliability and discharge plasma parameters. The test chamber was equipped with a double Langmuir probe and fast response ionization gauge. A base vacuum pressure of 8.8×10^{-8} Torr was achieved ensuring a quality operating regime. Pictures of the arc discharge were taken with an Imacon camera to elucidate arc

formation and uniformity. A schematic of the test vacuum chamber showing the relative positions of the plasma gun, Langmuir probe, and fast ion gauge is shown in Fig. 3.4.

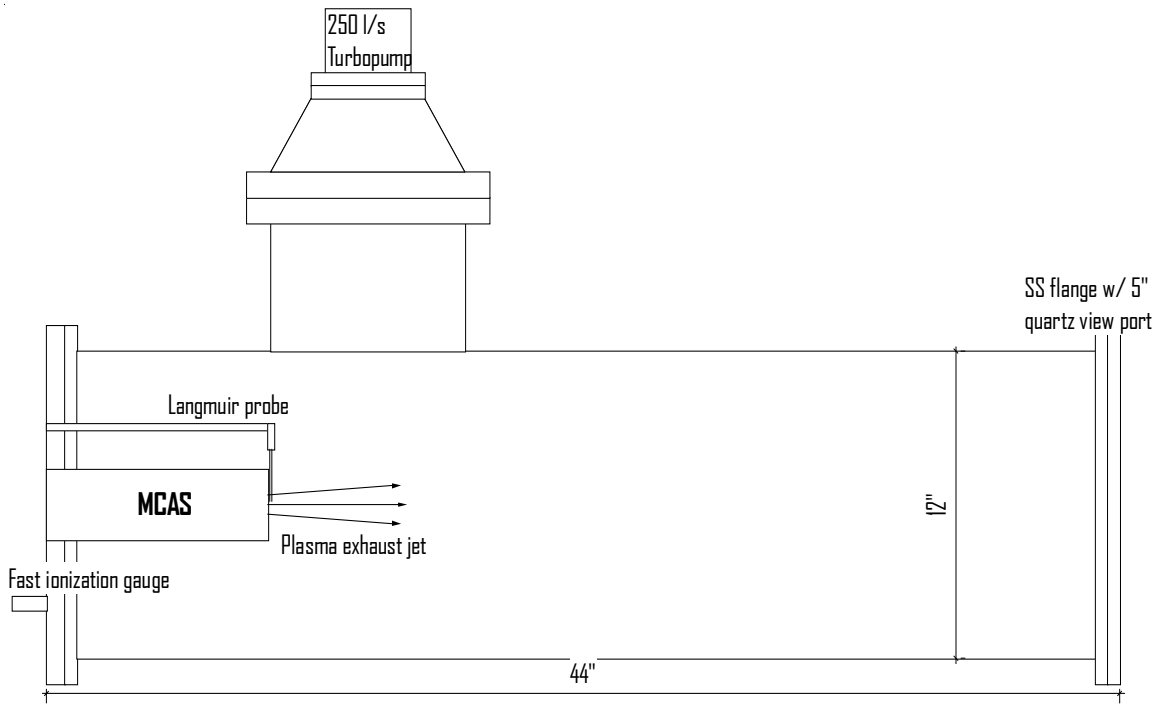

FIG. 3.4 Schematic of vacuum chamber used for MCAS testing.

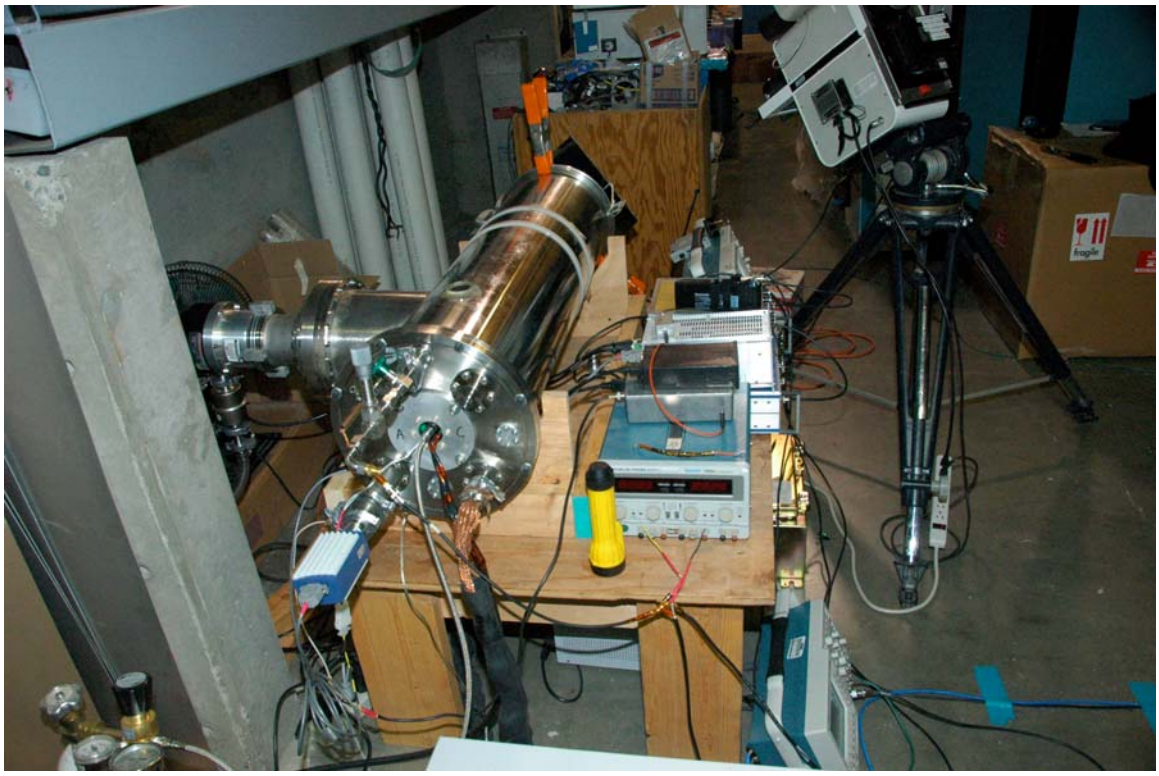

FIG. 3.5 Picture of the MCAS test chamber setup.

Once the test chamber was completed with the MCAS installed the arc discharge was found to be completely repeatable with zero extraneous arcing. Fig. 3.6 shows a collection of current and voltage traces taken of the MCAS at various arc discharge durations. The current and voltage decay times are always uniform. A picture of the plasma gun with the Langmuir probe rotated out of the way and a picture showing the gun firing are shown in Fig. 3.7.

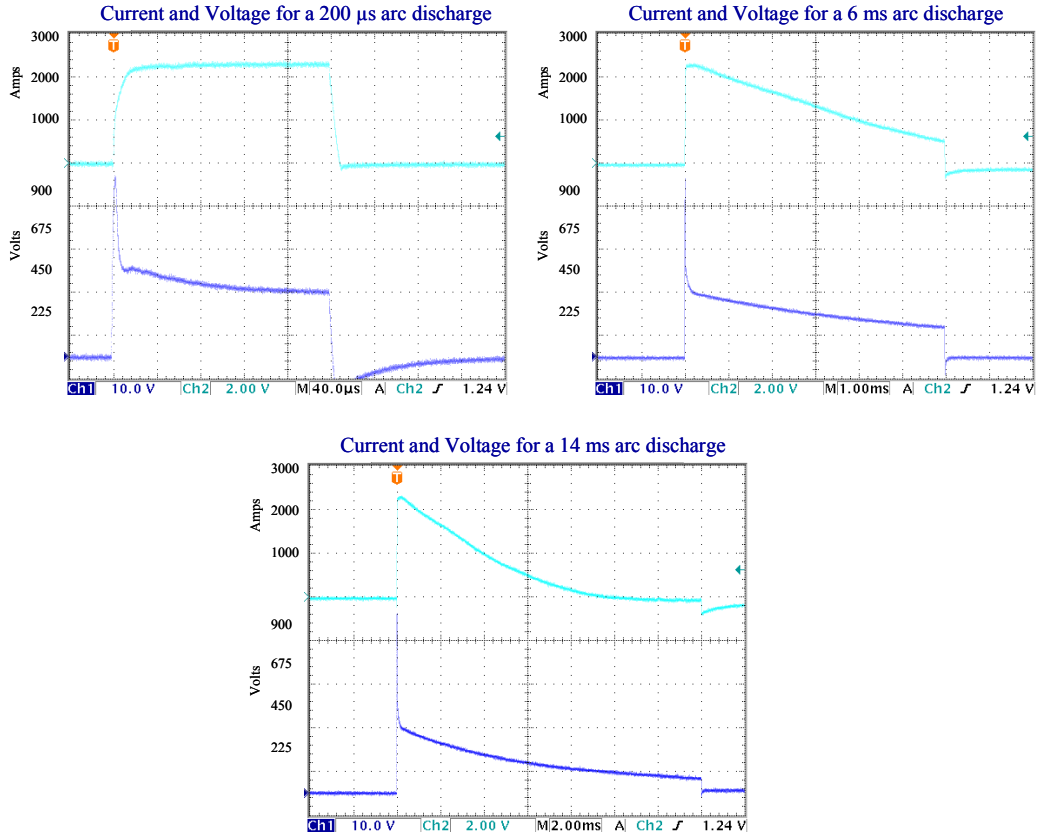

FIG. 3.6 Current and voltage for 200 µs, 6 ms, and 14 ms MCAS arc discharges.

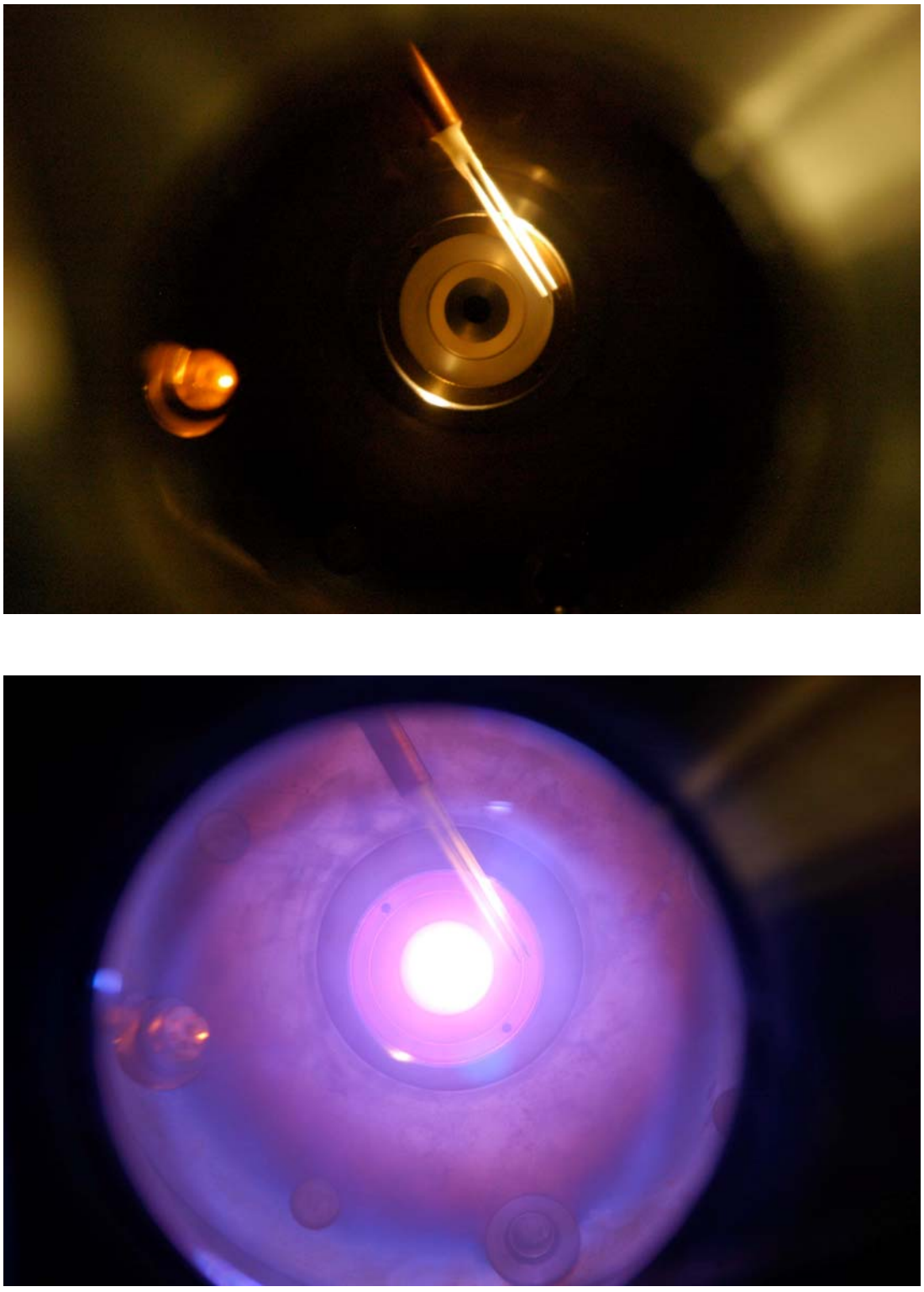

FIG. 3.7 Axial pictures of the plasma gun at rest (top) and during operation.

A double Langmuir probe, described in detail in Chapter 4, was used to measure the electron temperature and density of the MCAS arc discharge plasma. The probe was positioned in the plasma exhaust approximately 4 cm from the anode. Fig. 3.8 shows the resulting I-V trace taken 0.5 ms after arc formation for a 3 ms discharge with the same voltage settings as the discharge shown in Fig. 3.1. The electron temperature of the MCAS arc discharge has been measured at 10 eV. The electron density is measured to be 3.3×10^{19} m^{-3}.

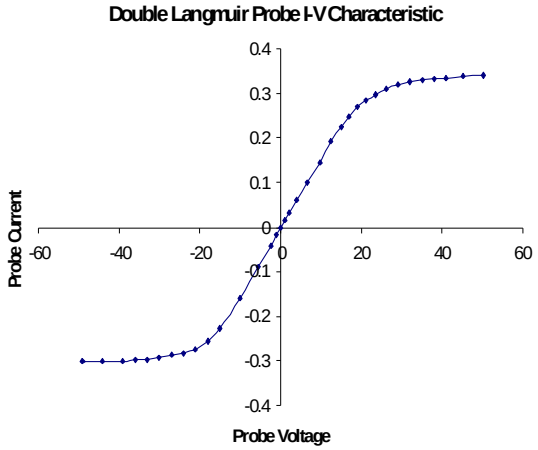

FIG. 3.8 I-V characteristic as measured with a double Langmuir probe of a typical MCAS discharge.

3.2 Puff Valve Driver Circuit

The MCAS has been successfully fired on TCSU over 10000 times. It is the sole source of pre-ionization used and has never been responsible for any delay in the operation of TCSU. Before the MCAS was fired a driver for the puff valve, identical to the puff valves on the rest of TCSU detailed in Chapter 2, needed to be designed. The puff valve driver designed to be used with the MCAS was so successful that it was duplicated and used to control all the puff valves on the TCSU experiment.

The puff valves can be opened much quicker than the manufacturer specifies by driving the magnet coil in the valve with a higher voltage than is recommended, although the coil can not be operated at high voltage for long or it will burn out. It is also important to have the ability to operate the puff valve for any duration desired so, in addition to the initial burst of high voltage to force the valve poppet open quickly, a continuous drive voltage within the recommended specifications is also required. Finally, it also needed to be controlled with a fiber optic gate sent from the TCSU screen command room.

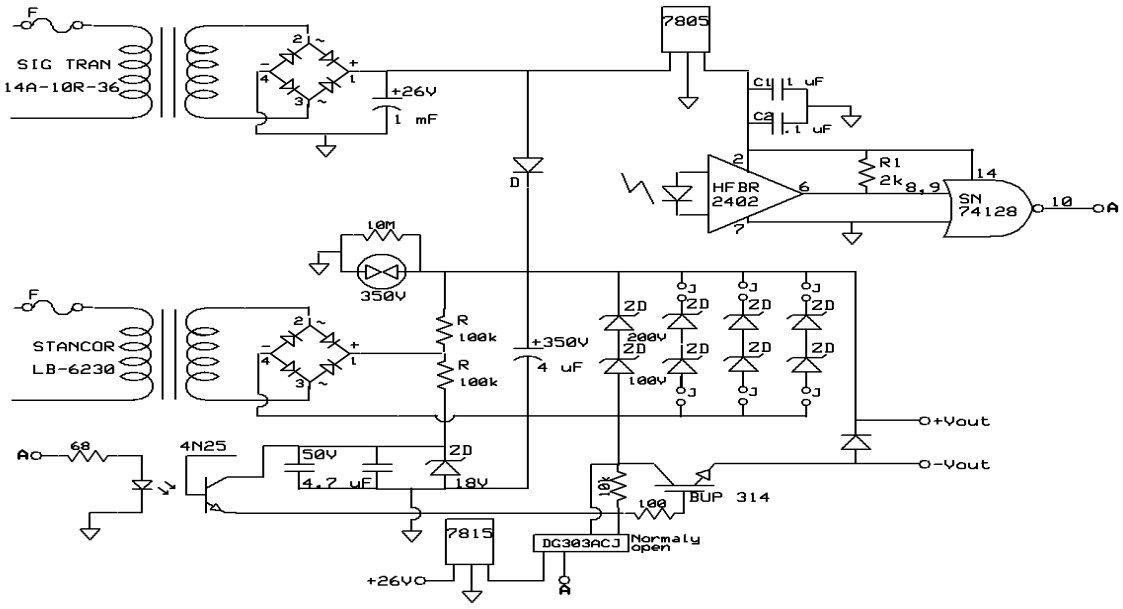

FIG. 3.9 Schematic of the puff valve driver designed and built for TCSU.

A schematic of the puff valve driver originally designed for the MCAS and incorporated into control of all puff valves on TCSU is shown in Fig. 3.9. A fiber optic gate is sent from the screen room which activates an IGBT puff valve driver. An IGBT is used to close the circuit for the entire duration of the fiber optic gate. A 350 V, 4 μF capacitor supplies the initial high voltage. This is built on top of a 1 mF capacitor charged to 25 V that supplies the steady voltage necessary for long duration operation. Each capacitor is charged with rectified AC so it only needs to plug into a standard 110 V outlet. A bank of zener diodes were also added to the circuit so the maximum voltage output could be reduced if the full capacitor voltage was found to be damaging the puff valve. The puff valves on TCSU showed no ill effects from operation at the maximum voltage so the output was always set to maximum.

A circuit board for the puff driver was designed with ExpressPCB software and they manufactured the board according to the design specifications. Eight circuit boards were ordered and were wired up at RPPL. The circuit board was designed to fit into a small metal enclosure carried by any electronics specialty store. A picture of the final circuit ready for use is shown in Fig. 3.10.

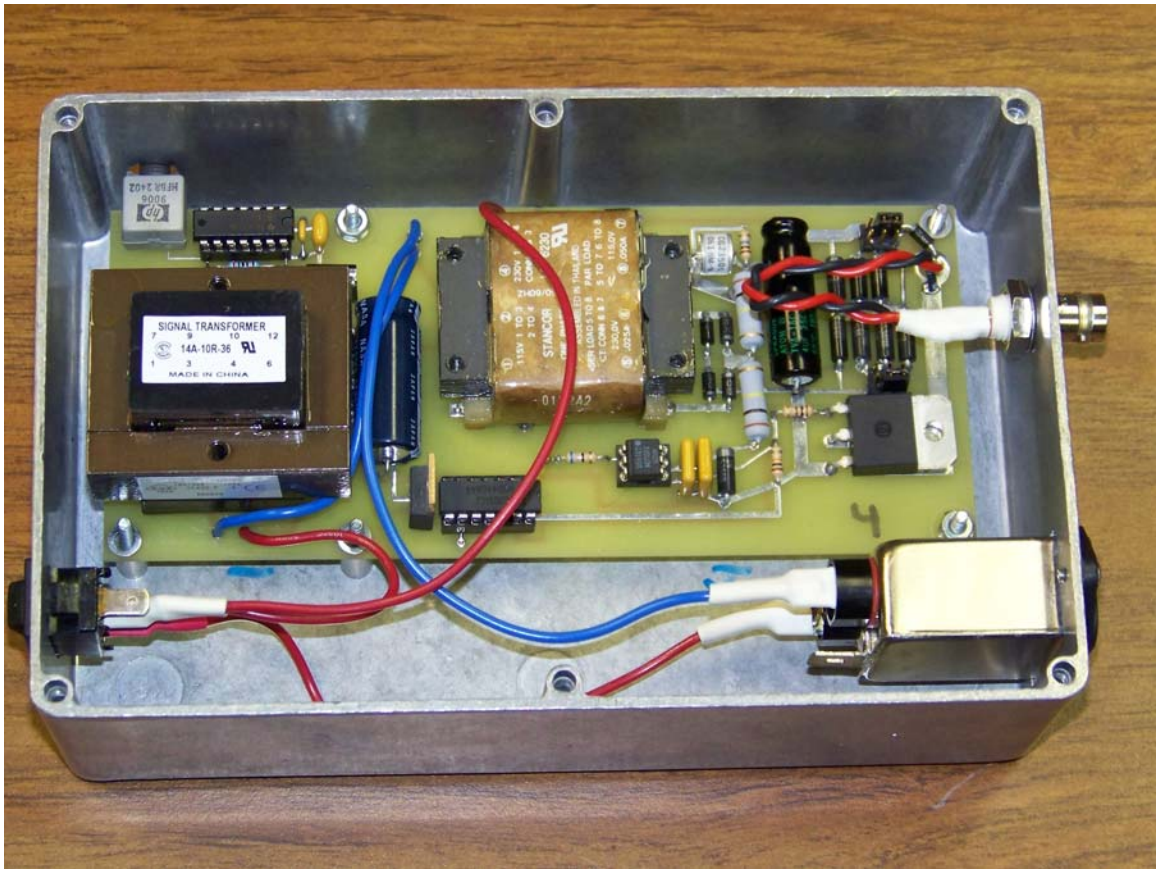

FIG. 3.10 Picture of the puff valve driver used on TCSU.

Chapter IV: Combination Probe Design and Theory

4.1 Combination Probe Design

A combination Langmuir/Mach probe has been developed to measure electron temperature and density as well as ion flow speed in TCSU. The probe is fully translatable allowing it to diagnose all radial locations of the FRC at either the mid-plane, end section, or in the exhaust jets. The 1/4" probe stalk consists of interlocking boron nitride cylinders which encompass a 1/8" diameter stainless steel tube that houses the probe wires. In addition to the stainless steel jacket the probe wires are twisted to minimize electromagnetic noise pickup. The tip of this combo probe is composed of a boron nitride housing and eight .020" diameter tungsten collection leads. In TCSU, the RMF used to form and sustain the FRC makes Langmuir probe measurements difficult. To this end we have developed a drive circuit that will generate the bias voltages necessary for Langmuir probe operation. This bipolar power supply can produce steady voltages up to 200 volts at loads over 1 amp and can be swept at any frequency up to 1.5 MHz. The probe current and bias voltage are measured with Pearson probes.

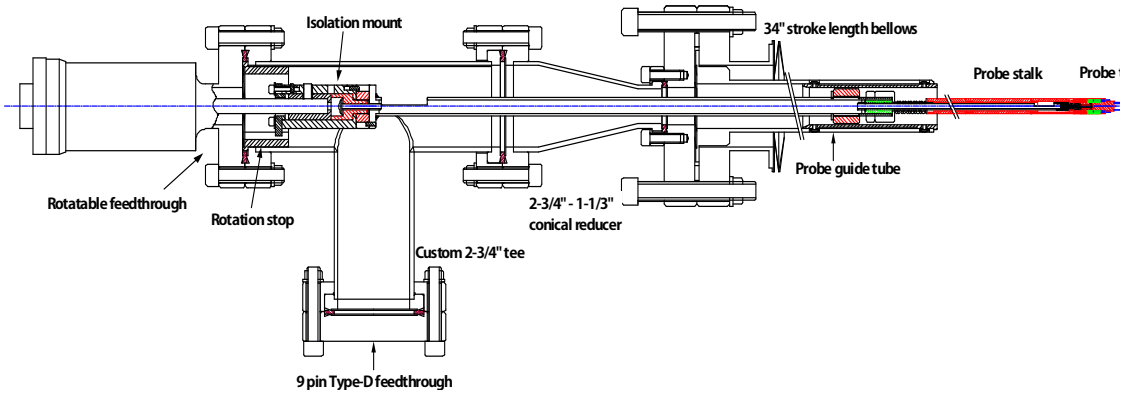

FIG 4.1 Schematic of the combination Langmuir/Mach probe in use on TCSU.

A scale drawing of the combination Langmuir/Mach probe is shown in Fig. 4.1. The full length of the probe is not clear because of the length breaks so a picture of the completed probe without the bellows attached is shown in Fig. 4.2. The length of the probe from the electrical isolation mount on the rotateable feedthrough to the probe tip is approximately 49.5". The boron nitride stalk is 21.5".

FIG 4.2 Picture of the combination probe, sans bellows.

Like the rest of the probe stalk, the boron nitride tip is cylindrical except for the very top which is cut into a square necessary for Mach probe operation. Four of the tungsten collection leads are located on the sides of the square and make up the Mach probe part of the combo probe. The other four tungsten collectors stick out of the top of the square tip. One of these top collectors is used to reference the Mach probe while the other three collectors comprise the Langmuir part of the probe and can be used in a single, double, or triple configuration. In Fig. 4.3 a close-up drawing of the probe stalk and tip is shown. The probe stalk is .250" in diameter and the Langmuir tips are .125"

long and are spaced .090” apart. The Mach tips are .110” long and are .170” apart because of the isolation needed for Mach probe operation.

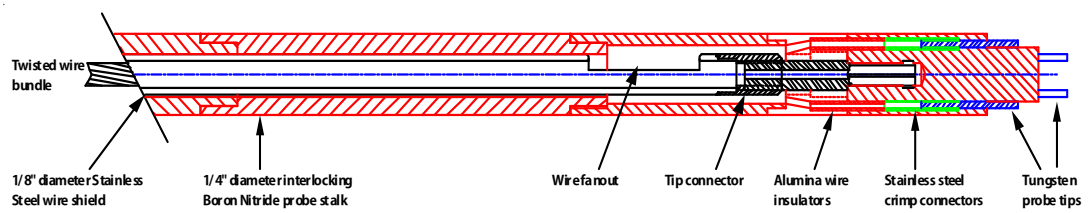

FIG 4.3 Probe stalk and tip.

To achieve the correct tip spacing for Langmuir and Mach probe operation every bit of the 0.25” diameter boron nitride tip housing must be utilized. This made it impossible to overlap the tip housing with the wire guide, as is done in the rest of the probe stalk, so the alumina insulators are used to eliminate the possibility of plasma contact with the probe wires. Fig. 4.4 shows the probe wires with the alumina wire insulators and the tungsten to copper wire crimps in place. 30 AWG solid core copper wire with kapton insulation is used. Thin walled stainless steel tubing was used to crimp the probe wires to the tips. Fig. 4.5 shows the completed probe tip and stalk. Three of the four tips emanating from the square part of the boron nitride housing are used in a Langmuir configuration while the fourth tip can be used to reference the Mach probe tips seen next to the square part of the housing.

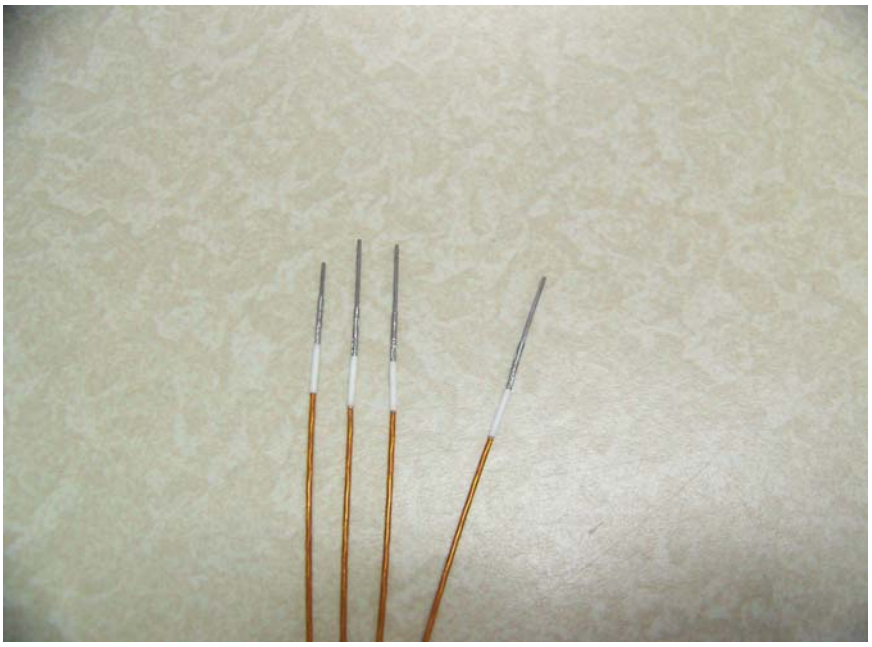

FIG 4.4 Probe wires crimped to tungsten probe tips.

FIG 4.5 Picture of the completed probe tip.

On TCSU the combination Langmuir/Mach probe was used to measure the temperature profile and ion flow velocity at the mid-plane and in the FRC exhaust jets. The turbulent nature of the RMF used to form and sustain the FRC makes Langmuir probe measurements difficult. To this end we developed a drive circuit that can generate the bias voltages necessary for Langmuir/Mach probe operation. As stated before, the bipolar power supply is capable of steady voltages of nearly 200 volts at any frequency up to 1.5 MHz across a load that can draw up to 1 amp of current. A block diagram of the probe electronics is shown in Fig. 4.6. The wiring schematic of the combination probe bias voltage generator is shown in Fig. 4.7.

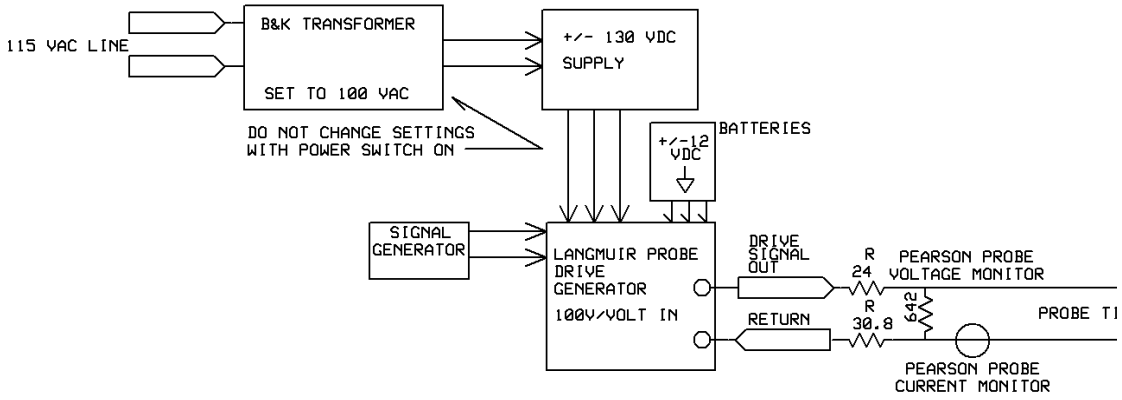

FIG 4.6 Block diagram of the combination probe electronics.

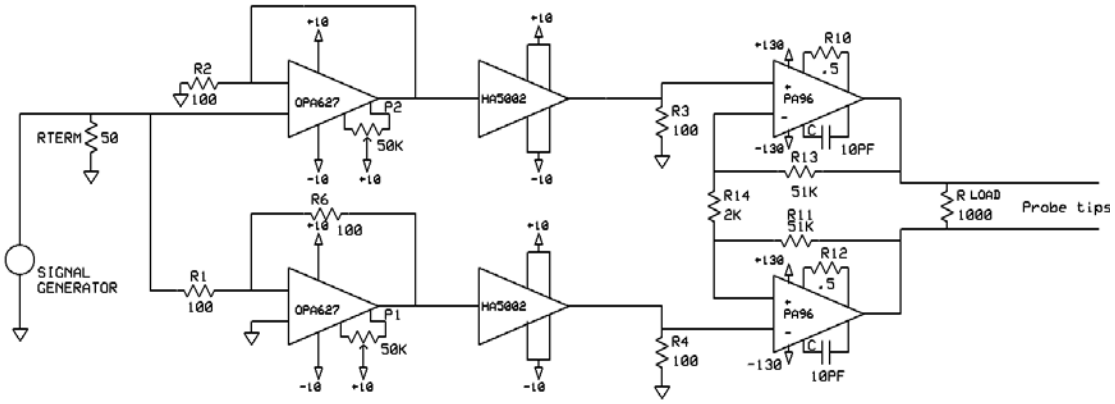

FIG 4.7 Wiring schematic of the bias voltage generator.

The bipolar 130 VDC power supply powers the PA96 MOSFET amplifiers which act in a push-pull configuration. Fig. 4.8 shows the sweep voltage from the generator and the resulting current when connected to a 300 Ω load with a 500 kHz input sine wave.

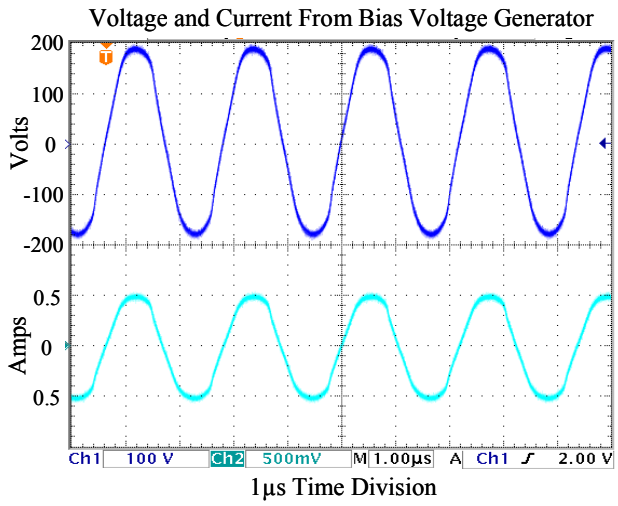

FIG 4.8 Voltage and current from the voltage generator during a bench test.

4.2 Double Langmuir Probe Theory

The double probe method makes use of two single probe tips biased with respect to each other but insulated from ground. In this configuration the entire system floats with the plasma so it follows the change in plasma potential. Originally proposed by Johnson and Malter [14] this method was developed for use in decaying plasmas. It was found to be quite accurate in measuring the electron temperature in turbulent and driven plasmas as well. If the plasma potential is changing with time it is difficult to maintain a constant potential difference between an electric probe tip and a given reference point like a vacuum chamber wall or internal flux ring, making the double probe the best option.

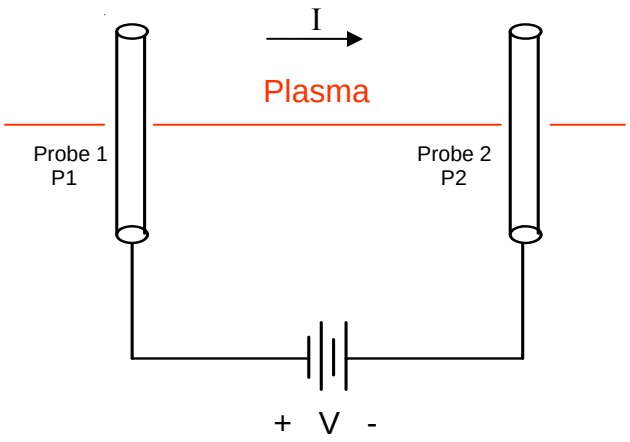

FIG. 4.9 Schematic of a floating double Langmuir probe showing the convention used for positive current and voltage.

The spacing of the double probe tips is such that they are far enough apart so it is unlikely to start an arc between them but close enough together so the plasma properties in the region between the tips can be considered uniform. Consider a double probe with probe tips *P1* and *P2* each with an area of *A1* and *A2* located in a plasma with constant properties between them as shown in Fig. 4.9. This is a closed system that floats with the plasma. A voltage V is applied between the probe tips and assume the voltage to probe 1 V_1 is positive with respect to V_2 such that $V = V_1 - V_2 > 0$. With this convention the current I that flows between 2 and 1 is positive if the voltage is positive.

In the presence of plasma each probe tip will become negatively charged because of the faster influx of electrons than ions. The electrons are much faster than the ions; therefore they are more mobile and they act to shield the rest of the plasma from the disturbance the probe presents. As long as the area of each probe is similar they will each have a negative charge. The only way around this is if one probe is much larger than the other so it can collect more ion current than the saturation electron current to the smaller probe.

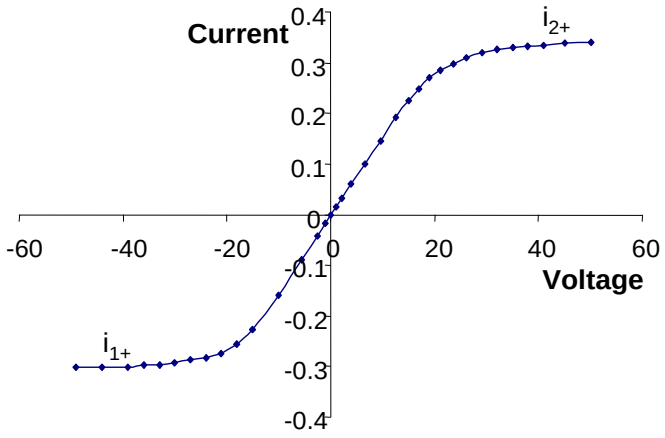

FIG. 4.10 A double Langmuir probe IV characteristic showing the typical linear slope through the origin and probe 1 and 2 ion saturation currents.

The double probe IV characteristic curve is shown in Fig. 4.10. When the applied voltage is zero both probes are at the floating potential so there is no net current going to either one. In our convention, if a positive voltage is applied then V_1 will become less negative than V_2 so more electrons will flow to probe 1 and fewer to probe 2 resulting in a positive current I. As the voltage is raised further probe 2 will draw ion saturation current i_{2+} while probe 1 will draw an electron current equal to the ion current to probe 2. A double probe can never draw a current greater than the ion saturation current because any electron current to one probe tip must be balanced by an equal ion current to the other probe tip.

The fact that the total current can never exceed the ion saturation current in a double probe presents a few notable advantages. Most importantly is the minimal effect this relatively small current draw has on the bulk plasma. In addition to the small plasma disturbance, the lifetime of the probe tips are increased since the maximum current is low; thus the material ablation is almost negligible. This also reduces the overall impurity content of the plasma which can limit the plasma temperature and performance.

The floating double probe quickly becomes negatively charged due to the initial bombardment of electrons which act to shield the bulk plasma from the presence of the probe. This negative potential will then repel most of the electrons so that only the most energetic will impact the probe. Hence, if we assume a given electron distribution in the bulk plasma it will remain so in the presence of the probe. Although sampling only the fast electrons in the tail of the distribution is a drawback the widely accepted accuracy of double probe measurements should be noted [15].

The behavior of plasma at a fundamental level is described by the collisionless Boltzmann equation, also known as the Vlasov equation. The time independent solution of the Vlasov equation is the Maxwell-Boltzmann velocity distribution function, also known as a Maxwellian distribution. This solution, which describes a distribution for a

system of particles in equilibrium, is an excellent approximation for the distribution of ions and electrons in a plasma. Of particular importance to Langmuir probes is the response of the plasma to the presence of an electrostatic field. In this case, the solution to the Vlasov equation is the Maxwellian distribution modified by the Boltzmann factor $e^{-\eta}$. The small area near a Langmuir probe where the effect of the probe is felt by the plasma in the form of an electrostatic field is called the sheath and the electron and ion distribution functions are modified in this region by the Boltzmann factor. If the electron density in the plasma is n_e then the electron density in the Langmuir probe sheath n_{es} can be calculated from Eq. (4.1).

$$n_{es} = n_e e^{-\eta} = n_e e^{(eV/kT_e)} \tag{4.1}$$

The effect of the electrostatic field in the Langmuir probe sheath modifies the Maxwellian distribution of electrons so the electron current density J_- to the probe is the random current density J reduced by the Boltzmann factor $e^{-\eta}$. The electron current to the probe is the product of the random current density, the probe area A, and the Boltzmann factor.

$$i_- = AJe^{(eV/kT_e)} \tag{4.2}$$

A relationship between total probe current I, voltage V, and electron temperature T_e can be found from a current loop analysis [16]. Define i_{1+} and i_{2+} to be ion currents to probes 1 and 2; and let i_{1-} and i_{2-} be the electron currents to probe 1 and probe 2. Consider the system to be floating, $V = 0$, so the following can be written:

$$i_{1+} + (-i_{1-}) + i_{2+} + (-i_{2-}) = 0 \tag{4.3}$$

It is easy to see from Eq. (4.3) that the ion current to the probes is balanced by the electron current so the total current in the loop can never exceed the maximum ion current attainable which is the ion saturation current i_{+}.

We have defined the total loop current I as positive when it flows from probe 2 to probe 1. Using this convention we obtain the relationship between the total current and the ion and electron probe currents.

$$I = i_{2+} - i_{2-} = i_{1-} - i_{1+} \tag{4.4}$$

The electron current to probe 1 can be found from Eq.(4.2) and can be inserted into the second of Eq.(4.4).

$$I + i_{1+} = A_1 J e^{(eV_1/kT_e)} \tag{4.5}$$

The voltage at probe 1 is $V_1 = V + V_2$ and is inserted into Eq.(4.5)

$$I + i_{1+} = A_1 J e^{(eV/kT_e)} e^{(eV_2/kT_e)} \tag{4.6}$$

The electron current to probe 2 is found using Eq. (4.2) and can be substituted in for the last term in Eq. (4.6) so that V_2 is removed as follows:

$$I + i_{1+} = \frac{A_1}{A_2} i_{2-} e^{(eV/kT_e)} \tag{4.7}$$

At this point the electron current to probe 2 can be written in terms of the ion current and total current.

$$\frac{I + i_{1+}}{i_{2+} - I} = \frac{A_1}{A_2} e^{(eV/kT_e)} \tag{4.8}$$

Eq.(4.8) can be solved for the electron temperature T_e once the I-V characteristic is known. This equation is difficult to use so usually the assumption that the probes are of the exact same size is made. If $A_1 = A_2$ then $i_{1+} = i_{2+} = i_+$ and Eq. (4.8) becomes:

$$I + i_+ = (i_+ - I)e^{(eV/kT_e)} \tag{4.9}$$

After a little algebra Eq.(4.9) can be written as:

$$I = i_+ \frac{e^{(eV/kT_e)} - 1}{e^{(eV/kT_e)} + 1} \tag{4.10}$$

The right hand side of Eq.(4.10) is the algebraic expression for the hyperbolic tangent so we finally arrive at Eq.(4.11).

$$I = i_+ \tanh\left(\frac{eV}{2kT_e}\right) \tag{4.11}$$

Equation (4.11) is commonly quoted in literature and can be used to solve for the electron temperature measured by a symmetric double probe. Unfortunately in practice the collection areas of the double probe, A_1 and A_2, are seldom equal on the scale of plasmas. Differences of 5-10% in the measured ion saturation currents of probes 1 and 2 are not uncommon and Eq. (4.11) fails to captures these nuances.

It is possible to derive an expression for the electron temperature that is dependant on the slope of the IV characteristic and the ion saturation currents to probes 1 and 2. As seen in Fig. 4.10, the ion saturation currents, i_{1+} and i_{2+}, are nearly constant with voltage. If we assume the ion saturation currents are independent of voltage and differentiate Eq. (4.4) with respect to V we obtain:

$$\frac{dI}{dV} = -\frac{di_{2-}}{dV} = \frac{di_{1-}}{dV} \tag{4.12}$$

Insert Eq. (4.2) for the electron currents to probes 1 and 2.

$$\frac{d}{dV}\left(A_1 J e^{(eV_1/kT_e)}\right) + \frac{d}{dV}\left(A_2 J e^{(eV_2/kT_e)}\right) = 0 \tag{4.13}$$

Now carryout the derivative to obtain Eq. (4.14).

$$A_1 J e^{(eV_1/kT_e)}\left(\frac{e}{kT_e}\right)\frac{dV_1}{dV} + A_2 J e^{(eV_2/kT_e)}\left(\frac{e}{kT_e}\right)\frac{dV_2}{dV} = 0 \tag{4.14}$$

The voltage is defined as $V = V_1 - V_2$ which we can differentiate to obtain an expression for the V_2 derivative in terms of the V_1 derivative.

$$A_1 J e^{(eV_1/kT_e)}\frac{dV_1}{dV} + A_2 J e^{(eV_2/kT_e)}\left(\frac{dV_1}{dV} - 1\right) = 0 \tag{4.15}$$

We are interested with Eq. (4.15) at the origin only. At $V = 0$, the floating potential, $V_1 = V_2$. Inserting this into Eq. (4.15) yields:

$$A_1 \left.\frac{dV_1}{dV}\right|_0 + A_2 \left.\frac{dV_1}{dV}\right|_0 = A_2 \tag{4.16}$$

This can be reduced to a simple form which will be used in our final expression for T_e.

$$\left.\frac{dV_1}{dV}\right|_0 = \frac{A_2}{A_1 + A_2} \tag{4.17}$$

With this information at the floating potential, we can revisit Eq. (4.12). At $V = 0$ we can write the following:

$$\left.\frac{dI}{dV}\right|_0 = \left.\frac{di_{1-}}{dV}\right|_0 = A_1 J \left(\frac{e}{kT_e}\right) e^{eV_f/kT_e} \left.\frac{dV_1}{dV}\right|_0 \tag{4.18}$$

Insert Eq. (4.17) into Eq. (4.18).

$$\left.\frac{dI}{dV}\right|_0 = \frac{A_1 A_2}{A_1 + A_2} \left(\frac{e}{kT_e}\right) J e^{eV_f/kT_e} \tag{4.19}$$

The saturation current density J_+ is equal to the term after the parenthesis so Eq. (4.19) becomes:

$$\left.\frac{dI}{dV}\right|_0 = \frac{A_1 A_2}{A_1 + A_2} \left(\frac{e}{kT_e}\right) J_+ \tag{4.20}$$

The ion saturation current measured by probe one is $i_{1+} = A_1 J_+$ and measured by probe two it is $i_{2+} = A_2 J_+$. Hence the equation for electron temperature is obtained.

$$\left.\frac{dI}{dV}\right|_0 = \frac{e}{kT_e}\frac{i_{1+}\cdot i_{2+}}{i_{1+}+i_{2+}} \tag{4.21}$$

From this simple equation the electron temperature can be calculated from the measured ion saturation currents to each probe and the slope at the origin. All measurements of T_e made by the combination Langmuir/Mach probe in this dissertation are calculated using Eq. (4.21) unless noted otherwise.

The electron density measured by a Langmuir probe is determined from the theory of ion collection, sheath formation and the measured values of T_e and J_+. The mechanics of ion collection and the measured ion saturation current form the basis of the formulaic approach to calculating the electron density [17]. As such, a number of different methods have been developed to deal with the problem that finite ion temperature poses. However all of these methods confirm the weak dependence of ion current on T_i when it is equal to or less than T_e therefore the Bohm theory of ion collection is appropriate and widely used. The Bohm formula is used in this dissertation and is given in Eq. (4.22). Where I_{i+} is the average ion saturation current to the probe and A_s is the surface area of the sheath which to first approximation is often taken as the surface area of the probe.

$$I_{i+} = .61eA_s n_e \sqrt{\frac{kT_e}{M_i}} \tag{4.22}$$

Chapter V: Combination Probe on TCSU

5.1 Probe Installation on TCSU

The combination Langmuir / Mach probe has been installed and operated in the midplane of TCSU and is easily moved allowing for measurements in both of the FRC exhaust jets located 1.20 meters from the midplane. Installation in the exhaust jets was simple because vertical vacuum ports were available so no extra support structure was needed and probe translation was smooth. In the midplane, however, the vertical port was occupied by the 2-axis internal magnetic field B(x,z) probe. Hence, the combination probe was installed on a vacuum port at -45° off the vertical y-axis.

The vacuum interface for diagnostics at the FRC midplane was made via standard 4.5" Conflat flanges. The large vacuum chamber comprising the TCSU confinement section was a large quartz tube with an 80 cm inner diameter and 0.6 cm wall thickness. The 4.5" Conflat flanges were welded to semi-rigid 3.5" long bellows which were attached to 2.5" diameter ports in the quartz vacuum chamber with an RTV adhesive. The vacuum seal between the quartz and the bellows was made by differentially pumping the RTV adhesive seal. G-10 support ring assemblies were mounted to each Conflat flange making them capable of supporting fairly heavy loads but not a 53" long approximately 60 lb. probe cantilevered off the end of it.

The weight of the combination probe was supported with an aluminum structure that was connected to the massive G-10 frame that held the TCSU confinement section in place. The G-10 confinement section frame has a radius of curvature of 24" so small mounts, made of 304 stainless steel, were built with the same radius of curvature. 3/8"-24 helicoils were inserted into blind holes drilled into the G-10 frame and the stainless

steel mounts were bolted into these threaded holes. The 1/2" thick combination probe support structure was constructed with 6061 aluminum and was connected to the stainless steel mounts with 3/4" steel dowel rods and cotter pins. A picture of the combination probe installed in the TCSU midplane is shown in Fig. 5.1.

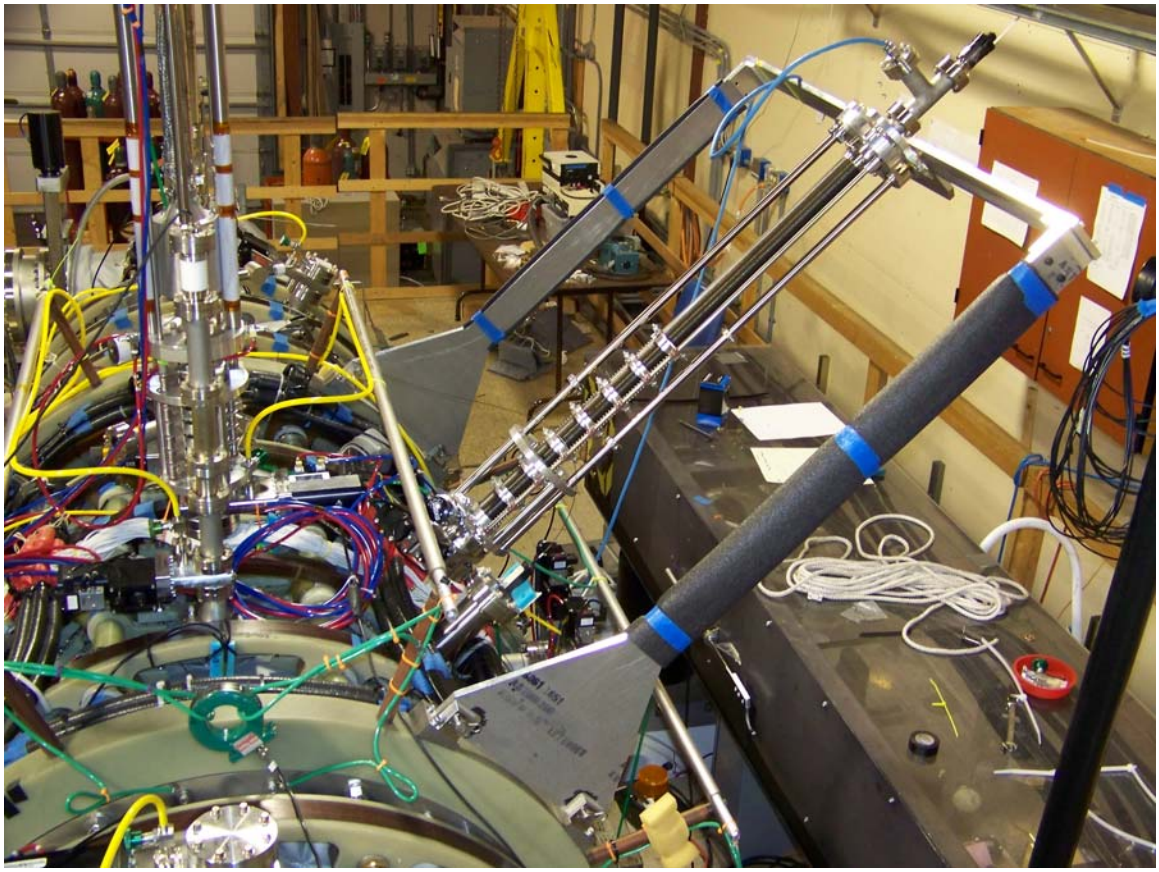

FIG. 5.1 Langmuir / Mach probe installed in the TCSU midplane in the fully retracted position. The probe sits behind a 4.5" UHV compatible gate valve that can be closed to protect the probe during glow discharge cleaning or Ti-gettering. It also allows the probe to be moved to a new location without undergoing a vacuum break.

Once the combination probe was installed on TCSU a 24’ shielded cable was built to connect the probe to the power supply. A 9-pin D-sub vacuum feedthrough was used to make the electrical connection at the probe and at the power supply. To minimize the noise pickup 8 small coaxial signal wires were connected to the 8 probe tips. The connection to the probe was made with the center conductors only. The 8 wires were all twisted together and then pulled through a tube of heat shrink that was cut to the length of the wires, approximately 24’. The heat shrink was then reduced to make one self contained cable. This cable was then fit through a sheath of copper braid that was cut to the length of the cable. The cable, with the copper braid sheath in place, was then pulled through another tube of heat shrink. The outer layer of heat shrink was activated with a hot air gun resulting in a flexible 3/8” diameter, shielded cable containing 8 small coaxial signal wires.

At this point the center conductors of the eight coxail wires were soldered to D-sub connectors at each end, a male connector was used at the power supply side and a female connector was attached at the other end to make the connection to the vacuum feedthrough at the probe. The braided outer conductors of the coaxial wires were then soldered to the large outer braid enclosing the entire cable at the power supply side only. A small hole, just large enough for the cable, was punched out of the steel power supply enclosure. The cable braid was then stretched through this clearance hole and electrically connected on the inside of the power supply enclosure. With the power supply enclosure grounded this provided a sufficient shield for the combination probe electronics and wiring all the way to the vacuum feedthrough connector.

Inside the TCSU vacuum, priority number one was to ensure no electrical connection could be made between the plasma and the vacuum boundary. To that end, a grounded shield could not enclose the probe wires from the vacuum feedthrough to plasma exposed probe tips. Since the main source of signal noise affecting the probe in vacuum is from the high frequency RMF antennas a conducting shield must still be used

to block as much noise as possible. The probe wires were shielded by the stainless steel 5/16" diameter probe mounting pipe, which connected via 15 kV electrical isolation to the rotary motion vacuum feedthrough. Attached to the end of the probe mounting pipe, using a collar and retaining ring, is the 1/8" diameter stainless steel tube on which the plasma facing, interlocking boron nitride probe stalk was assembled. Thus the probe wires were twisted and shielded by stainless steel from the vacuum feedthrough to the end of the 1/8" diameter internal probe stalk where they fanned out to connect to their respective probe tips.

Before the gate valve isolating the combination probe from the ultra-high vacuum of TCSU could be opened the air in the probe bellows must first be evacuated. This was easily accomplished through the use of a 1.33" mini-conflat flange pump-out port located on the air side of the gate valve. A portable pumping system, with a turbo-pump, roughing scroll pump and ion gauge, is attached to the pump-out port on the gate valve to pump the combination probe to a 10^{-7} Torr high vacuum level. The probe is then wrapped with heater tape and insulating blankets and baked at 200° C for an extended period, minimum 12 hours, to liberate water vapor and other impurities from the probe surface. Only after this is finished can the gate valve be opened and the probe exposed the TCSU vacuum system.

5.2 Probe Operation in TCSU

The combination probe on TCSU has successfully acquired data in the FRC midplane and in the exhaust jets. Langmuir measurements have been made using a steady bias voltage and more commonly by sweeping the bias voltage, usually at 10 kHz. Successful Mach probe measurements have been made at the FRC field null where the density is the highest. The Mach probe tips were made too small to capture data outside the field null or in the FRC exhaust jets where the density is an order of magnitude less than it is at the field null. Due to the strict operation schedule of TCSU a redesign of the Mach probe tips was not attempted.

In the previous TCS experiment Langmuir probe data was not successfully attained using a swept bias voltage. The RMF current drive creates a noisy and turbulent environment making electric probe operation difficult. It should be noted that the author was not involved with the Langmuir probe operation in the TCS experiment and the drive circuit design and signal capture methods used were not employed in the Langmuir probe installed on the TCSU experiment.

The first Langmuir data recorded on TCSU was acquired using the double probe method with a constant bias voltage on the probe tips. Although every precaution was taken to minimize signal noise due to the RMF current drive it was still present, but the underlying Langmuir signal was clearly visible. Fig. 5.2 shows the Langmuir probe current measured with a Pearson probe using a 54 volt bias on the probe tips. The blue trace is the raw data and the red trace is the same data with a 50 kHz lowpass filter applied.

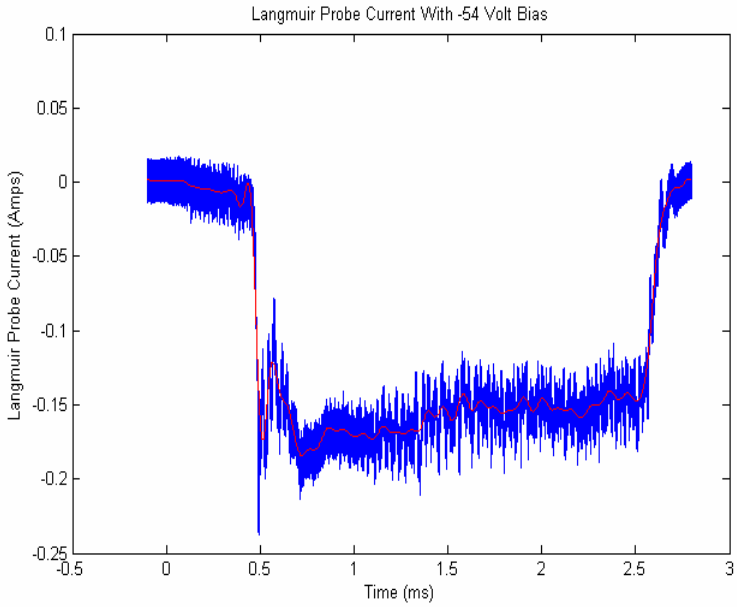

FIG. 5.2 Langmuir probe current measured in the circuit with a Pearson probe. The blue trace is the raw data showing the main source of noise on the signal is due to the RMF. The red trace is the same signal with a 50 kHz lowpass filter applied.

Due to the careful placement of the probe tips in the design stage, the rigorous cleaning methods employed before assembly, and the care taken during construction of the probe, arcing between the probe tips was rare. Since arcing was not a major problem with the combination probe, data acquisition was relatively simple and could be accomplished in a timely manner. Although uncommon, it is vitally important to protect the probe tips from melting during an arc by limiting the current in the probe circuit with a 50 Ω resistor.

As stated above, many probe scans were done by sweeping the applied bias voltage to the probe tips, but before that was attempted a shot to shot scan was done by changing the fixed bias voltage by 5 or 6 volts from one shot to the next. This shot to shot scan represents the first data taken with the Langmuir probe in TCSU and is by no means an ideal way to measure the electron temperature or density. This data was also

taken while the TCSU experiment was being operated with an 87 kHz even-parity RMF frequency that produced an FRC which would only reach a total temperature of roughly 40 eV as calculated from pressure balance. The optimal RMF frequency for even-parity operation was 122 kHz which produced FRCs with an approximate total temperature of 60 eV. Nevertheless, a shot to shot scan was completed with the Langmuir probe positioned at the FRC field null (R = 28 cm). By varying the bias voltage the current vs. voltage trace is known for the entire life of the FRC. The following figure shows the Langmuir probe current plotted against the applied bias voltage at a specific time during the quiescent phase of the FRC, 1.3 ms.

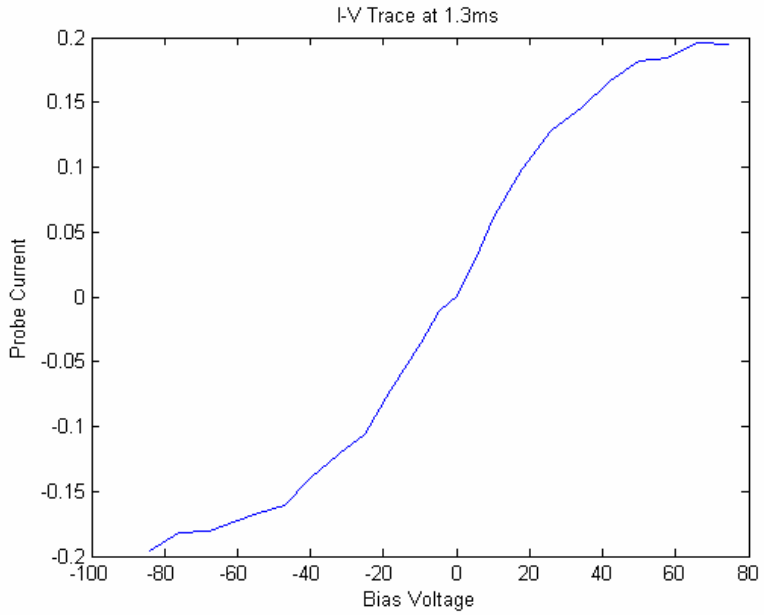

FIG. 5.3 The Langmuir probe current at the field-null is plotted against the bias voltage applied to the probe tips at 1.3 ms for a 87 kHz RMF driven FRC. This data was acquired by changing the fixed bias voltage from one shot to the next.

Once the Langmuir measured I-V characteristic of a plasma is known the electron temperature can be calculated from Eq. (4.21), which is derived in the preceding chapter. Since this data was gathered from a shot to shot sweep of the bias voltage the I-V trace is known for every time sample recorded by the digitizer. This does not mean that a precise time history of the electron temperature is known since any high frequency oscillations are the result of small variations in the plasma from one shot to another, but the overall profile is accurate. The electron temperature is calculated by measuring the slope of the curve at the origin and the ion saturation currents for each trace, and is plotted in Fig. 5.4.

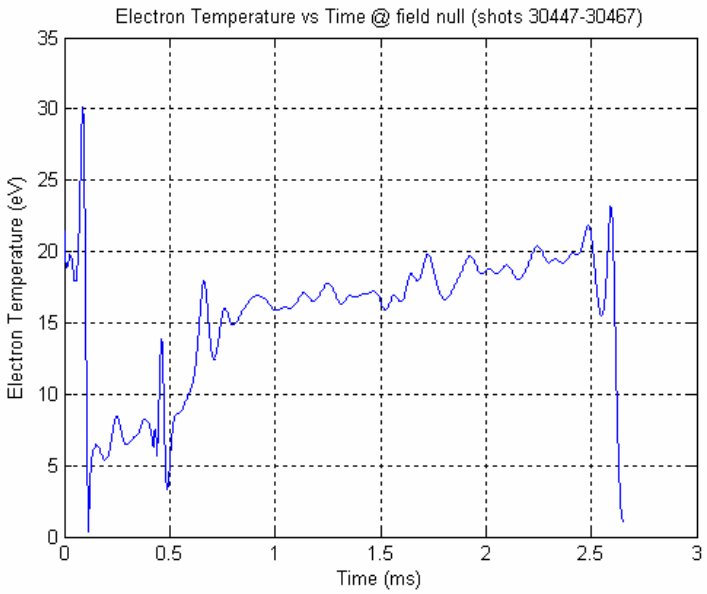

FIG. 5.4 The electron temperature as measured by the Langmuir probe at the field null of a 87 kHz RMF driven FRC. The data was recorded using a shot to shot sweep of the bias voltage applied to the probe tips.

The simply-connected, cylindrical geometry of a FRC allows for the calculation of the total temperature $T_t = T_e + T_i$ and the density profile in the plasma through the use of pressure balance. In the TCSU machine, the line integrated density measured by the interferometer and the radial profile of the azimuthal and axial magnetic fields, B_θ and B_z respectively, measured with the 2-axis internal magnetic probe are used to solve for the radial pressure profile, p, in the following pressure balance equation.

$$p + \frac{B_z^2}{2\mu_0} + \frac{\langle B_\theta \rangle^2}{4\mu_0} + \int_0^r \rho \Omega_i^2 r dr = C \tag{5.1}$$

In a field-reversed configuration plasma that is not formed or sustained by a rotating magnetic field the plasma pressure is balanced by the second term only. In TCSU, the bulk of the plasma pressure is balanced by the magnetic pressure generated by the axial magnetic field, but the RMF does affect the plasma pressure to a small degree and this is taken into account in Eq. (5.1). The third term represents the ponderomotive force that arises from the oscillating $J_z B_\theta$. The brackets around B_θ represent the time-average over an RMF cycle. The effect of ion rotation is also included and is embodied in the fourth term. The RMF imparts a net torque on the FRC which causes the electrons to rotate. The electrons transfer some of their torque to the ions so they rotate in the same direction. From ion Doppler spectroscopy and measurements with the Mach probe the ion rotation frequency, Ω_i, is found to be fairly constant and is usually set at 10 kHz.

The plasma pressure is determined in Eq. (5.1) by first finding the value of the integration constant, C. The constant is calculated at a location where the plasma pressure is zero but, as this is an iterative process, it can be adjusted later. At this point the pressure profile can be calculated because all of the other terms are known. Since $p(r) = n(r)k_B T_t$ we can calculate the number density, $n(r)$, by first assuming the total temperature is constant. Then we use the constraint that the line integral of the calculated density matches the line integral $\int n(r) dl$ from the interferometer measurements. In this

way the total temperature and density profile can be adjusted in a few iterations until all of the conditions are satisfied and the calculated values of $n(r)$ and T_t are known.

In the following figures the calculated total temperature and density is plotted along with the electron temperature and density measured with the Langmuir probe. Although the measurements were made using a shot to shot sweep of the bias voltage, fair agreement with the values calculated from pressure balance is attained. As expected, the electron temperature is approximately half of the calculated total temperature.

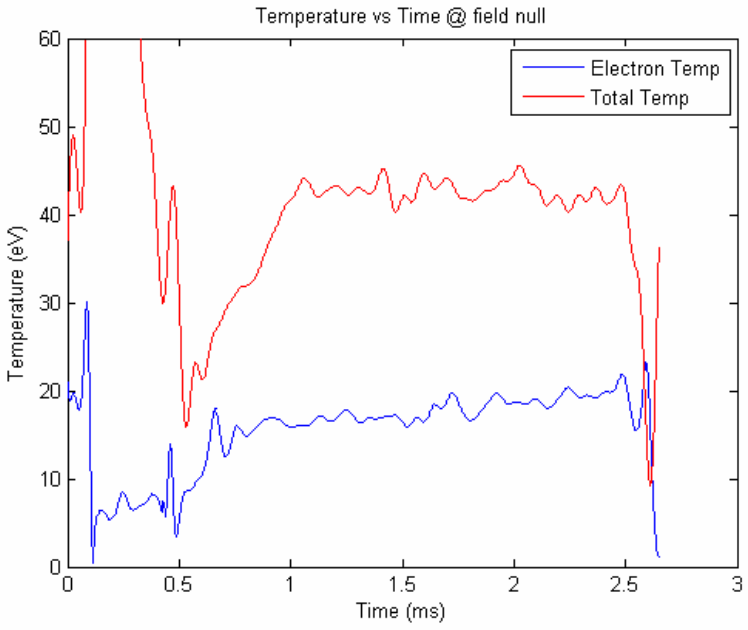

FIG. 5.5 The electron temperature measured with the Langmuir probe and the total temperature calculated from pressure balance are plotted together.

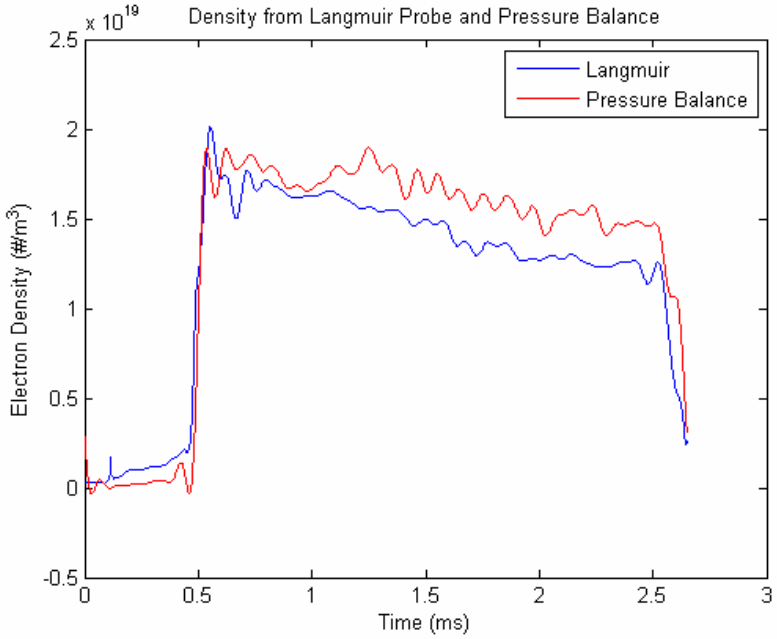

FIG. 5.6 The electron density measured with the Langmuir probe and density calculated from pressure balance at the field null are plotted together.

Once these measurements were completed the Langmuir probe was set to begin taking data by sweeping the applied bias voltage. A few different sweep frequencies were tested but the best results were attained at 10 kHz. Each time the bias voltage is swept from negative to positive the electron temperature and density can be measured. At 10 kHz a full cycle is completed in 100 μs. It was seen during testing that the output voltage from the Langmuir probe drive circuit began to drift when it sent a continuous 10 kHz waveform to the probe tips. This was due to the fact that the electronics had to be located about 20 feet from the probe and the long cable length connected to open probe tips acts like an antenna setting up an impedance mismatch. Steps were taken to counteract this imbalance such as inserting a load resistor in parallel with the probe output and adjusting the capacitance in the gain circuitry, but a small variable drift remained. The best solution to this voltage drift was setting the output voltage to zero.

But a Langmuir probe that sweeps once during the 2.5 ms FRC lifetime is not very useful so a little trial and error was used to find the minimum time between sweeps such that the voltage drift was negligible. 25 μs was found to be an acceptable amount of time for the Langmuir drive electronics to zero out so the waveform generator was triggered every 125 μs. In this way 20 data points were taken during the FRC discharge so a decent time history of each shot was recorded. Fig. 5.7 shows the voltage applied to the probe tips and the resulting current measured in the probe circuit.

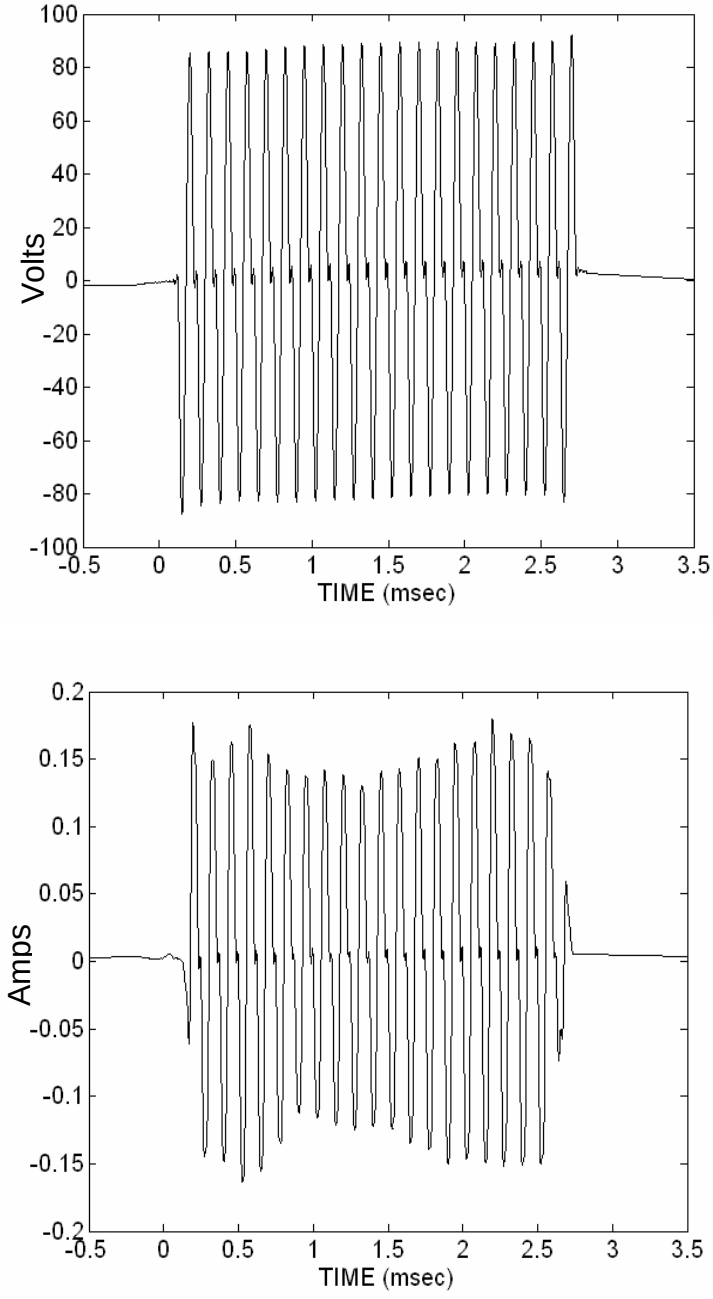

FIG. 5.7 The Langmuir probe voltage and current. A 10 kHz triangle wave is sent every 125 μs so 20 data points are collected during the 2.5 ms FRC.

Chapter VI: Combination Probe Results

6.1 FRC Parameters for Even and Odd Parity RMF Operation

To develop the radial profile of the electron density and electron temperature of an FRC, Langmuir probe measurements must be made at multiple radial positions. A shot to shot scan is performed in which the measuring probe tip is moved from one radial position to another, usually in 2 cm increments, from the center axis, R = 0 cm, to the vacuum chamber wall at R = 40 cm. Data is taken at a given radial location and as long as there is no probe arc or some other anomaly it is moved to the next position. To ensure the measured radial profiles are accurate the FRC must be stable and repeatable. A consistent operating regime was found in which the differences measured with the available diagnostics from one FRC to the next were very small. This was managed for both even and odd parity RMF operation. Data from a number of different diagnostics for both even and odd parity operation is shown in Fig. 6.1. These are the types of FRCs for which Langmuir and Mach probe data were taken at the midplane and in the exhaust jets and a complete analysis of the convective power losses is given. As can be seen, odd-parity operation produced more stable and time independent results after the approximately 700 μs formation phase.

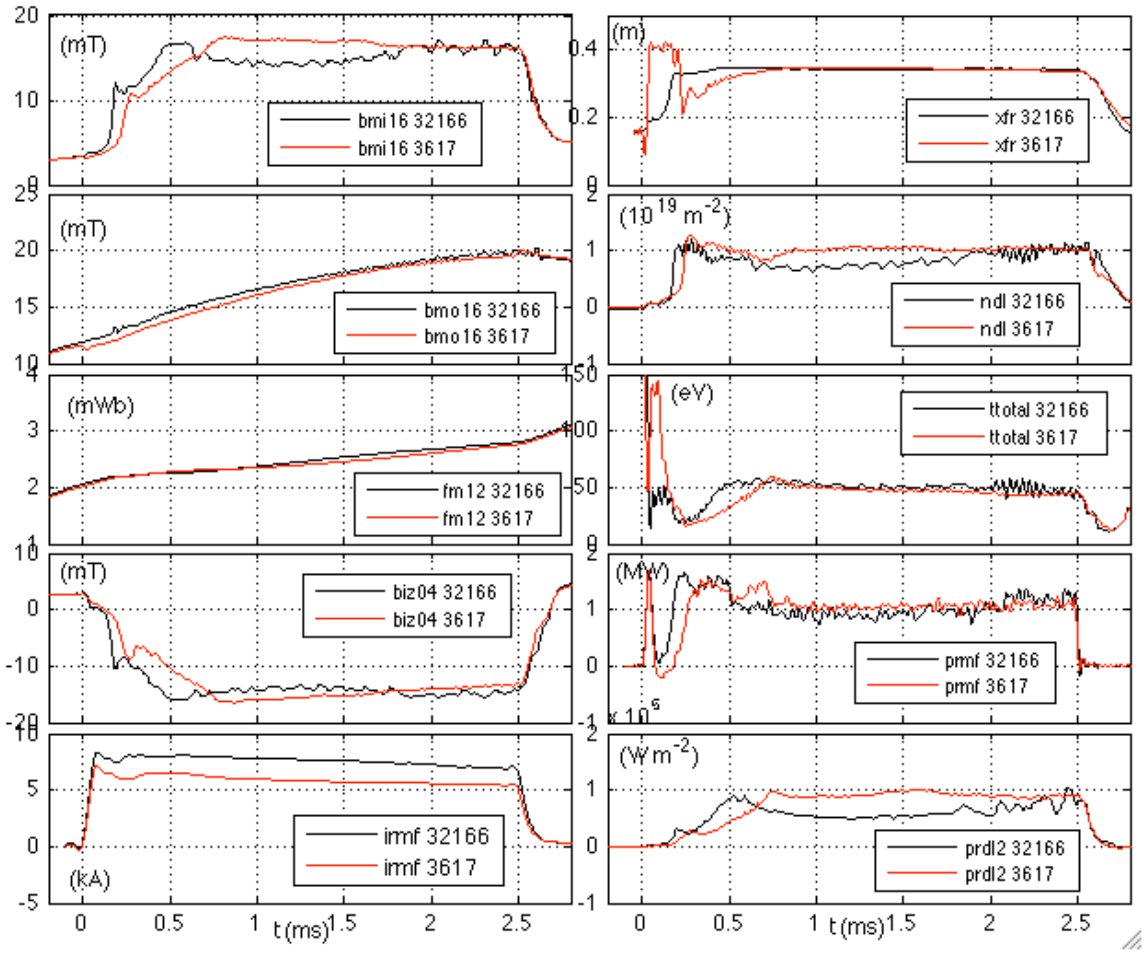

FIG. 6.1 Plasma parameters measured by a number of diagnostics for both even-parity (black) and odd-parity (red) RMF operation.

The left column of Fig. 6.1 shows bmi16, which is the magnetic field measured just within the internal flux rings at approximately R = 38 cm, and bmo16 which is the magnetic field measured just outside the flux rings at approximately R = 39.5 cm. The third pane in the left column shows a plot of fm12 which is the flux measured with a loop wrapped around the vacuum chamber at roughly R = 42.5 cm. Biz04 is shown in the fourth pane of the left column and this signal is the measured internal magnetic field at the center axis, R = 0 cm. It is almost a mirror image of bmi16 indicating that full reversal of the axial magnetic field is achieved. All of the signals discussed so far are measured at the midplane of the FRC, Z = 0 cm. The final graph in the left column is the total current in the RMF antennas. The RMF current I_{rmf} is calculated from the current measured in the vertical and horizontal RMF cradles, I_{vert} and I_{hor} respectively, by the following: $I_{rmf}^2 = I_{vert}^2 + I_{hor}^2$.

The right column of Fig. 6.1 shows a plot of the excluded flux radius at the midplane as denoted by the signal name xfr. The excluded flux radius is calculated from the bmi and bmo diagnostics and from the external flux loop data denoted with the signal name fm. The line integrated density measured with the interferometer is shown in the second pane of the right column. The total temperature is plotted in the next graph. The total temperature is calculated from pressure balance and is explained in Chapter 5. The RMF power is shown in the fourth graph of the right column. This is a fair estimate of the total input power to the FRC and will be discussed in further detail. Finally the radiated power measured with a bolometer is shown in the plot of prdl2.

The diagnostic measurements in Fig. 6.1 describe two FRCs which are rather similar, considering the RMF current drive responsible for the formation and sustainment of these FRCs is very different. There are a few differences which should be noted though. The inductance of the RMF antennas is higher in the odd-parity configuration so a similar input power is reached even though the RMF current is considerably lower. The RMF power supply is charged to 12 kV for both FRCs as can be seen in Table 6.1 which

also shows the voltage in the capacitor banks for the axial magnetic field coils and the time at which they fire. Time zero is when the RMF fires. The pressure and timing of the deuterium gas puff valves is also included.

Module/time	122 kHz Even	107 kHz Odd
RMFP	12 kV	12 kV
RMF time	0 to 2.5 ms	0 to 2.5 ms
ENSP	1000 V	1000 V
ENSP time	-15 ms	-15 ms
CCP	250 V	250 V
CCP time	-9 ms	-9 ms
CEP	125 V	125 V
CEP time	-14 ms	-14 ms
CMP	340 V	350 V
CMP time	-1.5 ms	-2 ms
PUFF1	8.5 psia	16 psia
puff1 duration	-25 to -22.5 ms	-25 to -24.78 ms
PUFF2	35.5 psia	52 psia
puff2 duration	-3.7 to +2 ms	-3.5 to +3 ms

Table 6.1 Description of the TCSU operating conditions for even and odd parity RMF. The charge voltage and timing of the RMF antennas, the axial magnetic field coils, and the pressure and duration of the deuterium gas puff valves is listed. RMFP is the RMF power supply, ENS are the end north and south magnets which start 1.8 m from the FRC midplane, CC are the cone magnets located 1.5 m from the midplane, CE are the center-end magnets over the ends of the FRC and the exhaust jets (where Langmuir measurements are made), and CM are center-midplane magnets under the RMF antennas.

The total temperature achieved is approximately equal but the density of the odd-parity FRC is noticeably higher, especially during the quiescent or steady-state phase from 1 to 2 ms. This alone indicates better performance from the odd-parity FRC since it reaches a similar temperature at a higher density and is thus slightly more energetic. The stability of the odd-parity FRC may also be slightly better than it is for even-parity operation. The even-parity FRC can be affected by an n=2 instability. A clear example

of an n=2 unstable FRC is shown in Fig. 6.2 [18]. Although there is no n=2 instability in the FRCs plotted in Fig. 6.1 or in any of the FRCs used in the Langmuir probe scan it can become a problem by increasing the axial magnetic field by as little 1 to 2 mT which equates to increasing CMP by about 20 volts. This is not to say that the odd-parity FRC is perfect in comparison as it will also go highly unstable if the axial field is increased by a few millitesla. It is not an n=2 instability that destroys the odd-parity FRC but a catastrophic failure where field reversal is lost and the FRC crashes, then builds back up. This repeats a few times such that a plot of the internal magnetic field (biz04) would show a saw-tooth pattern.

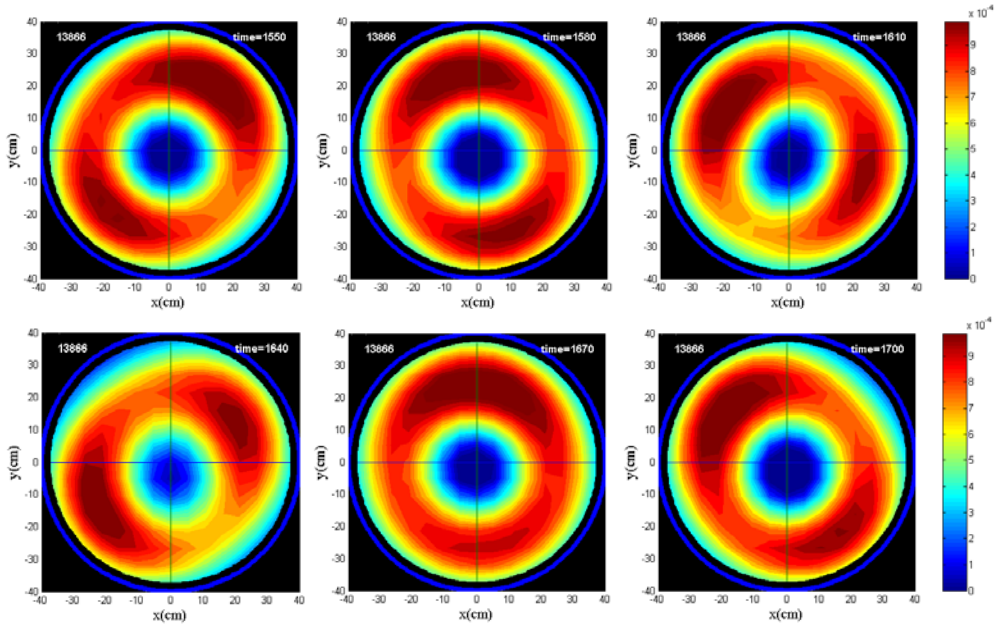

FIG. 6.2 Abel inverted visible light tomography data showing the cross section of an n=2 unstable FRC.

6.2 Combination Probe Data for the 122 kHz Even-Parity FRC

6.2.1 FRC Midplane Results

With the Langmuir probe at the midplane of the TCSU confinement section a radial scan was completed for the 122 kHz even-parity RMF driven FRC. The current and voltage in the probe circuit is recorded by a 12-bit digitizer. The local electron temperature and electron density in the plasma at the probe tips is calculated using the double probe method derived in Chapter 4. The probe is swept with a 10 kHz triangle waveform that is triggered every 125 μs. In this way the probe can accurately measure T_e and n_e 20 times during a 2.5 ms plasma shot.

To generate a smooth radial profile multiple shots are taken at a given location until all traces from several key diagnostics overlay the baseline outlined in Fig. 6.1. The electron temperature is calculated from Eq. (4.21). Fig. 6.3 shows the electron temperature measured with the Langmuir probe while the probe was positioned at R = 26 cm which is very near the FRC field null, also known as the magnetic o-point. The total temperature calculated from pressure balance for the 122 kHz even-parity baseline graph in Fig. 6.1 is plotted with the Langmuir measured electron temperature. This is done to show that the electron temperature is approximately half of the value of the total temperature.

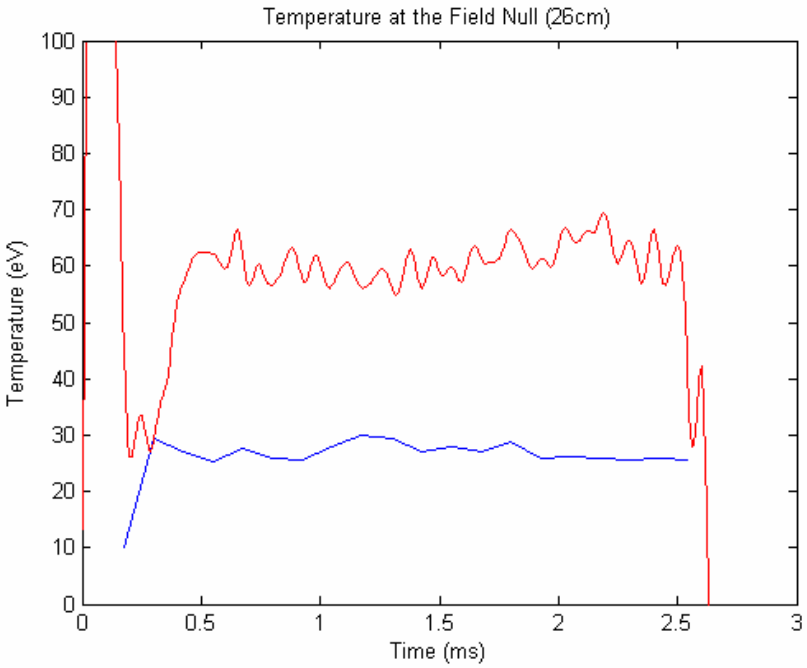

FIG. 6.3 The electron temperature (blue) measured with the Langmuir probe is plotted with the total temperature (red) calculated from pressure balance.

Similar measurements are made every 2 cm from the center axis all the way to the internal flux conserving rings at R = 38cm. A 3-D surface plot is shown in Fig. 6.4 which contains the electron temperature plotted as a function of time and radius. This shows a flat electron temperature profile of approximately 30 eV. The FRC does not appear to be heating up over time nor is there any localized region of increased temperature. Of course the Langmuir probe swept at 10 kHz is not capable of instantaneous measurements. Instead the data of value is captured over a period of 50 μs so it captures more of an average value of temperature and density.

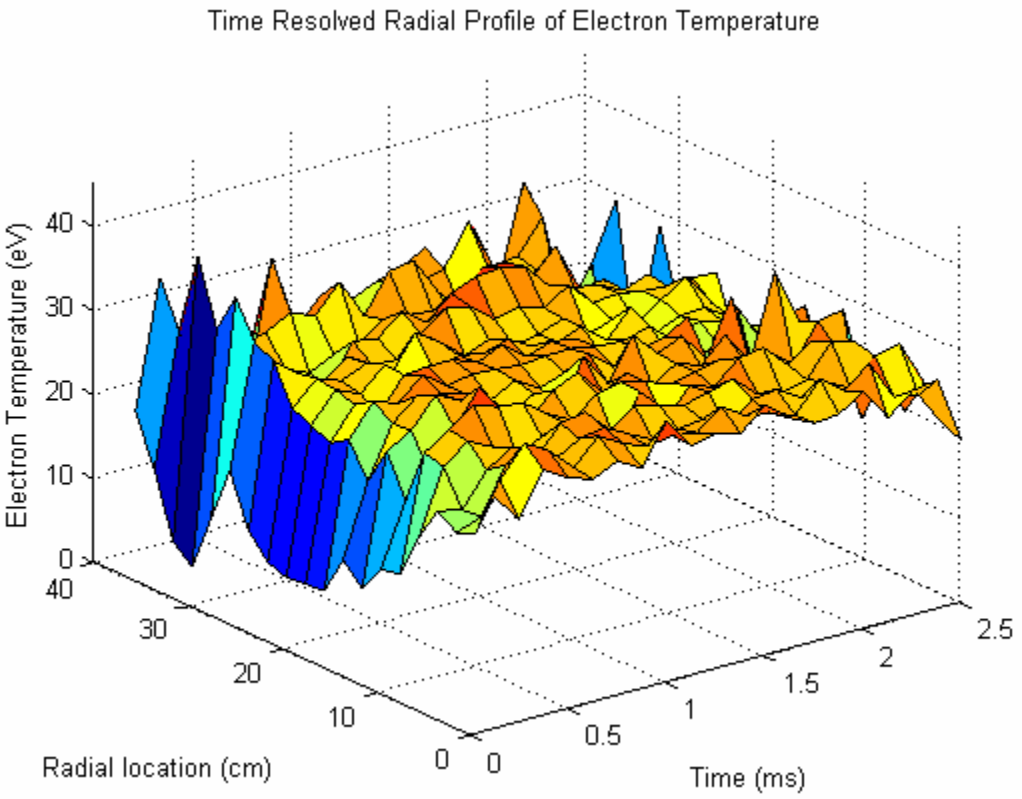

FIG 6.4 3D surface plot of the electron temperature for the 122 kHz even-parity RMF formed FRC.

The data in Fig. 6.4 is fairly smooth with spikes not greater than 4 eV more or less than the average value seen. Most of the rough data is seen at large radius near the flux conserving rings where the FRC density falls off quickly. At low density the particle flux to the probe tips is small so the current being measured in the circuit is low. Noise from the RMF is also higher at large radius because of the proximity to the antennas. The RMF is also constantly sweeping in particles from outside the seperatrix making the plasma is this region more turbulent.

A nearly instantaneous measurement of the electron temperature at 1.5 ms has been made with Thomson scattering [19] and is shown in Fig. 6.5. Multi-point

Thomson scattering was used on TCSU capable of electron temperature measurements at 5 spatial locations from 10 cm to 25 cm. A radial plot of the electron temperature measured with the Langmuir probe is also shown for comparison.

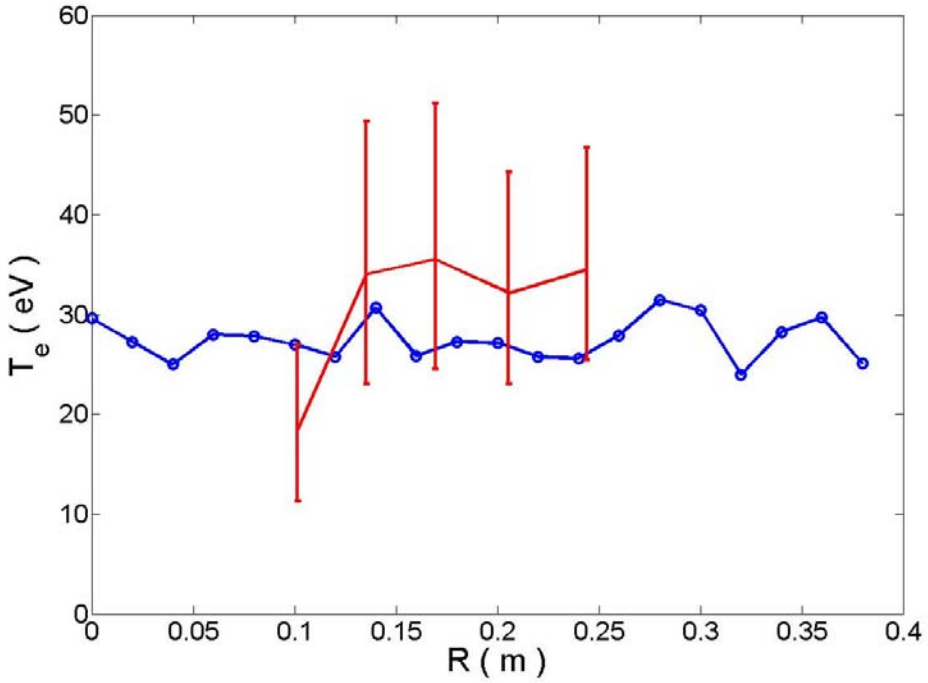

FIG. 6.5 Radial profile of the electron temperature at t = 1.5 ms measured with the Langmuir probe (blue) and Thomson scattering (red).

Once the electron temperature is known the electron density can be calculated using the method outlined in Chapter 4. For every location and time that T_e is calculated the corresponding value of n_e is also calculated using Eq. (4.22). In Fig. 6.6 the density at the field null is plotted. The density measured with the Langmuir probe agrees very well with the density calculated from pressure balance using the line integrated density measured with the two-pass CO_2 laser interferometer (denoted by the signal name ndl) which is also shown for clarity.

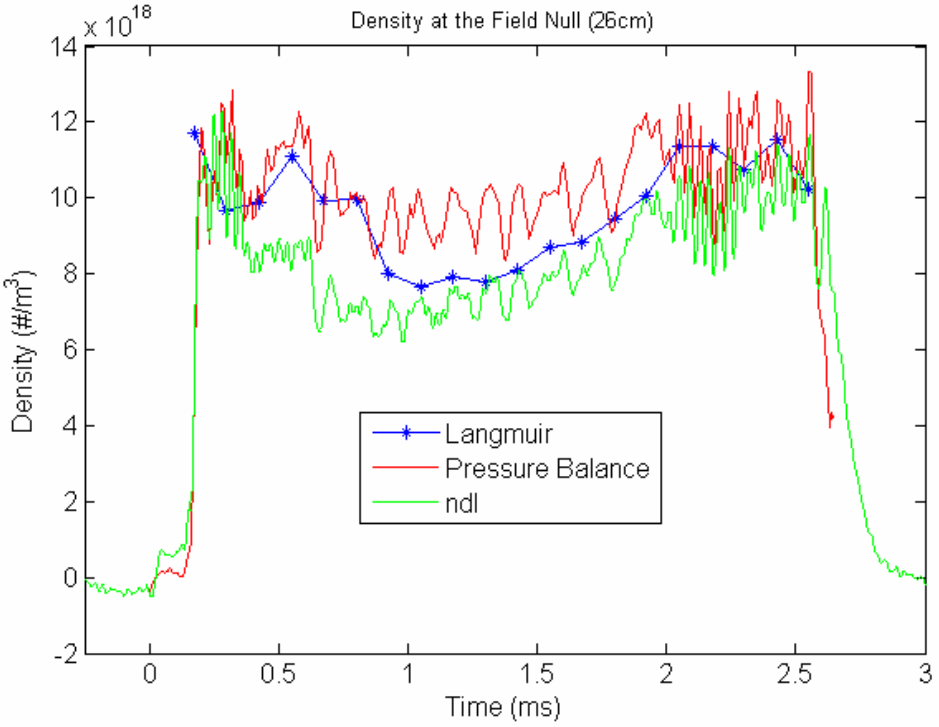

FIG. 6.6 Electron density at the field null measured with the Langmuir probe, calculated from pressure balance, and the line integrated measurement made with the interferometer. The signal ndl is not in units of m^{-3} and is only shown for comparison purposes.

The electron density was measured at all radial locations. A 3-D surface plot of n_e as function of time and radius is shown in Fig. 6.7. The density is directly proportional to the largest current measured, the ion saturation current. Since this is the case the density tends to be less affected than the temperature when sampling regions of low particle flux. The slope of the current at zero bias voltage is a very small term since you are only interested in the value of the current when probe voltage sweeps through zero. This value is indirectly proportional to the electron temperature and in an area of low particle flux to the probe tips it becomes difficult to measure which causes the calculation of temperature to become a little noisy. Although the equation for n_e depends on T_e it is only to the -1/2 power so the effect of the left hand side of Eq. (4.21) is reduced.

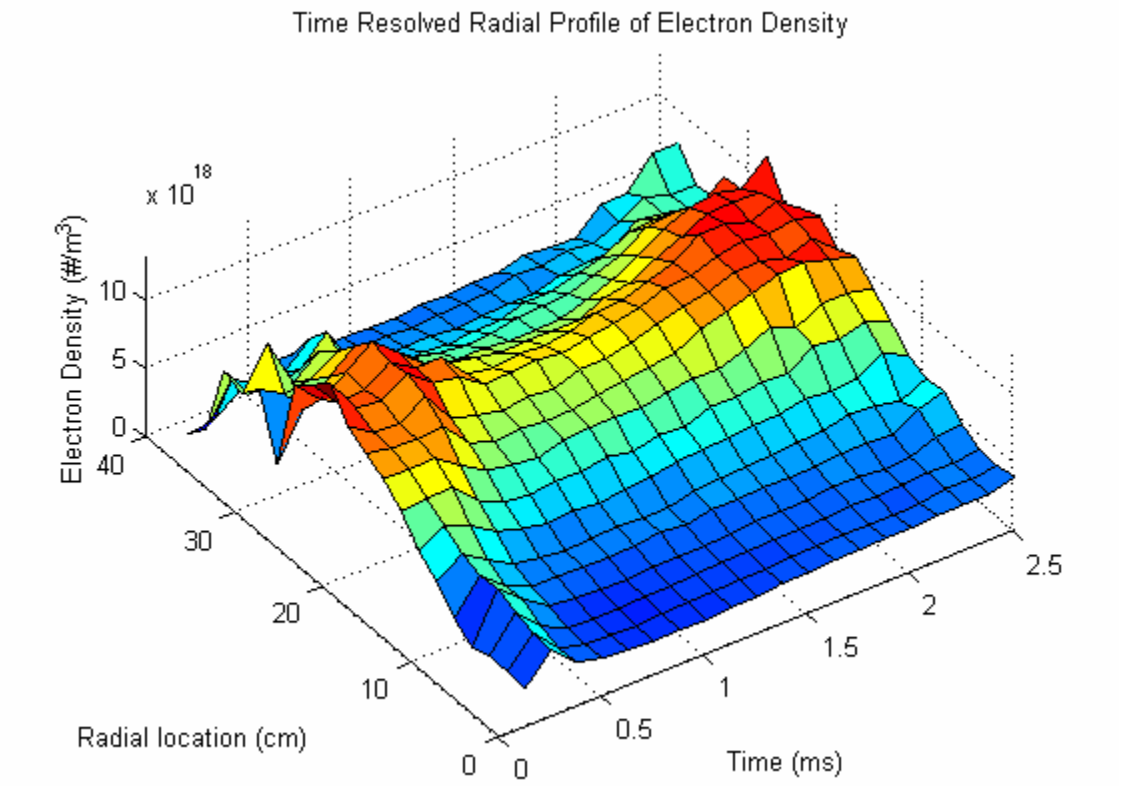

FIG. 6.7 3D surface plot of the electron density for the 122 kHz even-parity RMF formed FRC.

Similar to Fig. 6.6 the surface plot of the electron density shows the density rises quickly after the RMF is turned on then drops by about 20% during the steady state phase. At about t = 1.5 ms the density ramps up again. Although a surface plot is a good way to visualize the cross section of the FRC at the midplane, some interesting features emerge when the Langmuir measured density is compared with other density measurements. If we plot the electron density at a few points in time as a function of radius we notice a major difference between the results from Langmuir probe and those coming from the calculation of the density profile from pressure balance.

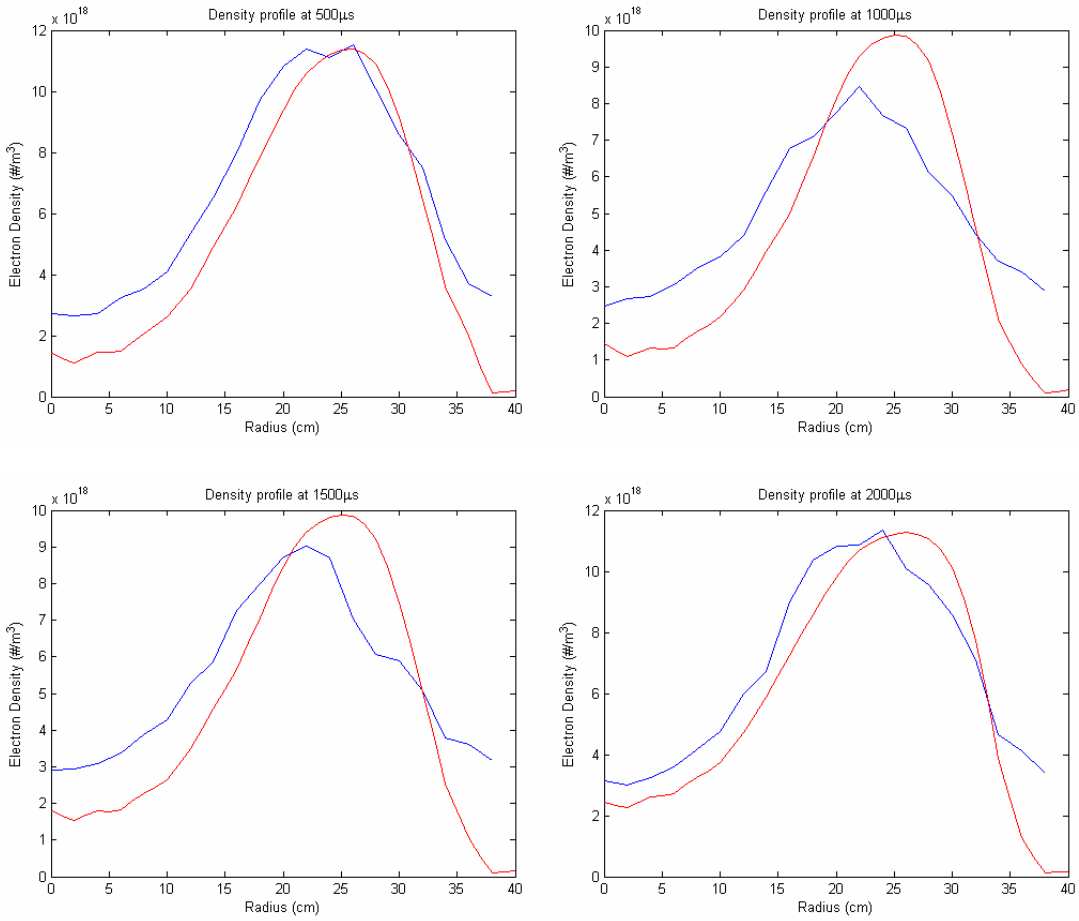

FIG. 6.8 The electron density measured with the Langmuir probe (blue) and calculated from pressure balance (red). The profile is shown at four separate time points: t = 0.5 ms, t = 1.0 ms, t = 1.5 ms, and t = 2.0 ms.

In Fig. 6.8 the electron density profile results from the Langmuir probe and from pressure balance are compared. While the maximum density measured is similar at the start of the plasma shot and towards the end, the peak density recorded by the Langmuir probe is noticeably lower during the steady state phase. A drop in average density is also seen by the interferometer during steady state. It should be noted that a shot to shot scan must be completed in order to obtain a radial density profile from the Langmuir probe while the density profile calculated from pressure balance is for a single shot, in this case

shot number 32166 which has been used as our 122 kHz even-parity baseline throughout this chapter. The line integrated density measured by the interferometer and shown in Fig. 6.6 is also for shot number 32166. While some error is introduced into the radial profiles measured with the Langmuir probe the utmost care was taken to ensure that data used in compiling this profile was from a shot that was as close of a match to shot 32166 as could be asked for. In the simplest terms this means that traces from multiple diagnostics, including those used in Fig. 6.1, would basically lie on top of each other with the only difference being seen in the small amplitude, high frequency oscillations (noise).

As previously outlined the radial density profile for any given shot derived from pressure balance is heavily dependent upon the measurement made with the interferometer for the same shot. The double pass CO_2 interferometer used on TCSU is an invaluable diagnostic for density measurements but it is also extremely sensitive. The optics tables on which the laser and beam path are mounted are placed on 2500 lb. pillars that sit on the concrete building foundation. This is done to keep any vibrations that could be recorded by the interferometer to a minimum. An example of how an incorrect reading from the interferometer can affect a quantity calculated from pressure balance is shown in Fig. 6.9. These two shots were basically identical according to every other diagnostic but a mechanical vibration can be seen in the signal from the interferometer. This is clear at the end of the shot. For our baseline shot (32166) the interferometer signal goes to zero when the shot ends but for the other shot the signal never falls to zero because there is some physical disturbance disrupting the measurement. These disturbances can last a few milliseconds so if we see the interferometer signal (ndl) begin or end at a value other than zero we know the measurement is corrupted.

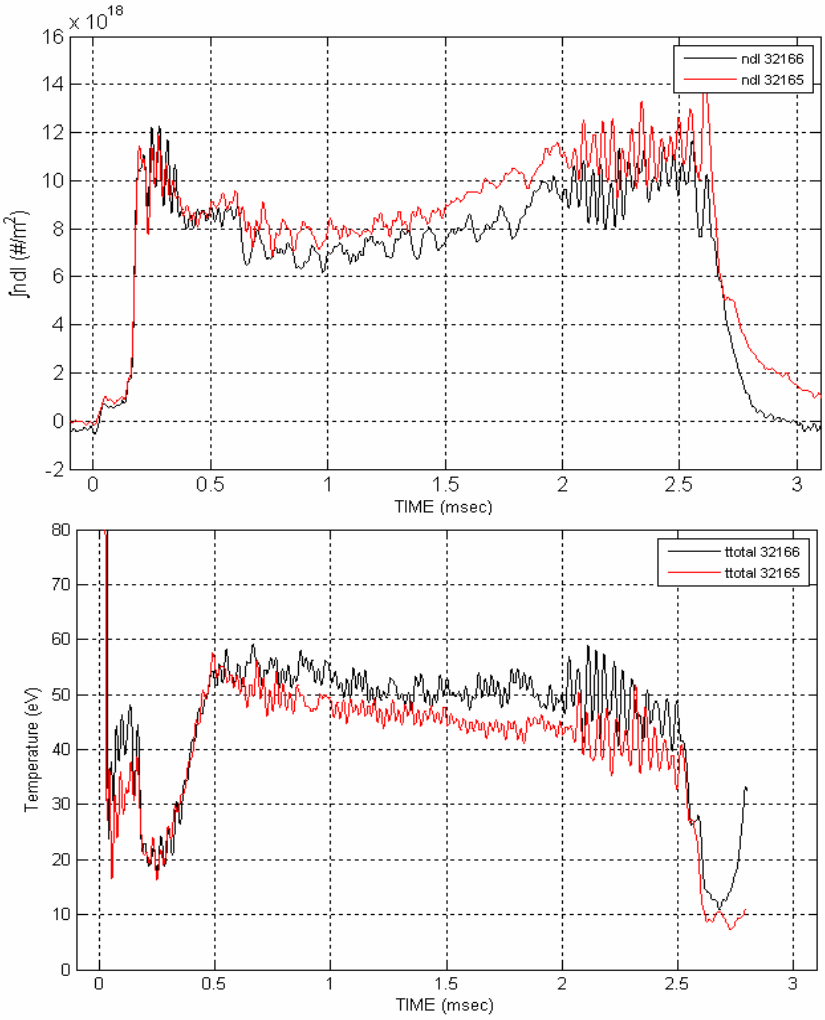

FIG. 6.9 A comparison of two shots. For shot # 32166 the interferometer is working properly and for shot # 32165 a mechanical vibration has corrupted the signal. Its effect on pressure balance is shown in the graph of T_t.

Although the maximum value of density when calculated from pressure balance can be affected by the interferometer the overall shape of the curve is not. A clear discrepancy between the two density profiles in Fig. 6.8 is the outward pressure shift apparent in the pressure balance curve. This shift is seen in all profiles inferred from pressure balance for an even-parity RMF formed FRC. The Langmuir probe measures a wider profile. The Langmuir measurement on the outer field lines is probably not as

accurate as it is on the inner lines but this effect is small and it is due to the noise from the RMF. The curve of the Langmuir measured profile on the inner lines is smooth and takes the shape predicted. But it clearly shows the density on inner fields is a little bit higher than we previously thought.

The electron density can also be measured with Thomson scattering. In Fig. 6.10 the density measured with Thomson scattering for a 122 kHz even-parity FRC is plotted with the Langmuir measured radial density profile and the profile from pressure balance. The density measured by the Thomson scattering is in excellent agreement with the profile compiled with the Langmuir probe.

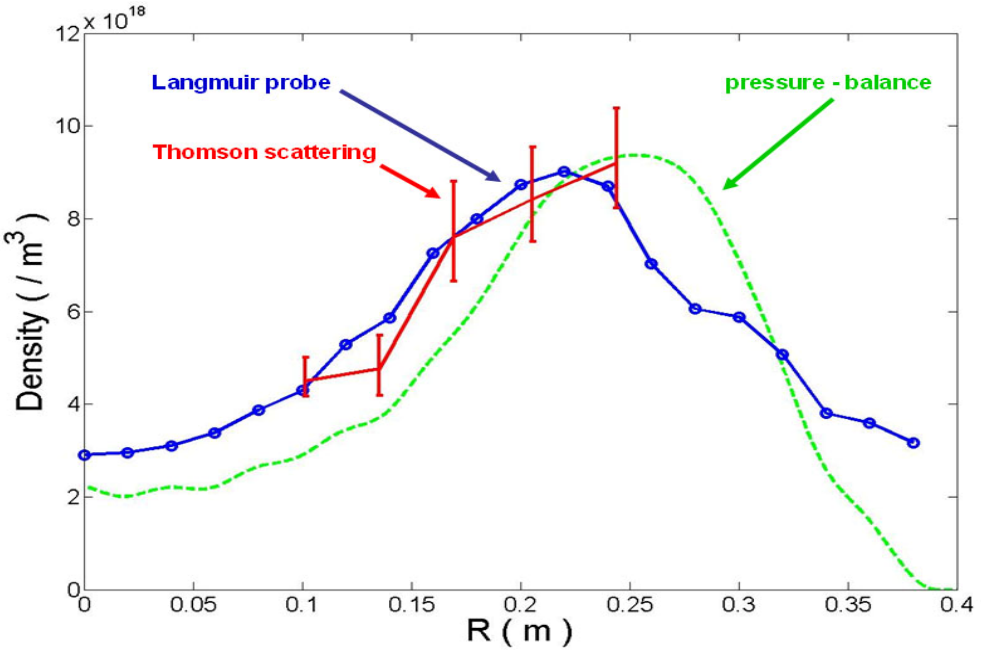

FIG. 6.10 A radial profile of n_e measured with the Langmuir probe and Thomson scattering is compared to the profile inferred from pressure balance.

This density shift is not yet fully understood. As shown in Eq. (5.1) the effect of ion rotation is included in the pressure balance formula. A constant rotation frequency of 10 kHz is assumed. This has been independently verified with the ICCD spectrometer and with the Mach probe. The centrifugal force of the ion rotation acts to push the plasma outwards. This is a real effect and it has been and will continue to be used in any pressure balance calculations presented in this thesis, but a plot of the plasma pressure with and without ion rotation is shown in Fig. 6.11 for completeness. The curve without ion rotation does show a wider profile and a higher pressure on the inner field lines like the Langmuir probe measures but the effect is small.

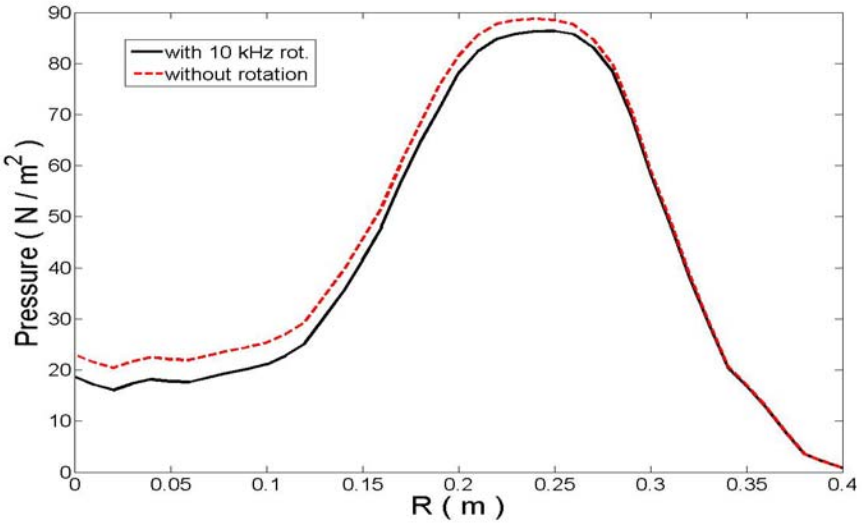

FIG. 6.11 The pressure profile is plotted with the effect of ion rotation and without.

All of the Langmuir results are gathered from the combination probe. Located near the Langmuir tips at the top of the combination probe are four more collection tips that are used for Mach probe measurements [20, 21]. Unfortunately the Mach probe tips were made too small to measure anything outside of the field null at the FRC midplane where the plasma density is highest. Accurate measurements of the rotational ion

velocity have been made with the Mach probe at the field null and are shown in Fig. 6.12. Similar to the results from ICCD spectrometer [22] the Mach probe reveals that the ions spin up to their nearly constant azimuthal velocity extremely quickly. These results show the ions are spinning and that their centrifugal effects should be included in any pressure balance analysis.

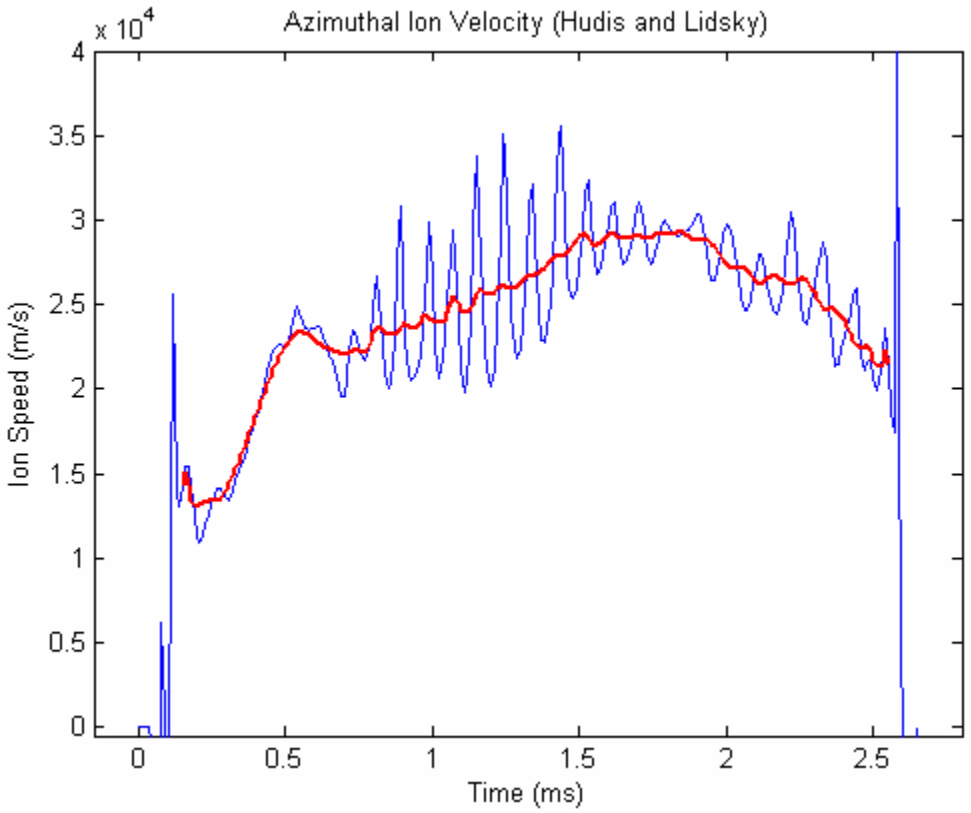

FIG. 6.12 Mach probe measurement of the azimuthal ion velocity at the FRC field null. The blue is the result of a 20 kHz lowpass filter applied to the raw data and the red trace is a boxcar average of the blue trace.

The possibility of an ion temperature gradient was proposed by Kiyong Lee in his Ph.D. thesis [19]. He argued that the ions were being heated on the outer field lines and that they were possibly hotter than the electrons at the field null but that they cooled to

about half the electron temperature on the inner field lines. If T_i on the inner field lines is lower than T_e, to satisfy pressure balance the density must be greater since $p(r) = n(r)k_B(T_e+T_i)$ and the pressure doesn't change because it is set by the opposing magnetic pressure. The RMF frequency is always set such that $\omega_{ci} << \omega_{rmf} << \omega_{ce}$, where ω_{ci} and ω_{ce} are the ion and electron cyclotron frequencies, because it is designed to act on the electrons. Although the RMF does not directly affect the ions, it can have a large effect on the axial field through a tearing and reconnection process at the FRC edge [23]. It is possible that this turbulent process on the outer field lines is heating the ions more than the electrons.

The temperature equilibration time, τ_{ei}, is a measure of how long it take for the ions and electrons to reach the same temperature due to Coulomb collisions. This equation is written as follows:

$$\tau_{ei} = \frac{3\pi\sqrt{2\pi}\varepsilon_0^2 M_i T_e^{3/2}}{n_e Z^2 e^4 \sqrt{m_e}\ln\Lambda} \tag{6.1}$$

This is a measure of the maximum time of temperature equilibration since it is based on the assumption that $T_i \approx 0$. This assumption allows the following.

$$\tau_{ei} = T_e \Big/ \frac{dT_i}{dt} \tag{6.2}$$

In the case where $T_i \neq 0$ it has been shown by Spitzer that Eq. (6.3) holds and that the equilibration time is lower since for a finite T_i some collisions will result in an energy transfer from the ions to electrons instead of the one sided energy transfer from the electrons to the ions.

$$\tau_{ei} = (T_e - T_i) \Big/ \frac{dT_i}{dt} \tag{6.3}$$

Eq. (6.1) is calculated from the Langmuir measurements at the field null and is plotted in Fig. 6.13. The average temperature equilibration time of less than 500 μs would imply that a strong ion heating on the outer field lines is certainly a possibility.

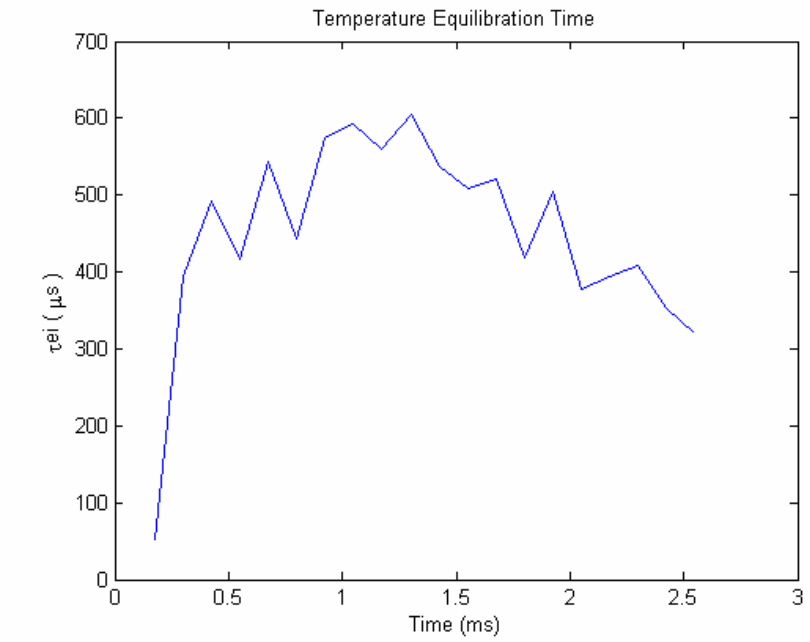

FIG. 6.13 The electron-ion temperature equilibration time calculated using the measurement from the Langmuir probe at the FRC field null.

6.2.2 Results from the North Exhaust Jet (Even-Parity FRC)

The combination probe was placed in the north exhaust jet of the FRC approximately z = 1.2 meters from the midplane. It will be shown that the density was in the low 10^{18} /m^3 range but the Langmuir probe was capable of making accurate measurements. The Mach probe is not capable of measurements at this level so the exact flow speed could not be measured. For this analysis the flow speed in the jet is assumed to be the acoustic speed and a pressure balance is used to calculate the ion temperature in the jet.

As was the case with the radial scan at the midplane the same procedure was followed in collecting data in the exhaust jet. Only data collected on a shot where a virtual match in the measurements of our key diagnostics was accepted. In Fig. 6.14 the electron temperature measured at the center axis of the north exhaust jet is plotted along with the electron temperature measured at the FRC midplane. As expected the value of T_e in the exhaust is virtually the same as it is at the midplane. The length of the FRC is approximately 1.5 meters and extends from z = -0.75 meters south to z = +0.75 meters into the north side of TCSU [24]. This has been measured with the translatable 3-axis B probe. The jet at z = 1.2 m is fully formed but the TCSU vacuum chamber remains 80 cm in diameter at this location. The internal flux conserving rings are still in place in the jets also. In terms of the TCSU machine the only differences between the jet and the midplane is that the chamber wall is stainless steel in the jet because the total length of the quartz TCSU confinement section is 1.25 meters. The RMF antennas are also 1.25 meters long. Since there are no plasma strike points between the FRC and z = 1.2 m in the exhaust jet there is nothing for the mobile electrons to lose energy to other than unfavorable collisions.

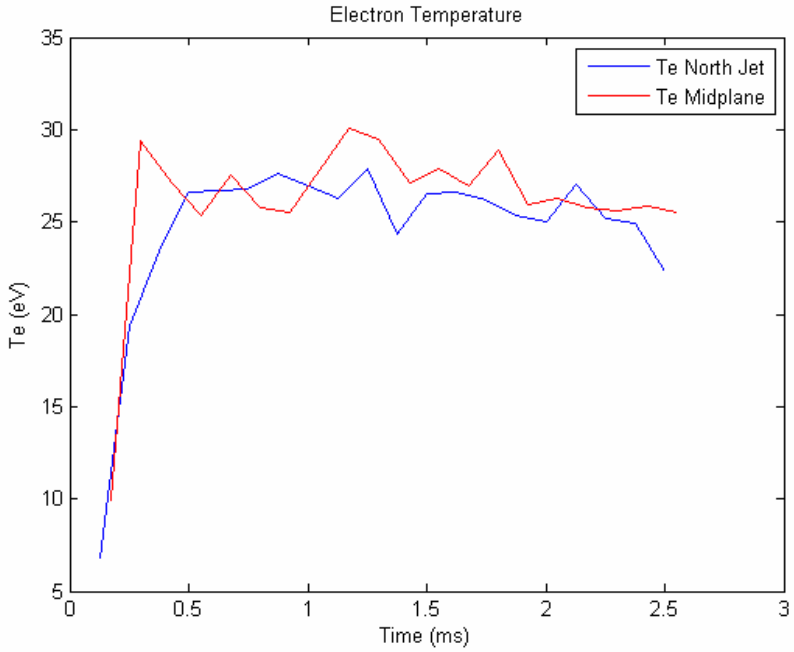

FIG 6.14 The electron temperature measured with the Langmuir probe at the center axis in the north exhaust jet, z = +1.2 m (blue) and the electron temperature at the FRC midplane (red) are plotted together.

A radial scan of measurements was performed in the exhaust. As noted the electron temperature measurements are difficult when the density falls to the 1-2x10^{18} /m^3 range. A 3D surface plot of the electron temperature is shown in Fig. 6.15. Although the data becomes somewhat uncertain at larger radii in the jet it is apparent that the electron temperature profile is flat.

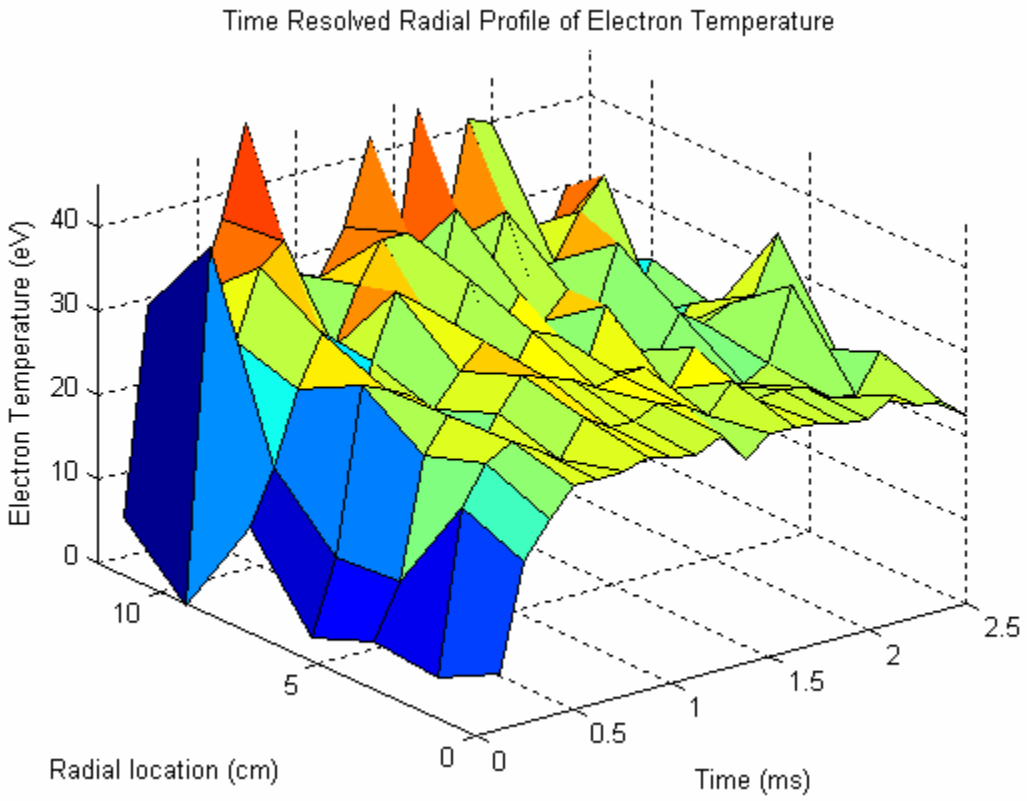

FIG. 6.15 3D surface plot of the electron temperature at z = 1.2 m for the 122 kHz even-parity RMF formed FRC.

The density measurements in the jet are of particular importance. Although one would have reasoned T_e to be approximately the same as it is at the midplane it is not a common measurement and no record of Langmuir measurements in the exhaust jet of an RMF formed FRC have been found. First the density at the center axis of the jet is plotted in Fig. 6.16. The density in the jet is about 5 times smaller than it is at the FRC field null in the midplane except at the very beginning. Other than for the first half millisecond the density appears to follow the time history of the process in the FRC. The jet density is lowest during the quiescent phase and then increases near RMF shut-off and the end of the plasma. This increase in density could signal the onset of an instability

which causes the FRC to shed off more particles, but it is also seen from the time sensitive plots earlier in the chapter that the electron density is increasing in the midplane with time. This is possibly due to the FRC being awash in a sea of neutral particles which are continuously swept in by the RMF. The puff valves are open for much the FRC lifetime and the measurements with the fast ion gauge and calculations of the particle flow rate out of the puff valves shown in Chapter 2 confirm that the neutral pressure is high.

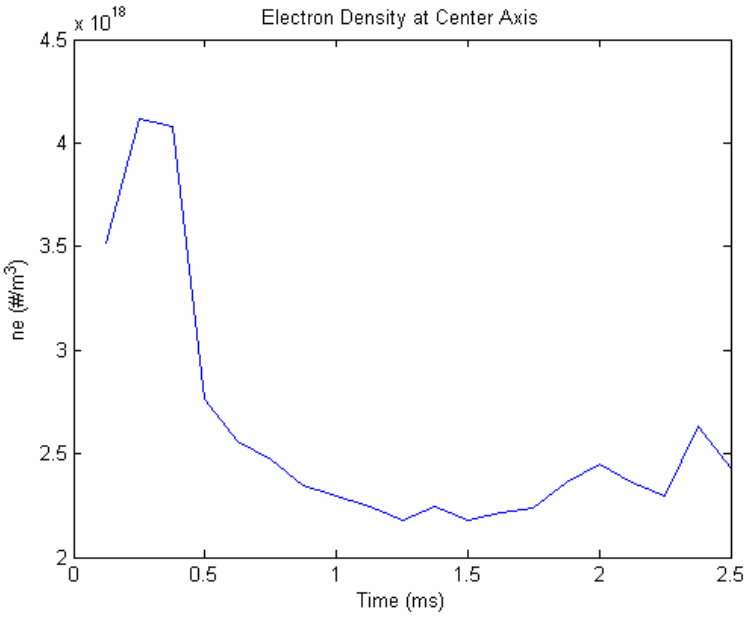

FIG. 6.16 The electron density measured as a function of time at R = 0 m and z = 1.2 m.

A radial scan to measure the electron density was completed in the north exhaust jet and is shown as a 3D surface plot in Fig. 6.17. The structure of the FRC exhaust is clearly visible in this graph. The spike in density at the beginning is most likely due to an ionization wave that forms when the RMF first turns on. If we consider the formation process during RMF startup it's clear that it is chaotic and turbulent. A small stream of ionized particles is supplied by the plasma gun described in Chapter 3 approximately

2.63 meters from the midplane. The number of ionized particles is a small fraction of the total particle count supplied by the puff valves just before the RMF starts up. The RMF causes the ionization fraction to increase by well over an order of magnitude in microseconds. Many particles become ionized but are not caught by the formation of the FRC. As the magnetic field in the plasma reverses a lot of ionized gas in the fringe region is pushed out as the FRC violently expands to the size and shape it takes for as long as confinement holds. This ionized deuterium on the outskirts of the FRC during formation are recorded by the Langmuir probe and are seen as the large density spike near t = 0 ms.

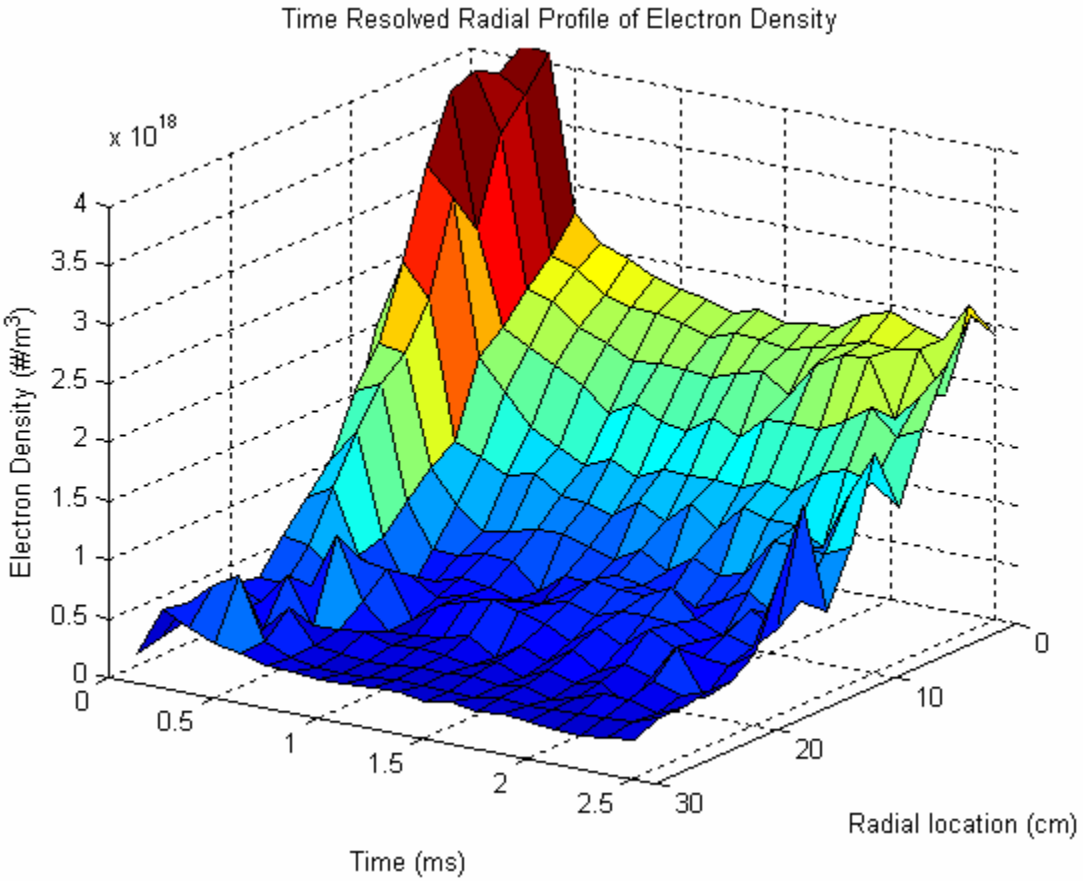

FIG. 6.17 3D surface plot of the electron density at z = 1.2 m for the 122 kHz even-parity RMF formed FRC.

The size of the exhaust jet is better determined in a plot of n_e versus radius. The radial profile of the electron density at t = 1.0 ms is supplied in Fig. 6.18. An assumed circular exhaust jet is formed soon after the FRC is formed and remains quite stable throughout. The density in the jet changes slightly and is somewhat proportional to the density of the FRC. As the magnetic field lines in the exhaust are comprised of the open field lines at the FRC midplane we can estimate the size of the scrape-off layer using the radius of the exhaust jet, r_{jet} = 15 cm. If the thickness of the scrape-off layer is Δr, we can calculate it from the separatrix radius and the area of the jet since $2\pi r_s \Delta r = \pi r_{jet}^2$. Using r_s = 35 cm we find Δr = 3.2 cm which is what we would expect because the internal flux conserving rings are at approximately r_c = 38 cm.

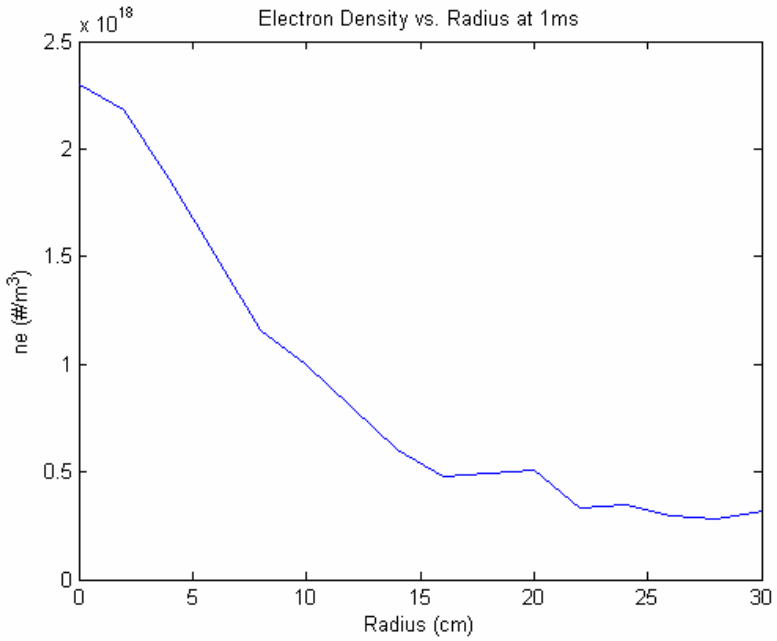

FIG. 6.18 Radial profile of the electron density in the north exhaust jet measured by the Langmuir probe at t = 1.0 ms.

The particle flow rate in the exhaust jet can now be calculated. The Mach probe part of the combination probe could not make accurate measurements in the exhaust jet because the density is far too low. A redesign of the Mach probe tips in the form of flat

paddle probes with a large collection area was completed but it was not built since the shutdown of TCSU was imminent. Based on studies in the FRC scrape off layer [25, 26] the flow speed in the jet is assumed to be acoustic speed given in Eq. (6.4).

$$c_s = \left[\frac{k_B (T_e + T_i)}{M_i} \right]^{\frac{1}{2}} \tag{6.4}$$

The particle flow rate is calculated from Eq. (6.5).

$$\dot{N} = c_s n_e(r) A_{jet} = 2\pi c_s \int r n_e(r) dr \tag{6.5}$$

The integral in Eq. (6.5) is easy to compute once the ion acoustic speed is known. We could simply assume $T_e = T_i$ although this may not be true in the jet since the massive ions with large cross section are likely to undergo more collisions in which they may lose energy. The ions can also lose energy through adiabatic expansion as they travel from the scrape-off layer into the larger exhaust jets. The well defined geometry of the jet invites a pressure balance analysis in an attempt to calculate the ion temperature. The pressure in the jet should balance with the axial magnetic pressure and azimuthal magnetic pressure if there is any transverse field in that location. The pressure balance formula is written in Eq. (6.6).

$$n_e k_B (T_e + T_i) + \frac{B_z^{\,2}}{2\mu_0} + \frac{B_\theta^{\,2}}{4\mu_0} = C \tag{6.6}$$

Fortunately an axial scan of the magnetic field with the 3-axis probe was completed for the 122 kHz even-parity FRC [27]. The scan was done in increments of 5 cm from z = -132 cm to z = +138 cm. The magnets in this section of TCSU fire 14 ms before time zero and are designed to provide a near steady axial field over the 2.5 ms

lifetime of the FRC. Data from the 3-axis probe exists at z = +118 cm, only 2 cm from location of the Langmuir probe measurements. A radial plot of the axial magnetic field for a plasma shot and a vacuum reference shot in which all magnetics, including the RMF, were fired but the plasma gun was not used and no gas was puffed in is shown in Fig. 6.19. A trace of the transverse magnetic field is also included.

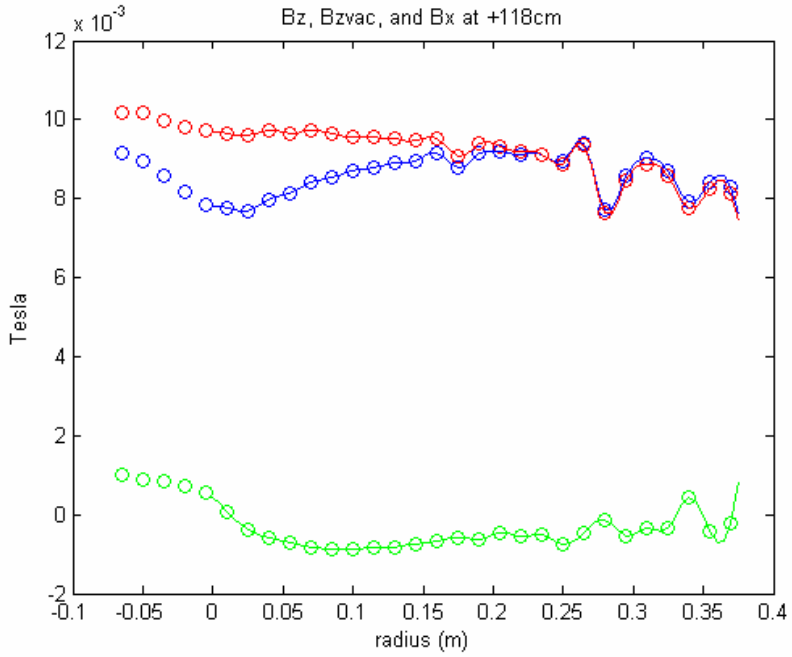

FIG. 6.19 Data from the 3-axis probe at z = +118 cm. The axial magnetic field for a vacuum reference shot (red), the axial magnetic field for plasma shot (blue), and transverse magnetic field for a plasma shot (green) are shown.

It is clear from Fig. 6.19 that the effects from B_θ are negligible in the exhaust jet so that term will be set to zero in Eq. (6.6). To compensate for probe effects the difference in the axial magnetic field for a vacuum shot and the plasma shot is calculated. If we call this difference ΔB, the integration constant in Eq. (6.6) can be solved and pressure balance can be written as follows.

$$n_e k_B (T_e + T_i) = \frac{B_{Z\max}{}^2 - (B_{Zvac} - \Delta B)^2}{2\mu_0} \tag{6.7}$$

In Eq. (6.7) the plasma pressure on the left side is equal to the magnetic pressure defined by the right side. In Fig. 6.20 the component of pressure due to the electrons only is plotted on the same graph as the magnetic pressure. Excellent agreement with the magnetic pressure is seen until about R = 12 cm where the calculated electron pressure breaks down because the design minimum of the Langmuir probe is reached at about n_e = 3x10^{17} /m^3.

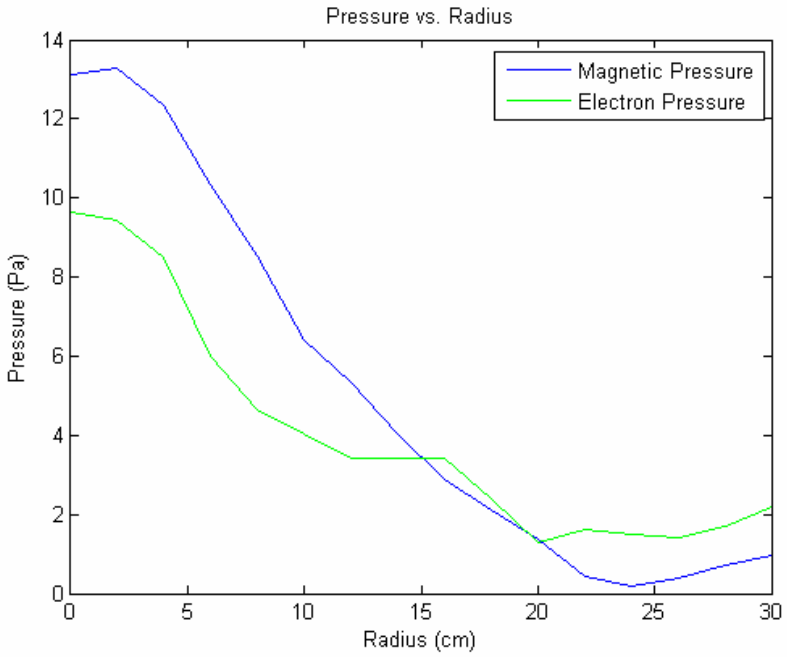

FIG. 6.20 The magnetic pressure and the electron component of the plasma pressure in the north exhaust jet.

At this point the calculation of T_i is straightforward. We can already see that the ion temperature is not going to be equal to the electron temperature. In fact it comes out to be approximately half of the measured electron temperature. Fig. 6.21 is plot of T_e and

T_i versus radius where the Langmuir measurements are still valid. Like the electron temperature the ion temperature is also flat in the FRC exhaust. The electrons retain much of their energy because the parallel conductivity of the electrons is very high. The ions likely lose energy through adiabatic expansion. The difference in temperature is also supported by the ion-electron temperature equipartition time in the exhaust jet which is approximately 2.7 ms, that is longer than the lifetime of the FRC.

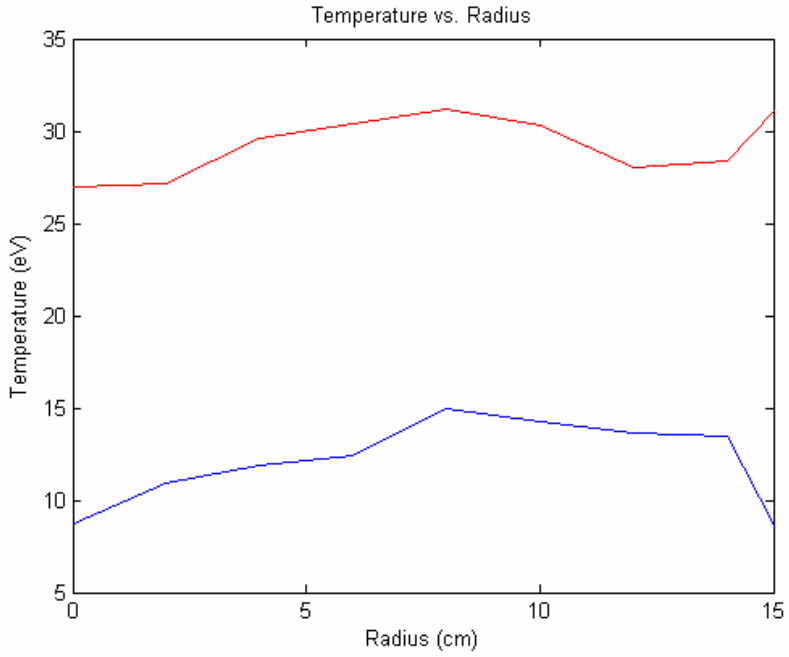

FIG. 6.21 The radial profile of the electron temperature (red) and the ion temperature (blue) at z = +1.2 meters.

With the temperatures shown in Fig. 6.21 the ion acoustic speed is determined to be approximately $c_s = 4.5\text{x}10^4$ m/s. The particle flow rate in the north exhaust jet is calculated from Eq. (6.5) and the results are shown in Fig. 6.22. The large peak is the ionization wave from the RMF startup discussed earlier. After that passes a steady rate of approximately $7\text{x}10^{21}$ /s is reached which gradually increases with time. The Langmuir

probe can only detect electrons so this calculation is likely not the full amount of particles escaping the north side of the FRC. Some of the particles will recombine before reaching the probe and this says nothing about charge exchange in the FRC. Although the charge exchange process in TCSU is more of a recycling issue and is likely providing much of the drag on the ions keeping them from spinning up to higher azimuthal velocities [28].

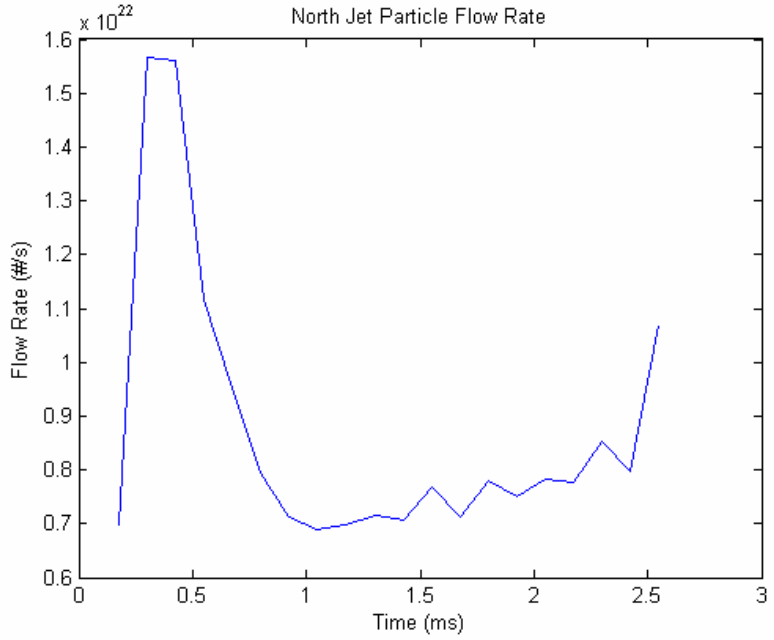

FIG. 6.22 The flow rate of ionized particles escaping the FRC in the north exhaust jet measured at z = 120 cm.

An estimate of the energy in the exhaust jet is made. We assume the total energy in the exhaust is comprised of thermal energy in the plasma, kinetic energy of the directed flow, and the ionization energy of deuterium (13.6 eV). The equation for energy in the FRC exhaust jet is as follows.

$$E_{jet} = \frac{3}{2} k_B T_t + \frac{1}{2} M_i c_s^{\,2} + (13.6eV) \tag{6.8}$$

The power of this flow is the product of Eq. (6.8) with the particle flow rate.

$$P = \dot{N} \times E_{jet} \tag{6.9}$$

Eq. (6.9) has been calculated and the result is shown in Fig. 6.23. This is considered to be the power lost due to convection in the north exhaust jet only from the FRC. Therefore the total convective power lost is the sum of the Eq. (6.9) calculated for the north jet and south jet.

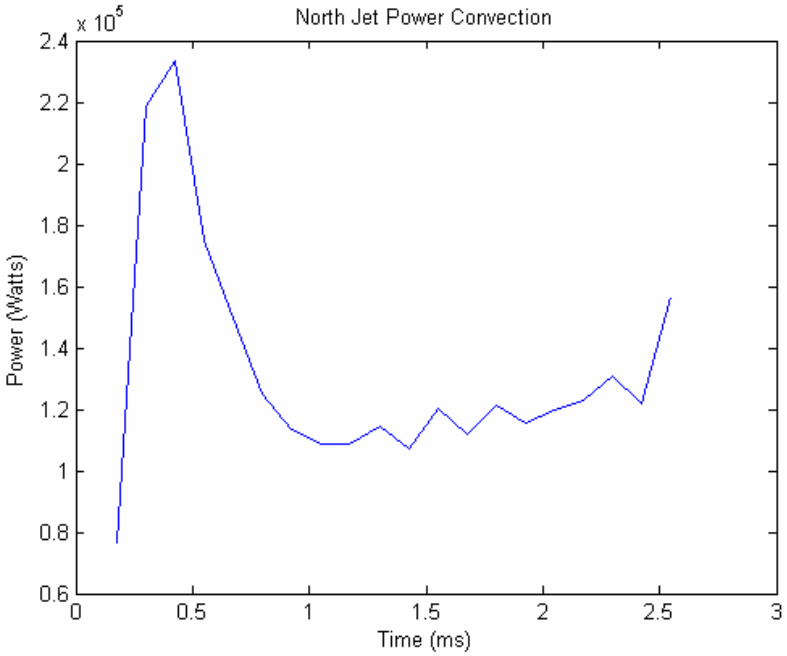

FIG. 6.23 The calculated power lost due to convection of the 122 kHz even-parity FRC out of the north exhaust jet.

6.2.3 Results from the South Exhaust Jet (Even-Parity FRC)

The analysis for the south jet is the same as it is for the north jet so only a brief overview will be given here. Langmuir probe measurements made in the south exhaust jet are at z = -120 cm equidistant to the FRC midplane as the measurements made in the north jet. It will be shown that the results in the south exhaust jet are similar to the results from the north jet but not identical. The TCSU vacuum chamber is not symmetric about the midplane. There is only one plasma gun and it is mounted to the north end flange. It is also possible that the end shorting in the north end is not identical to the end shorting in the south end because of the vacuum chamber asymmetry although the magnetic conditions at both ends are the same.

The electron temperatures for all locations measured by the Langmuir probe in the 122 kHz even-parity FRC are shown in Fig. 6.24. As expected T_e is pretty much the same throughout TCSU. Any difference measured is not large enough to claim any sort of temperature imbalance.

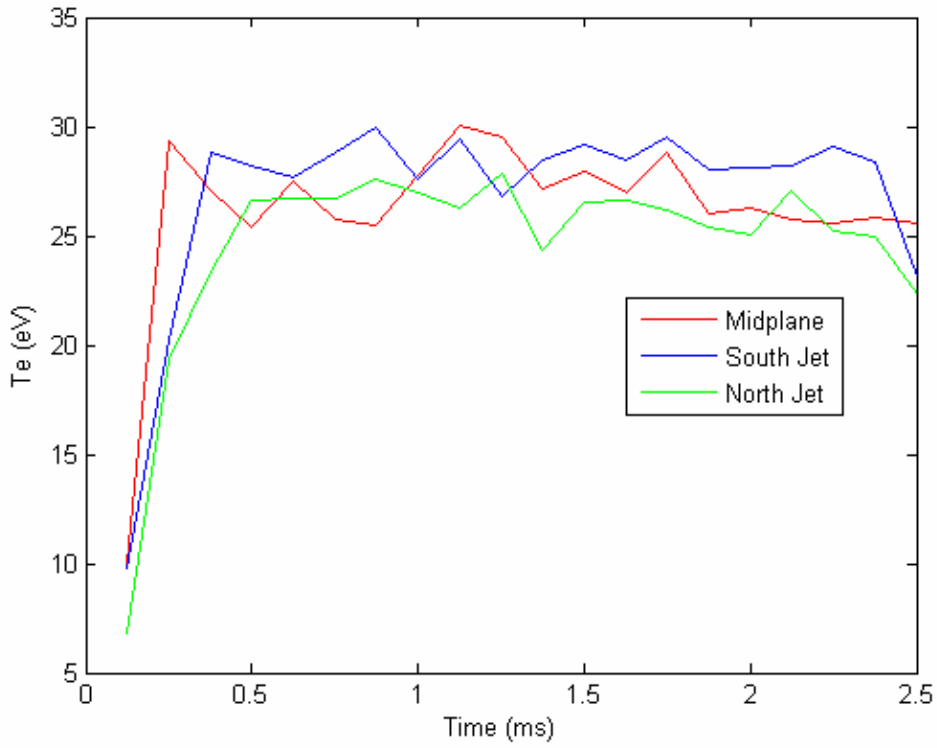

FIG. 6.24 The electron temperature measured at the FRC midplane (red), the south exhaust jet (blue), and the north exhaust jet (green).

The electron density measured at the south exhaust jet is noticeably lower than it is in the north jet. Multiple measurements were taken and the density results were repeatable. If the electron temperature in known the only term affecting the density is the ion saturation current collected by the probe. The ion saturation current is the maximum current that can be collected by a double Langmuir probe if the tips are the same size. A steady potential of 80 volts or more can be applied to the probe tips to ensure only the ion saturation current is collected. Probe scans were done in both the north and south exhaust jets using a steady 80 V potential across the tips and the ion saturation current measured in the north jet is always higher than it is south jet for a similar FRC. The maximum electron density measured in each exhaust jet is at the center axis. They are plotted on the same graph in Fig. 6.25.

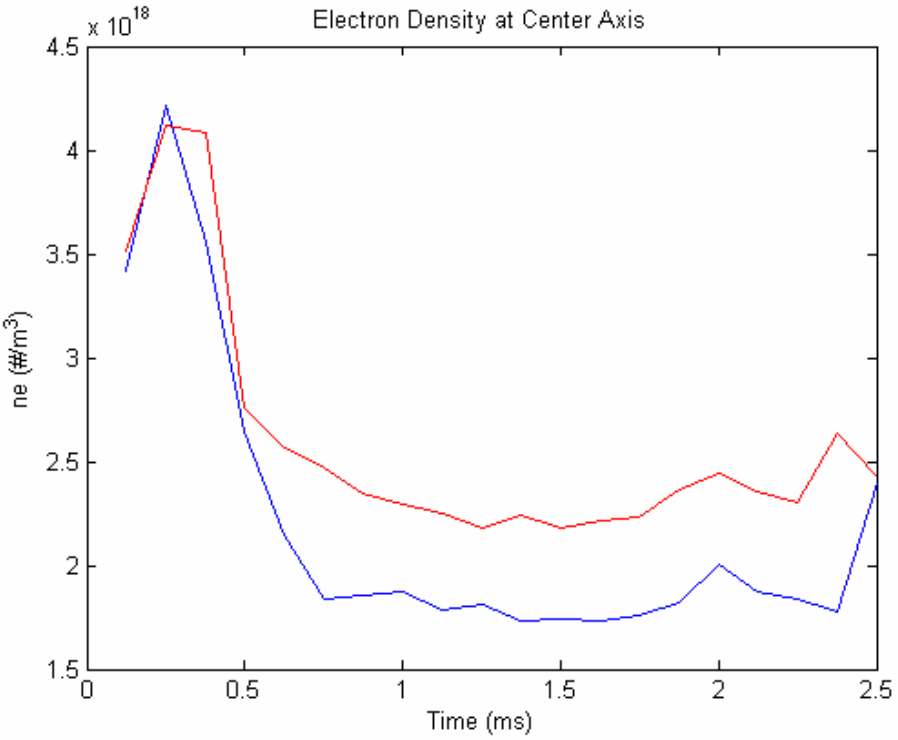

FIG. 6.25 The electron density measured at the center axis in the north exhaust jet (red) and the south exhaust jet (blue).

The radial profile of the south exhaust jet has the same shape as the profile measured in the north jet but the magnitude is lower. The 3D surface plot of the electron density for the south exhaust jet is shown in Fig. 6.26.

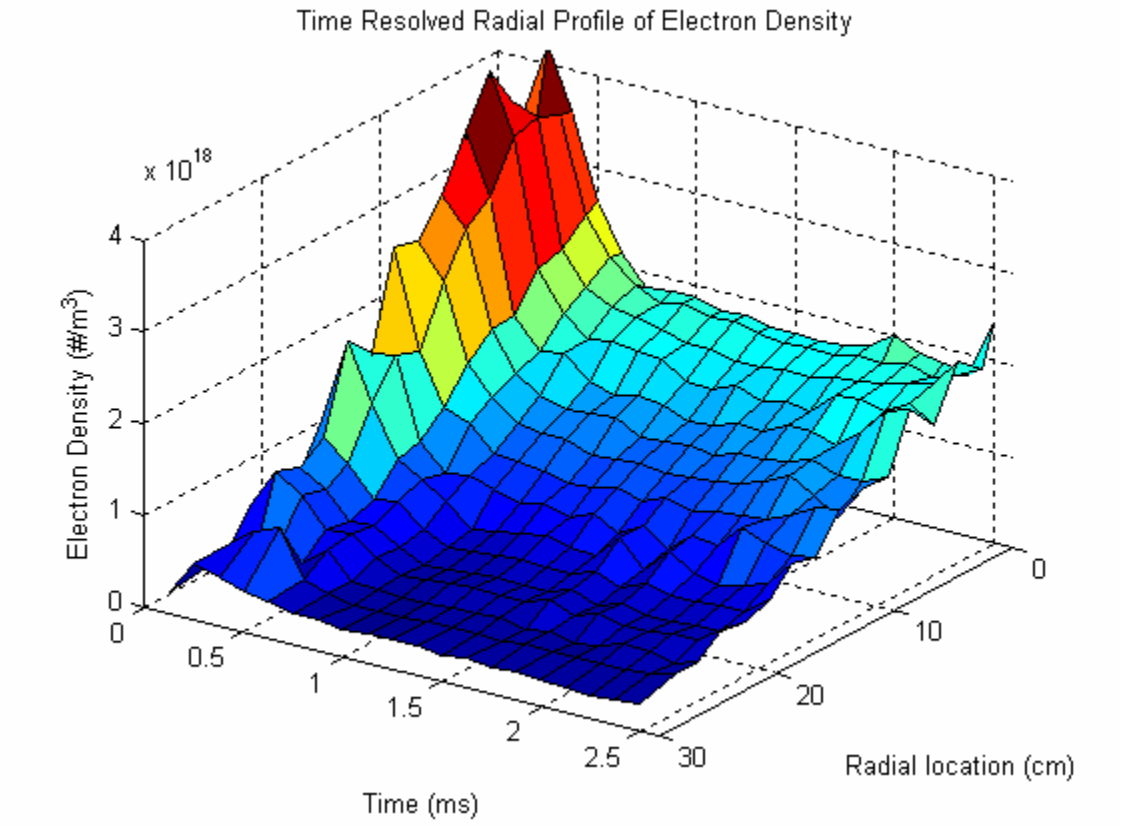

FIG. 6.26 3D surface plot of the electron density in the south exhaust jet at z = -1.2 m for the 122 kHz even-parity RMF formed FRC.

The ion temperature in south jet is calculated from pressure balance the same as it was done for the north jet. Unfortunately 3-axis magnetic probe data for a vacuum reference shot does not exist for any location within 18 cm of the Langmuir probe measurements at z = -120 cm. The magnetic coils of interest in both the north and south exhaust locations are the CE 'confinement-end' and CC 'confinement-cone' sections. Both sets of magnets are wired in parallel with equal lengths of the same type of cable. There was no reason to take data from vacuum reference shots at locations equidistant to the midplane in the end sections because the data is identical. But the jet plasma in the end section is not identical. The density of the south jet is lower than it is in north so the flux of the south jet should be lower also. This is apparent in the 3-axis magnetic probe

data taken in the south jet. The magnitude of the axial magnetic field in the south jet is lower than it is in north jet due to flux conservation. B_z for a plasma shot at z = -118 cm is plotted with the data seen in Fig. 6.19, without B_x.

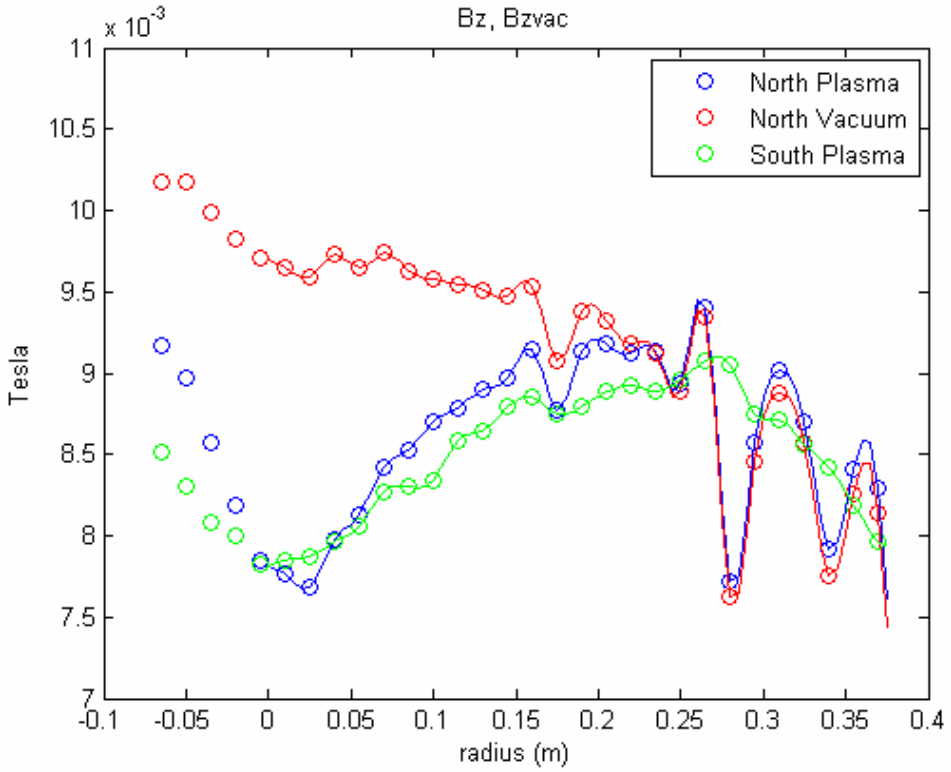

FIG. 6.27 The axial magnetic field of the 122 kHz even-parity FRC measured in both exhaust jets approximately 118 cm from the FRC midplane.

The magnetic pressure calculated from the right hand side of the Eq. (6.7) is lower in the south jet. The electron component of the plasma pressure is also lower in the south jet because the density is smaller. The final result is that the ion temperature calculated in the south jet also turns out to be approximately half of the electron temperature.

Due to the slightly higher measured electron temperature in the south jet the calculated acoustic speed comes out to be fractionally higher than the speed in the north

jet. The higher speed compensates for the lower measured density and the result is a particle flow rate in the south jet that is comparable with the flow rate in the north jet. The calculated particle flow rate for each jet is plotted in Fig. 6.28

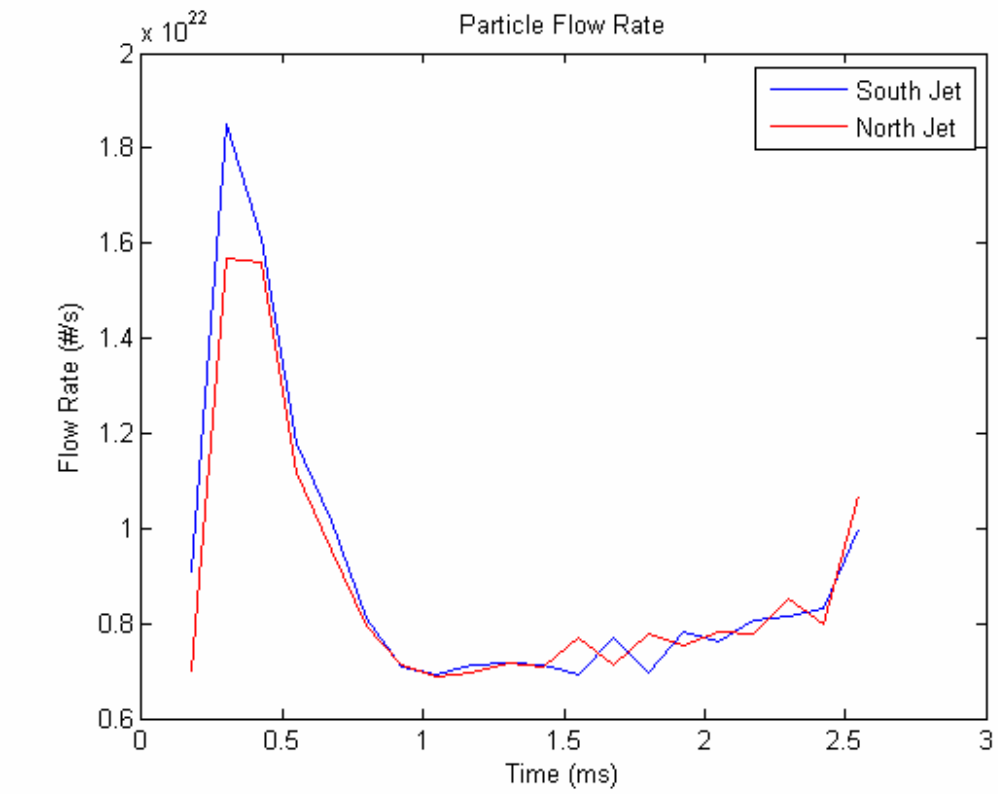

FIG. 6.28 The particle flow rate in the exhaust jets of a 122 kHz even-parity RMF formed FRC.

The power in the south exhaust is calculated from Eq. (6.9). The sum of the power in the south jet with the power in the north jet is considered to be the FRC power lost due to convection. These quantities are shown in Fig. 6.29.

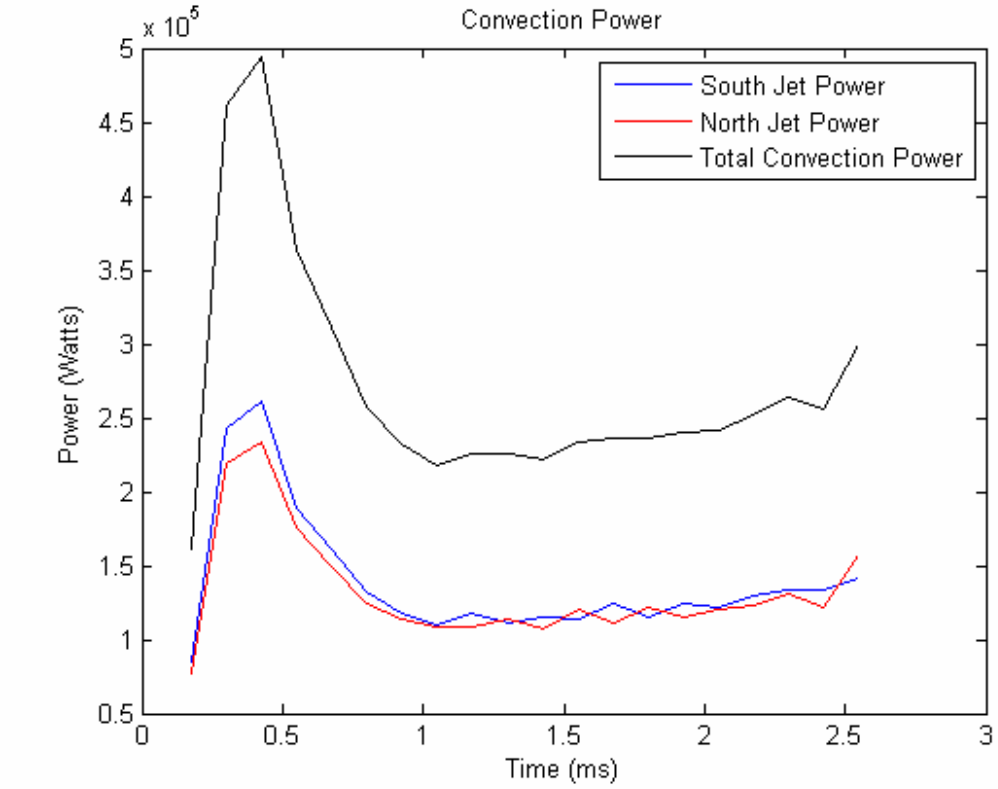

FIG. 6.29 The calculated FRC power loss due to convection is the sum of the power in each exhaust jet.

Although not an exact measure of the total power supplied to the FRC, the power in the RMF antennas is an acceptable estimate. The total measure of energy in an FRC is difficult without extensive 3D modeling. Radial compression, length contraction, and magnetic reconnection are but a few of the issues affecting the power of the FRC. To get an idea of how the calculated convection power loss scales with the total FRC power; prmf and the convection power are plotted together in Fig. 6.30. We see that approximately 25% of the FRC power lost is due to convection.

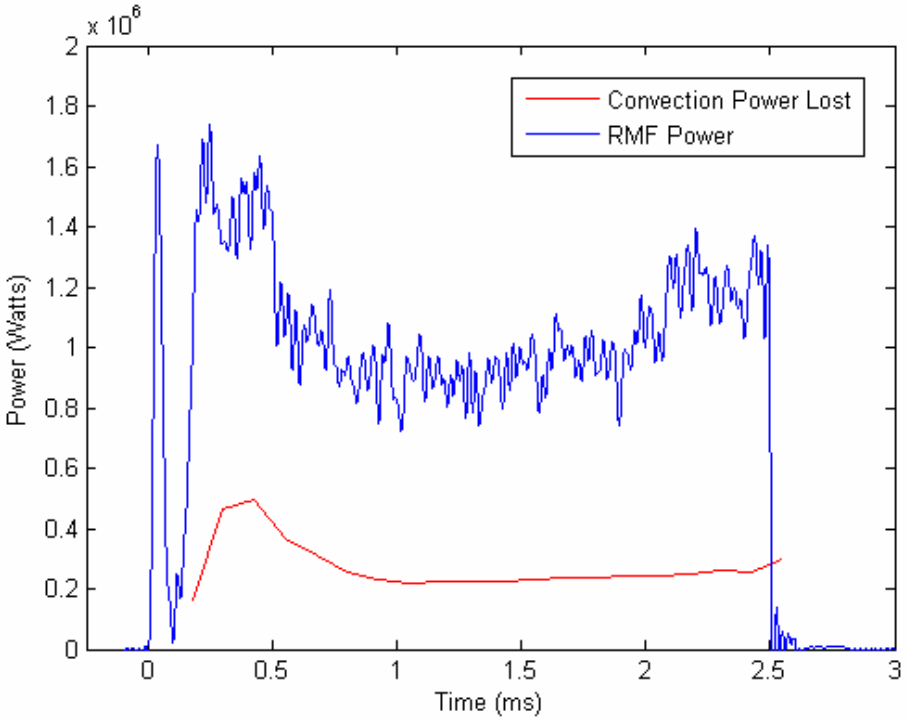

FIG. 6.30 The RMF power and the estimated power loss due to convection.

6.2.4 Additional Analysis of the 122 kHz Even-Parity FRC

The particle lifetime of the FRC is defined in Eq. (6.10).

$$\tau_n = \frac{N}{\dot{N}} \tag{6.10}$$

The total particle inventory, N, of the FRC can be calculated for the density profile shown in Fig. 6.7. The length of the FRC in this analysis is taken to be 1.4 meters based on the measurements of the x-point with the 3-axis probe. The calculated particle inventory is shown as a function of time in Fig. 6.31.

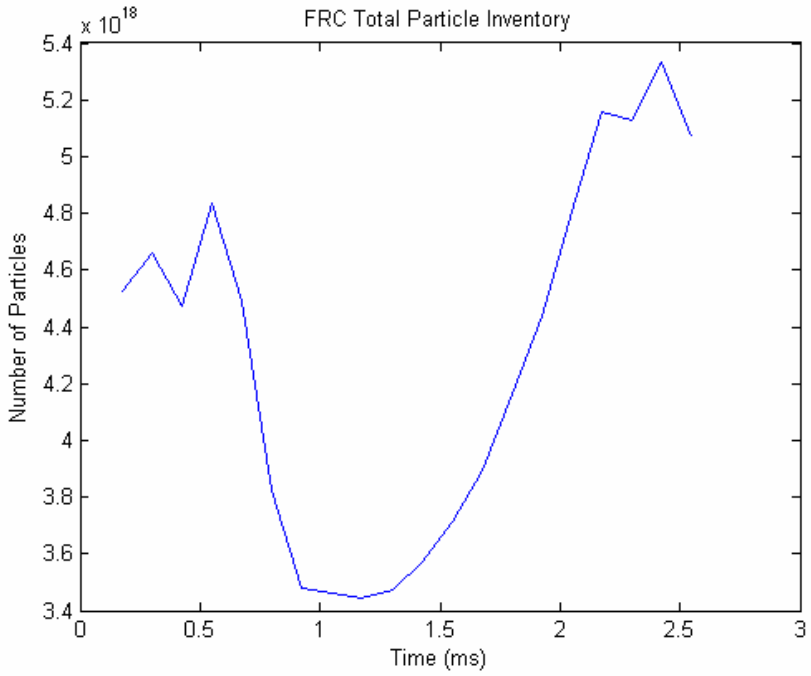

FIG. 6.31 The total number of particles in the 122 kHz even-parity FRC calculated from the density profile measured with the Langmuir probe.

The number of particles lost is the sum of the particle flow rates from each exhaust jet. The estimated particle lifetime has been calculated and shown in Fig. 6.32. As stated before the Langmuir probe can only detect charged particles. Hence any particle lost by the FRC that undergoes recombination or simply impacts the internal flux rings or the vacuum chamber wall will not be recorded. The actual particle lifetime is most likely shorter than the value shown.

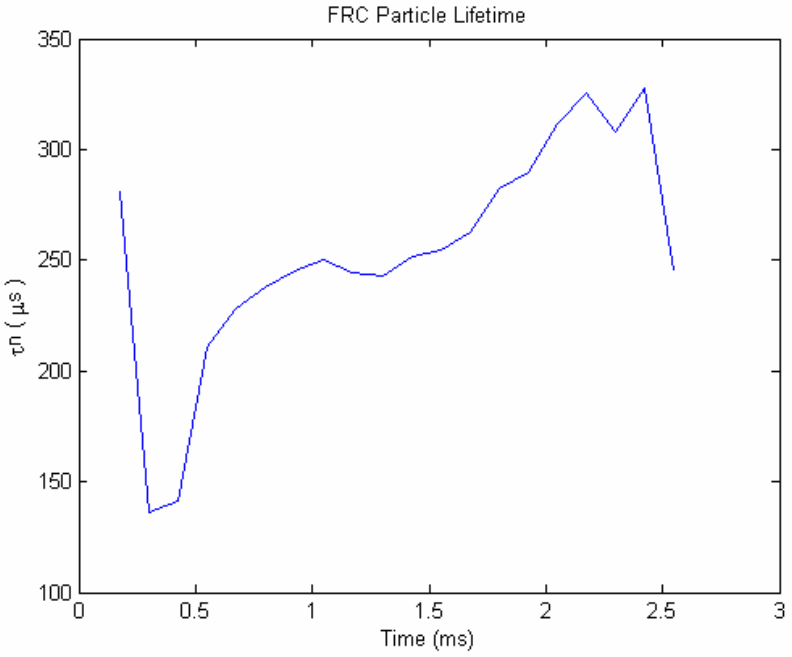

FIG. 6.32 The estimated particle lifetime of the even-parity FRC. This is the maximum possible particle lifetime of the FRC.

In steady state the particle loss rate is equal to the total ionization rate. The total ionization rate is the product of the average electron density, the average neutral density, and the ionization cross-section and is given in Eq. (6.11).

$$\langle S_{ion} \rangle = \langle n_e n_o \rangle \langle \sigma v \rangle_{ion} \tag{6.11}$$

The average electron density is the area integral from the center axis to the separatrix.

$$\langle n_e \rangle = \frac{2}{r_s^{\,2}} \int_0^{R_w} n_e(r) r dr \tag{6.12}$$

Once steady state is reached at t = 1 ms the average electron density is calculated to be approximately 5.45×10^{18} m^{-3}. The charge-exchange rate can also be calculated in a manner similar to the ionization rate as seen in Eq. (6.13):

$$\langle S_{cx} \rangle = \langle n_i n_o \rangle \langle \sigma v \rangle_{cx} \tag{6.13}$$

The ionization impact parameter has been calculated for hydrogen from the Atomic Data and Nuclear Data Tables [29] and is plotted versus temperature in Fig. 6.33. The charge-exchange cross section has also been calculated assuming cold (1 eV) neutral reactants.

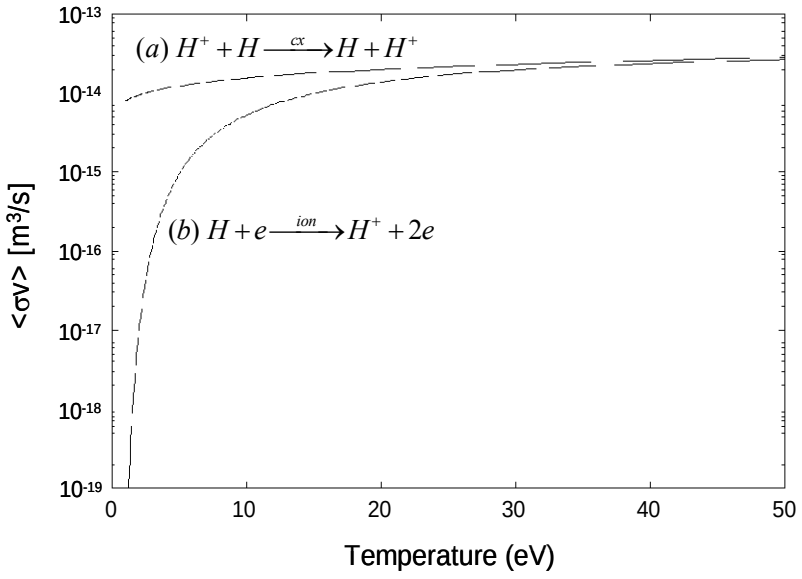

FIG. 6.33 The impact cross-section for charge-exchange (a) and ionization (b).

The average neutral density can now be calculated from Eq. (6.11). Although this analysis only applies to the FRC while it is in steady state, for completeness the neutral density has been calculated for the full duration. Once the FRC has reached steady state at approximately t = 1 ms the average neutral density is roughly 1.61×10^{17} m^{-3} or about 3% of the plasma density.

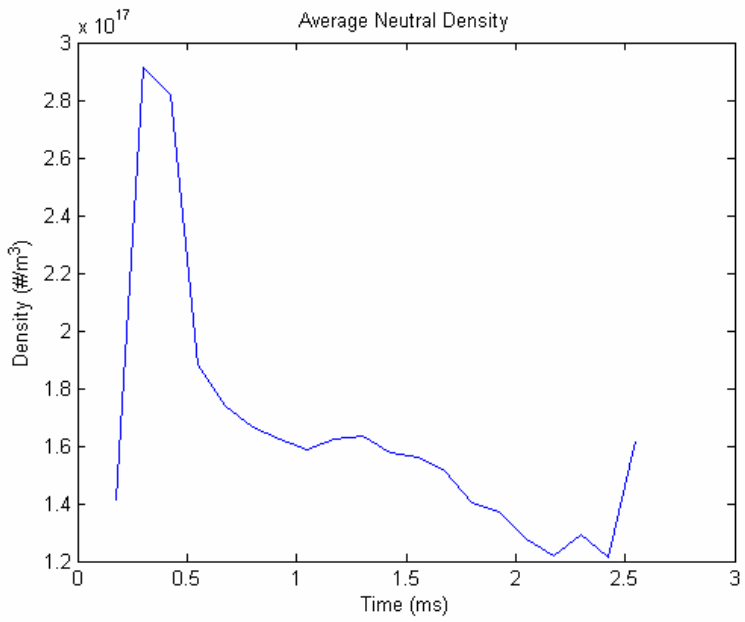

FIG. 6.34 The average neutral density calculated from the total ionization rate for the 122 kHz even-parity FRC.

The large initial ionization burst from the RMF start up appears in Fig. 6.34 and is only an artifact since the calculation assumptions are not valid in this region. The steady state regime is marked by a constant neutral density and the average neutral fraction during this time holds at approximately 0.03. As noted earlier, the increase in electron density from t = 1.7 ms to RMF shut off that is characteristic of the even-parity FRC causes the neutral density to fall. Technically our assumption that the particle loss rate is

equal to the ionization rate is only valid when the particle inventory is constant but we would expect the neutral density to fall when the electron density increases.

Knowing the average neutral density we can calculate the ionization source rate and the charge-exchange rate. These rates can be used to estimate the FRC power lost due to ionization and charge-exchange as follows. The ionization power lost is simply the product of the source rate, the ionization energy of deuterium, and the FRC volume. This estimate does not account for ionization losses due to impurity ionization.

$$P_{ion} = (13.6eV)\langle S_{ion}\rangle V_{FRC} \tag{6.14}$$

Charge exchange is a resonant process where an electron of a cold neutral is transferred to a hot rotating ion. The energy of each species is largely retained after the collision but the hot ion now becomes a hot neutral that is no longer confined by the electromagnetic field. Therefore the FRC energy lost is the thermal energy of the hot ion and the rotational energy. The power lost due to charge exchange is given in Eq. (6.15).

$$P_{cx} = \left[\frac{3}{2}kT_i + \frac{1}{2}M_i v_\theta{}^2\right]\langle S_{cx}\rangle V_{FRC} \tag{6.15}$$

The power lost due to radiation can also be estimated by using the results of the pinhole bolometer. The bolometer is calibrated such that the signal written to the database (prdl) is a line integrated measure of the total radiation. If we define the total radiated power emitted from the FRC per unit volume as P', then the bolometer signal and P' are related by the separatrix radius as written in Eq. (6.16).

$$prdl = P' \cdot 2r_s \tag{6.16}$$

If we assume the total radiation emanating from the FRC is uniform across the surface then the FRC power loss from radiation can be calculated from Eq. (6.17).

$$P_{rad} = P^{'} \cdot V_{FRC} = \frac{prdl}{2r_s} V_{FRC} \tag{6.17}$$

These power loss mechanisms are all plotted in Fig. 6.35 along with the RMF power input and the convective power loss calculated in Section 6.2.3. Of all the loss channels considered, Convection appears to be the dominant loss accounting for half of the total power lost. Charge exchange is also a considerable loss mechanism accounting for approximately 30% of the power lost. Unfortunately the biggest loss channel is not considered above and is likely due to the effect of the RMF itself. Numerical simulations suggest that the RMF is responsible for creating open field lines at the FRC boundary [30]. It is probable that these field lines intersect the wall and electron conduction along these open field lines is likely responsible for the majority of the total FRC power lost. Electron conduction out of the ends of the FRC is another possible energy loss mechanism that likely accounts for a small percentage of power lost in TCSU plasmas but could be more important for higher temperature FRCs.

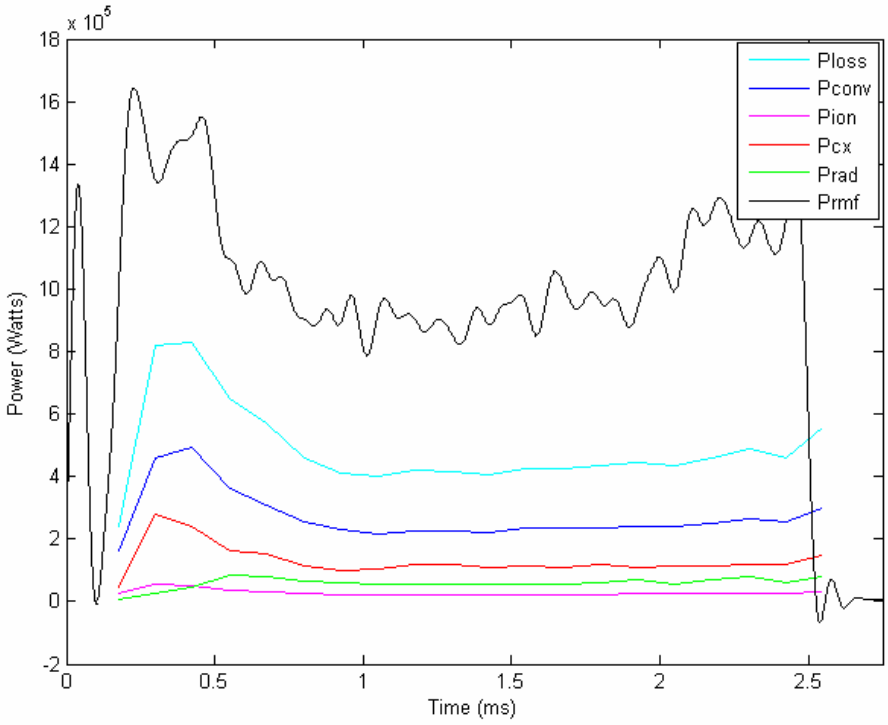

FIG. 6.35 The black trace is the RMF power (Prmf). (Ploss) is the sum of the estimated loss channels: the convective power loss (Pconv), Charge exchange power loss (Pcx), radiation power loss (Prad), and the ionization power loss (Pion).

To check the validity of the inferred neutral density and charge exchange rate and by extension the particle loss rate upon which these values are calculated we can calculate the torque on the FRC due to the influx of neutrals and compare this with the RMF torque. The torque per unit length about the z-axis due to the RMF is given in Eq. (6.18).

$$T'_{RMF} = \int_0^{r_s} 2\pi r^2 F_\theta dr \tag{6.18}$$

Where the azimuthal force on the electrons due to the RMF is $F_\theta = \langle J_{ez} B_r \rangle$. The brackets a time average over one RMF cycle. A solution for the torque in terms of the

magnetic field and known plasma parameters was first obtained by Hugrass [31] and later modified by Hoffman [32] for the rigid rotor assumption of a fixed rotational speed throughout the plasma column. The final expression for the RMF torque due to antennas of length L_a is given in Eq. (6.19).

$$T_{RMF} = \frac{2\pi r_s^2 B_\omega^2}{\mu_0} L_a f(\zeta) \tag{6.19}$$

The final term in Eq. (6.19) is an expression for ζ which is the ratio of actual FRC line current to the line current that would occur with synchronous electron rotation. This expression is related to the effective RMF penetration depth and $f(\zeta) = 0.1$ will be used in this analysis [33].

The charge exchange rate can be used to calculate a neutral drag torque. In calculating the charge exchange rate S_{cx} we assumed that the incoming neutrals are cold and non-rotating, and that the charge exchange neutral is immediately lost along with all of its angular momentum. The drag torque due to charge exchange is the integral of the angular momentum loss rate and is given in Eq. (6.20).

$$T_{cx} = 2\pi L_{FRC} \int_0^{r_w} S_{cx} M_i \omega_i r^2 dr \tag{6.20}$$

There is an additional momentum loss due to ion-neutral elastic collisions. In low temperature plasmas the torque due to ion-neutral collisions is approximately equal to the charge exchange torque. Therefore the total neutral drag torque plotted in Fig. 6.36 is double the charge exchange torque calculated in Eq. (6.20). The RMF torque is also plotted in Fig. 6.36 and we can see that the estimated neutral drag torque is more than half the value of T_{RMF}. It should be noted that the RMF torque calculated with Eq. (6.19) does not account for end-shorting. The actual RMF torque is most likely lower than the

value shown in Fig. 6.36, possibly by as much as 30%. Mach probe measurements have shown that the ions rotate in the same direction as the electrons due to their Coulomb attraction. The viscous drag on the ions inhibits spin-up which prevents further degradation of the plasma current.

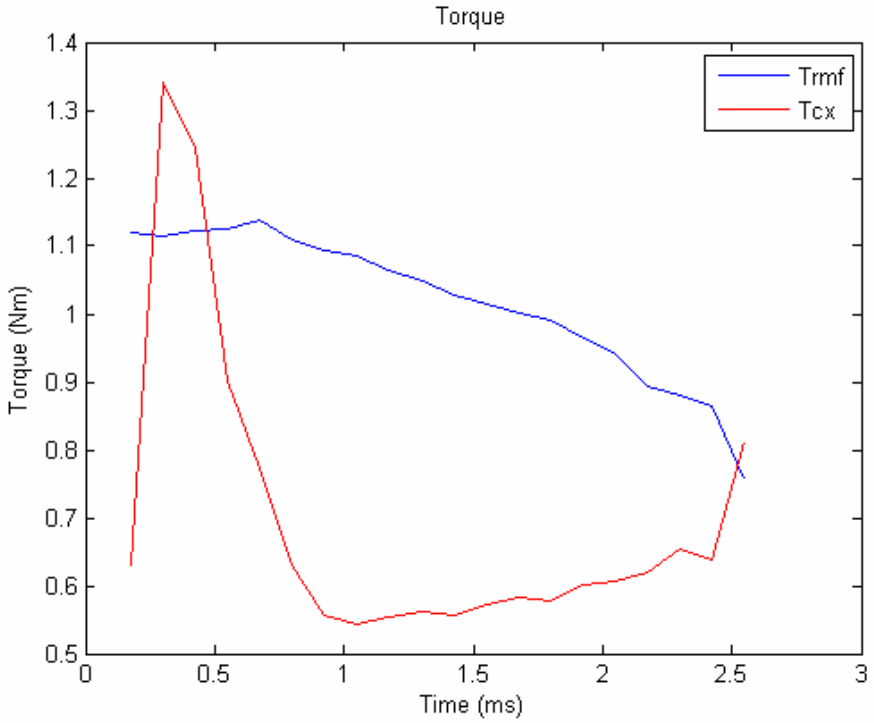

FIG. 6.36 The torque on the FRC due to the rotating magnetic field (Trmf) and the neutral drag torque due to charge exchange and ion-neutral collisions (Tcx).

6.3 Combination Probe Data for the 107 kHz Odd-Parity FRC

6.3.1 FRC Midplane Results

The time history of electron temperature and density at multiple radial locations has been measured for the 107 kHz odd-parity RMF formed FRC in the same manner that it was done for the even-parity FRC discussed earlier in the chapter. In terms of repeatability and stability the 107 kHz odd-parity FRC is the best operating mode in TCSU. The odd-parity FRC is capable of achieving a higher external magnetic field (B_e) for a given rotational magnetic field produced by the RMF antennas. The magnetic field due to the RMF antennas is B_ω and it is obtained from the measured RMF antenna current by $B_\omega(\text{mT}) = 0.5 I_{rmf}\,(\text{kA})$. The ratio of B_e/B_ω is constant for all modes of even and odd-parity RMF operation as is shown in a plot of the external magnetic as a function of B_ω given in Fig. 6.37. The external field scales linearly with RMF and a clear improvement is seen in RMF current drive for odd-parity RMF. $B_e/B_\omega = 5.8$ is achieved for the 107 kHz odd-parity FRC compared to $B_e/B_\omega = 4.0$ for the 122 kHz even-parity case.

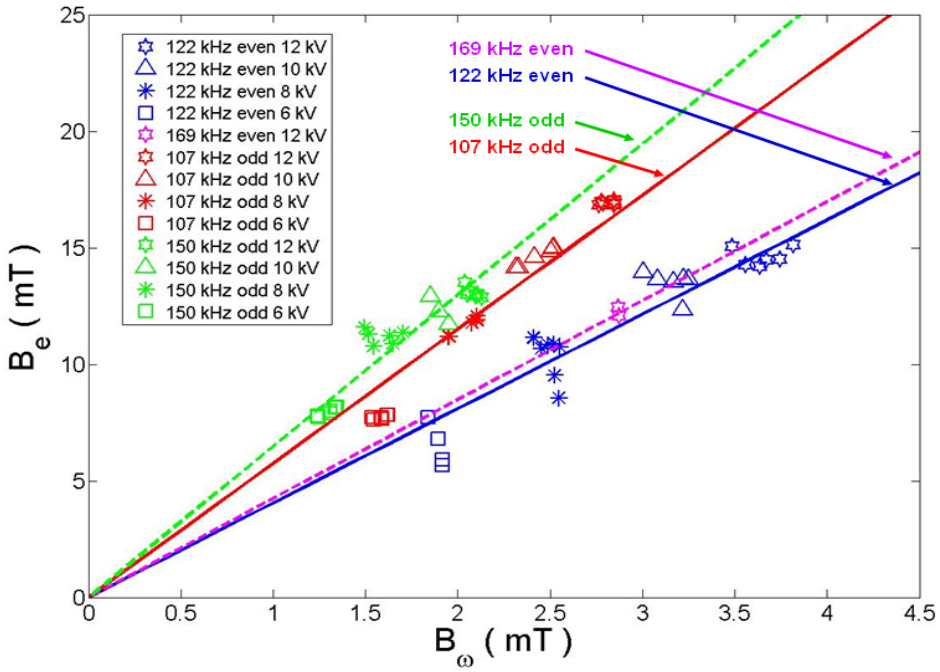

FIG. 6.37 The external magnetic field plotted as a function of B_ω for even and odd-parity RMF as the RMF voltage is increased from 6 kV to 12 kV.

A strong oscillating B_z is measured by the 2-axis magnetic probe near the seperatrix at the FRC midplane during odd-parity RMF operation. The center section of each RMF antenna cradle carries zero net current during even-parity operation because the current in each cradle is equal and in opposite directions, but during odd-parity RMF the current is in the same direction. This net current is responsible for the oscillating axial magnetic field seen near the plasma edge. The plasma confinement at the midplane appears to be affected by the oscillations in the axial magnetic field. This is isolated to the plasma edge at the midplane only during odd-parity operation. In the 3D surface plot of the electron density profile measured with the Langmuir probe shown in Fig. 6.38 a noticeable increase in density is seen at the FRC boundary indicative of particle loss due to the oscillating B_z at the midplane. Other than the Langmuir measurements taken in the FRC exhaust jets all measurements taken in the body of the FRC are done at the midplane

so it is difficult to estimate the axial length of the FRC influenced by the magnetic oscillations but based on measurements with the 2-axis magnetic probe at the midplane and the translatable 3-axis magnetic probe array the effect on the FRC is likely confined to a few centimeters in either direction of z = 0 cm.

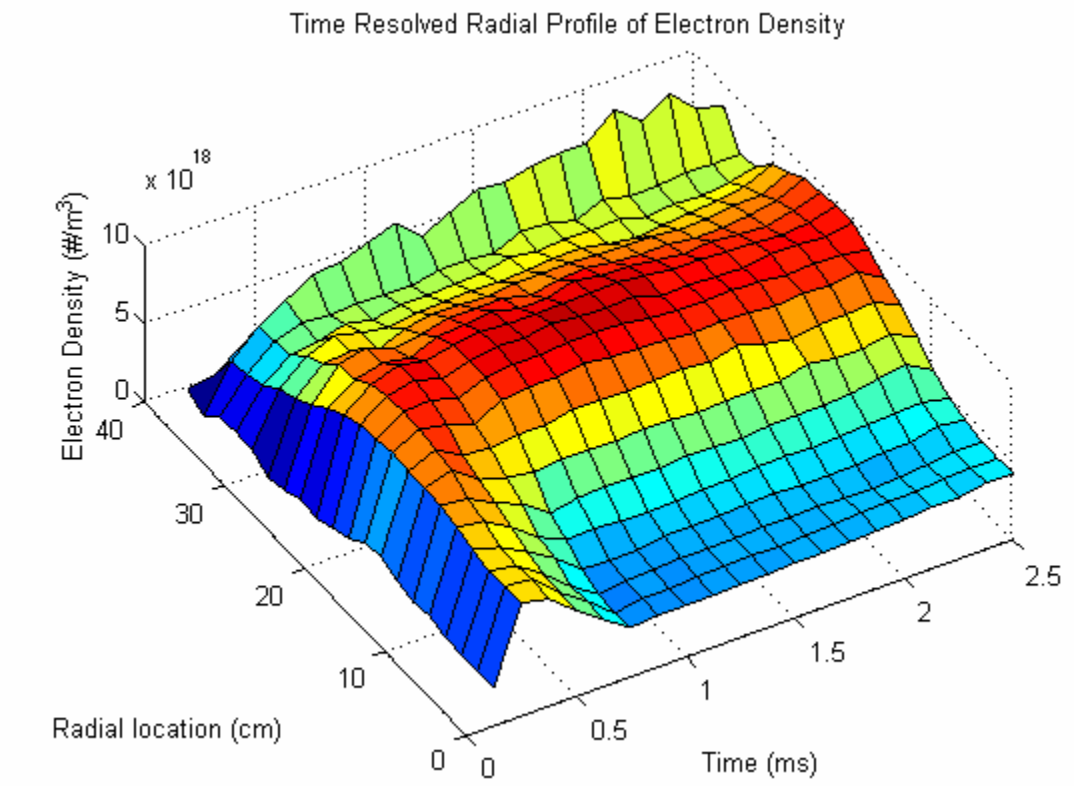

FIG. 6.38 3D surface plot of the electron density for the 107 kHz odd-parity RMF formed FRC.

A few noticeable differences exist in the electron density profile of the odd-parity FRC compared with the density profile of the even-parity FRC shown in Fig. 6.7. The

characteristic ionization burst observed in the odd-parity FRC is similar to the burst measured in the even parity FRC in both magnitude and duration. The maximum density measured at the field null is also similar for both cases but the odd-parity reaches the peak in density and sustains this throughout the FRC lifetime. The even-parity FRC was incapable of maintaining its maximum density when the axial magnetic field was driven near its maximum stable value of approximately 17 mT regardless of the amount of deuterium injected into the machine. The even-parity FRC could only maintain the peak operating density when the axial magnetic field was reduced to under 15 mT but this came at the expense of the electron temperature. The electron temperature measured with the Langmuir probe and the Thomson scattering diagnostic are in agreement for all FRCs formed in the TCSU machine and they show the temperature of the even-parity FRC to always be higher than it is for the odd-parity plasma. The average electron temperature of the 107 kHz odd-parity FRC was measured at approximately 23 eV. It is likely that the B_z oscillations are responsible for the lower T_e measurements in the odd-parity FRC by increasing the plasma contact with the wall. The oscillations are reduced at lower B_ω indicating improved confinement when B_ω/B_e is small. A surface plot of the electron temperature profile of the odd-parity FRC measured with the Langmuir probe is shown in Fig. 6.39. Langmuir measurements in the body of the odd-parity FRC show less fluctuations than they do for the even-parity FRC. This can also be said for other diagnostics on TCSU capable of resolving plasma turbulence like the internal magnetic probes and the bolometer, possibly due to the improved stability of the odd-parity FRC.

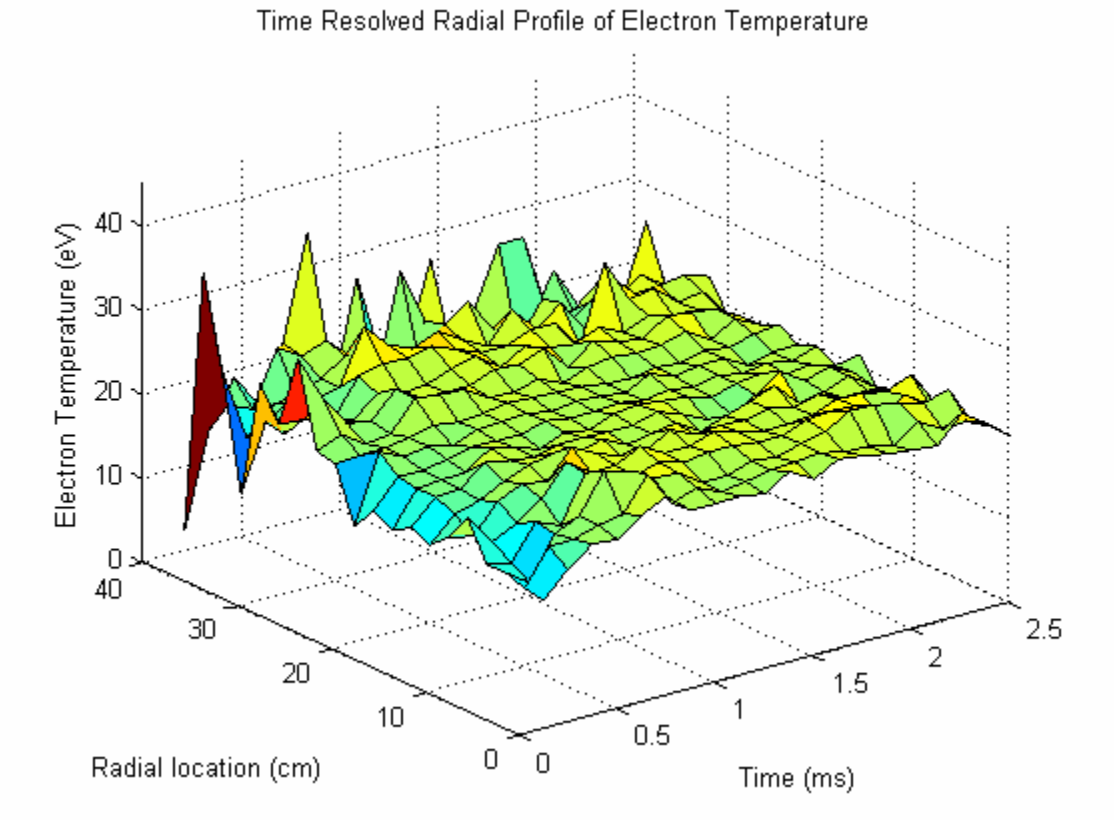

FIG 6.39 3D surface plot of the electron temperature for the 107 kHz odd-parity RMF formed FRC.

6.3.2 Results from the South Exhaust Jet (Odd-Parity FRC)

The electron temperature and density has been accurately measured with the Langmuir probe in the south exhaust jet (z = -120 cm) of the 107 kHz odd-parity RMF formed FRC. A 3D surface plot of the electron temperature in the exhaust jet is shown in Fig. 6.40. As expected the temperature profile is flat and equal to the measured temperature in the midplane.

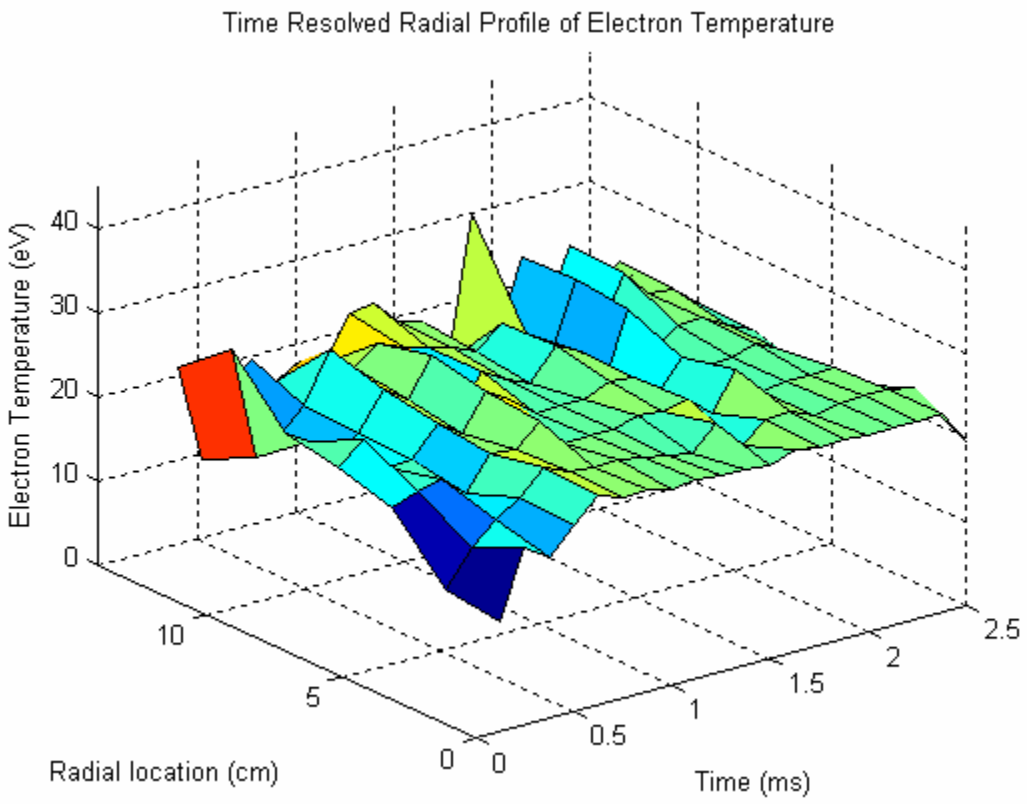

FIG 6.40 3D surface plot of the electron temperature at z = -120 cm for the 107 kHz odd-parity RMF formed FRC.

The electron density in the exhaust jet for the odd-parity FRC is similar to the measurement taken in the exhaust jets of the even-parity FRC. The characteristic

ionization burst is seen soon after RMF start-up and then density remains fairly constant at a value slightly greater than $2x10^{18}$ m^{-3}. The radial profile of the electron density decreases quickly until it drops below the range of the Langmuir probe at approximately R = 18 cm.

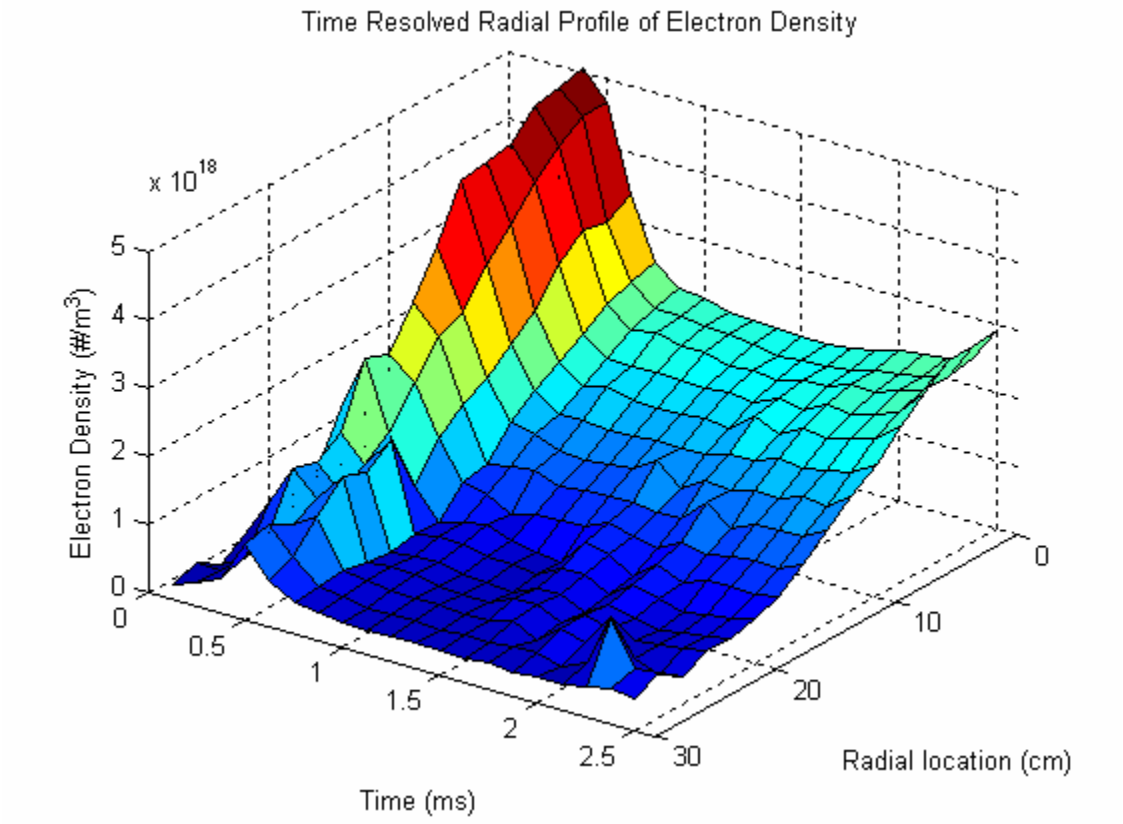

FIG 6.41 3D surface plot of the electron density at z = -120 cm for the 107 kHz odd-parity RMF formed FRC.

The FRC particle outflow to the south jet is calculated from Eq. (6.5). Once the particle flow rate is known the power in the exhaust jet can be calculated from Eq. (6.9). These two quantities are shown in Fig. 6.42.

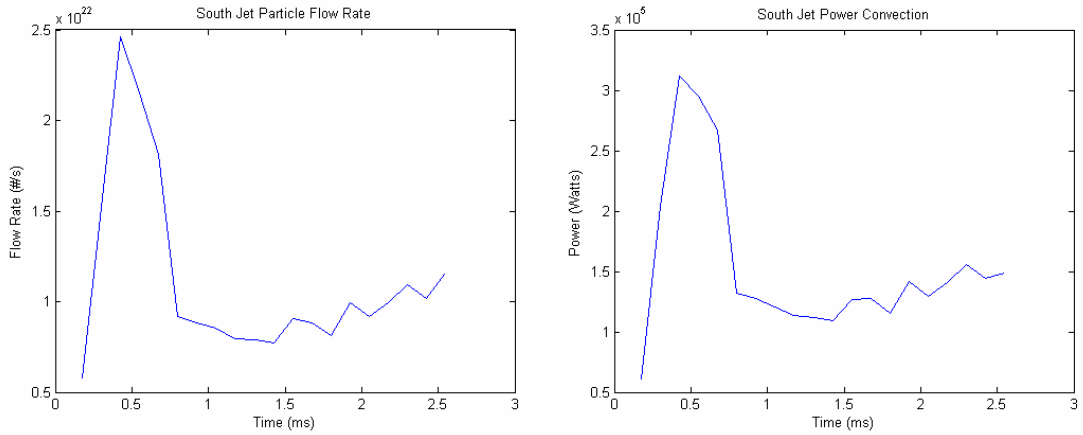

FIG. 6.42 The particle flow rate and power in the south exhaust jet of the 107 kHz odd-parity RMF formed FRC.

The 107 kHz odd-parity FRC will sustain its maximum electron density throughout the lifetime of the shot. Hence the total FRC particle inventory remains flat during the shot. The particle flow rate, however, gradually increases with time as seen in Fig. 6.42. The particle flow rate calculated for the 122 kHz even-parity FRC also showed a gradual increase with time but the FRC density at the midplane increases much faster from its steady state value at t = 1 ms to its maximum value around t = 2.2 ms. This caused the calculated particle lifetime of the even-parity FRC to increase slightly with time. The electron density of the 107 kHz odd-parity FRC does not change much with time which results in a particle lifetime that decreases with time. The total particle inventory calculated by integrating the electron density across the FRC volume and the particle lifetime τ_n of the odd-parity are shown in Fig. 6.43.

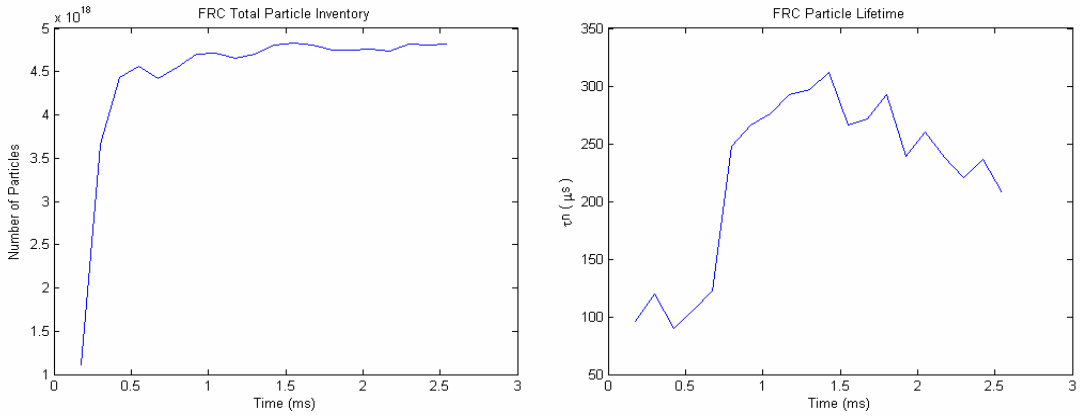

FIG. 6.43 The total particle inventory and the particle lifetime of the 107 kHz odd-parity RMF formed FRC.

The average neutral density has also been calculated for the odd-parity FRC. Its value is noticeably larger than the average neutral density calculated for the even-parity FRC but the average electron density of the odd-parity FRC is much larger than its counterpart for the even-parity case. The resulting average neutral fraction of the odd-parity FRC is also approximately 0.03. The average electron density and calculated average neutral density of the odd-parity FRC is shown in Fig. 6.44.

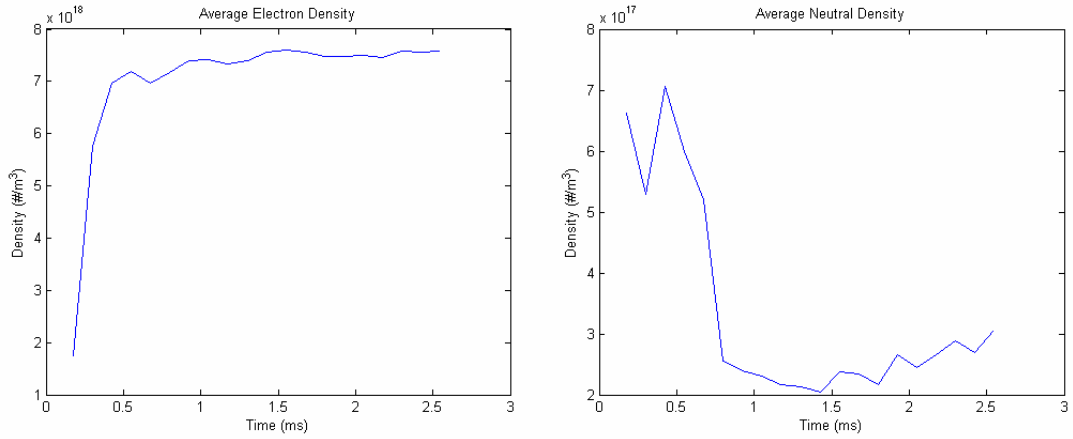

FIG. 6.44 The average electron density and the average neutral density of the 107 kHz odd-parity RMF formed FRC.

The total power loss due to convection for the odd-parity FRC has been calculated and is shown in Fig. 6.45 with the RMF input power. Unfortunately, Langmuir measurements were not taken in the north exhaust jet for the 107 kHz odd-parity RMF formed FRC so the total convection power loss is estimated as double the amount measured in the south exhaust jet. As is the case with the even-parity FRC the total convection power loss from the odd-parity FRC is approximately 25% of the RMF power.

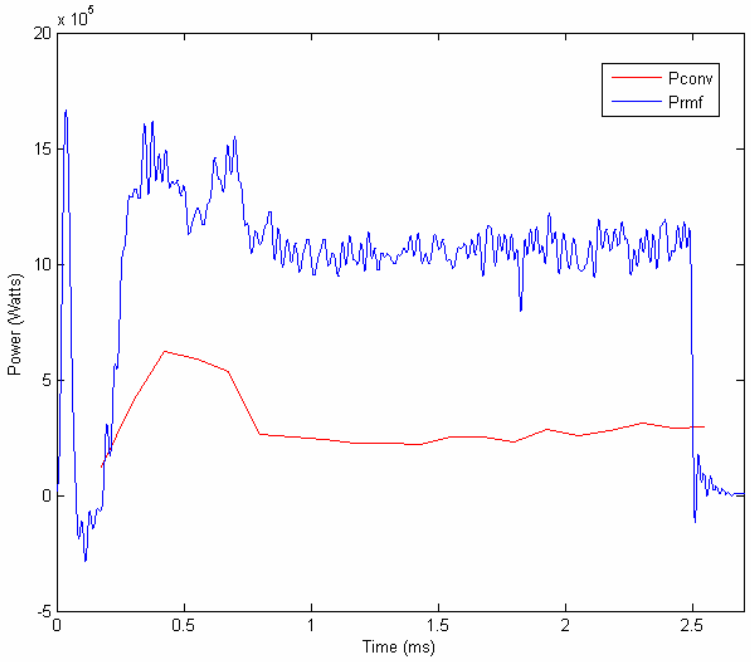

FIG. 6.45 The RMF power and the estimated power loss due to convection for the 107 kHz odd-parity FRC.

Chapter VII: Summary and Conclusions

A combination Langmuir / Mach probe was installed on TCSU and successful measurements were taken at the FRC midplane and in the exhaust jets. The RMF presents a very challenging environment for electric probe measurements and every precaution was taken to minimize noise pickup. An innovative probe design was utilized to minimize the probe's impact on the FRC by ensuring that boron nitride was the only material in contact with the plasma other than the tungsten probe tips. At every point possible the wires leading to the probe tips were shielded with stainless steel inside the vacuum chamber and copper braid outside in an effort to reduce noise.

A radial scan of both the even and odd parity FRCs was completed with the Langmuir probe at the midplane. The bias voltage at the probe tips is continuously swept at 10 kHz to create a time history of the electron temperature and density at each spatial point in the radial scan. In this way a radial profile of the temperature and density were compiled. A discrepancy was noticed in the density profile measured with the Langmuir probe when compared to the density profile calculated from pressure balance which relies on data from the interferometer and the 2-axis internal magnetic probe. Although the peak density value and the average value calculated from the area integral is similar, the density profile from pressure balance displays an outward pressure shift compared to the density profile measured with the Langmuir probe. Multipoint Thomson scattering, which collects data from five radial locations from 10 cm to 25 cm, shows excellent agreement with the Langmuir data indicating that the plasma density profile is less broad than previously thought. Some possible explanations for the discrepancy in the density profiles were examined but the exact reason is yet to be determined.

Successful Langmuir measurements were also made in the exhaust jets of the FRC. With an accurate description of the temperature and most importantly the radial profile of the electron density in the exhaust, some of the interesting dynamics of the

FRC were uncovered. The electron temperature was shown to be uniform throughout the FRC and exhaust while the peak electron density in the exhaust was measured to be approximately 3 or 4 times lower than the average density in the midplane. With the temperature and density profiles and data from the translatable three-axis internal magnetic field probe a pressure balance in the jet was completed to determine the ion temperature. Interestingly it was found to be approximately half the value of the electron temperature. As the ions travel from the scrape-off layer into the exhaust jet they lose energy through adiabatic expansion and unfavorable collisions. The ion flow velocity in the exhaust is calculated and in conjunction with the density profile the particle flow rate in the exhaust is calculated. The total energy of the exhaust jet is calculated by estimating the thermal, kinetic, and ionization energy. This is the FRC power loss due to convection and is approximately 25% of the input power from the RMF.

The particle confinement time of the FRC is also calculated by estimating the total particle inventory from the volume integral of the density profile at the midplane. With the total particle count and the flow rates in the exhaust jets the particle confinement time is calculated as a function of time. The confinement time of approximately 250 μs is likely high since the Langmuir probe can only detect charged particles.

The average neutral density in the FRC is also estimated since the particle outflow rate is equal to the total ionization rate in steady state. The neutral density is calculated to be approximately 3% of the electron density. With the average neutral density the FRC energy lost due to ionization and charge-exchange is calculated. The energy lost due to radiation is also calculated from the pinhole bolometer. Along with the power loss due to convection these major loss channels are shown to account for approximately 50% of the total FRC input power. This would imply that the dominant loss channel is parallel electron conduction along open field lines which intersect the wall. Electron thermal losses appear to be greater for the odd-parity FRC as indicated by the lower electron

temperature, even though odd-parity was formulated to reduce such losses. This is almost certainly caused by additional wall contact produced by the strong B_z oscillation at $z = 0$ cm. Odd-parity operation will only be effective when the value of B_ω/B_e is small, as will be necessary in any case if RMF is to be an efficient current drive mechanism. This, of course requires lower plasma resistivity.

The combination probe measurements in the midplane and especially in the exhaust jet have greatly improved our understanding of power loss in both even and odd-parity RMF formed and sustained FRCs.

BIBLIOGRAPHY

[1] W. M. Stacey, “Fusion: an Introduction to the Physics and Technology of the Magnetic Confinment Fusion”. New York, Wiley (1984).

[2] M. Tuszewski, “Field Reversed Configurations”, Nucl. Fusion **28**, 2033 (1988).

[3] L. C. Steinhauer, “Review of field-reversed configurations”, Phys. Plasmas **18**, 070501 (2011).

[4] J. T. Slough, A. L. Hoffman, R. D. Milroy, R. Maqueda, and L. C. Steinhauer, “Transport, energy balance, and stability of a large field-reversed configuration”, Phys. Plasmas **2**, 2286 (1995)

[5] A.L. Hoffman, *et al* "The Large-S Field-Reversed Configuration Experiment" Fusion Technology **23**, 185 (1993).

[6] H. A. Blevin and P. C. Thonemann, Nucl. Fusion Suppl. Part 1, 55 (1962).

[7] I. R. Jones, "A review of rotating magnetic field current drive and the operation of the rotamak as a field-reversed configuration (Rotamak-FRC) and a spherical tokamak (Rotamak-ST)", Phys. Plasmas **6**, 1950 (1999).

[8] A.L. Hoffman, H.Y. Guo, J.T. Slough, S.J. Tobin, L.S. Schrank, W.A. Reass, and G.A. Wurden, "The TCS rotating magnetic field FRC current-drive experiment", Fusion Science and Technology **41**, 92 (2002).

[9] K.E. Miller, “The Star Thrust Experiment, rotating magnetic field current drive in the field reversed configuration”, Ph.D. Dissertation, University of Washington (2001).

[10] J.A. Grossnickle, “Deep fueling of large tokamaks by field-reversed configuration injection”, Ph.D. Dissertation, University of Washington (2001).

[11] K.E. Miller, et. al., “The TCS upgrade: Design, construction, conditions, and enhanced RMF FRC performance”, Fusion Science and Technology **54**, 948 (2008).

[12] G. Fiksel, A.F. Almagri, D. Craig, M. Iida, S.C. Prager, J.S. Sarff, “High current plasma electron emitter”, Plasma Sources Sci. Technol. **5**, 78 (1996).

[13] D.J. Den Hartog, D.J. Craig, G. Fiksel, J.S. Sarff, “Impurities, temperature and density in a miniature electrostatic plasma and current source”, Plasma Sources Sci. Technol. **6**, 492 (1997).

[14] E.O. Johnson, L. Malter, “A floating double probe method for measurements in gas discharges”, Physical Review **80**, 58 (1950).

[15] I.H. Hutchinson, “Principles of Plasma Diagnostics”, Cambridge University Press (1987).

[16] F.F. Chen, “Electric Probes”, “Plasma Diagnostic Techniques”, Huddlestone (1965).

[17] R.J. Goldston and P.H. Rutherford, “Introduction to Plasma Physics”, Taylor & Francis (1995).

[18] G.R. Votroubek, “Tomographically aided study of field reversed configuration plasma rotation and stability”, Ph.D. Dissertation, University of Washington (2005).

[19] K. Lee, “Development of a Thomson scattering system and its use in a rotating magnetic field driven field-reversed configuration plasma”, Ph.D. Dissertation, University of Washington (2011).

[20] M. Hudis, L.M. Lidsky, “Directional Langmuir probe”, J. Appl. Physics **41**, 5011 (1970).

[21] B.J. Peterson, J.N. Talmadge, D.T. Anderson, F.S.B. Anderson, J.L. Shohet, “Measurement of ion flows using an “unmagnetized” Mach probe in the interchangeable module stellarator”, Rev. Sci. Instrum. **65** (8), (August 1994).

[22] C. L. Deards, “Factors affecting ion spin-up in the Translation, Confinement and Sustainment Upgrade Experiment”, Ph.D. Dissertation, University of Washington (2010).

[23] R.D. Milroy, K.E. Miller, “Edge-driven rotating magnetic field current drive of field-reversed configurations”, Phys. Plasmas **11** 633 (2004).

[24] K.M. Velas, R.D. Milroy, “Probe measurements of the three-dimensional magnetic field structure in a rotating magnetic field sustained field-reversed configuration”, Phys. Plasmas **21**, 012502 (2014).

[25] L.C. Steinhauer, “Electrostatic confinement in the edge layer of field-reversed configurations”, Phys. Fluids **29**, 3379 (1986).

[26] G.C. Vlases, “TCS edge studies”, Grant DE-FG03-01ER-546537, Final Technical Report.

[27] K.M. Velas, “Investigation of the three-dimensional structure of a rotating magnetic field driven field-reversed configuration using internal magnetic field measurements”, Ph.D. Dissertation, University of Washington (2013).

[28] M. Peter, “Paramagnetic spin-up of a field reversed configuration with rotating magnetic field current drive”, Ph.D. Dissertation, University of Washington (2003).

[29] G. S. Voronov, “A practical fit formula for ionization rate coefficients of atoms and ions by electron impact: Z=1-28”, Atomic Data and Nuclear Tables **65** (1997).

[30] R.D. Milroy, C.C. Kim, and C.R. Sovinec, “Extended magnetohydrodynamic simulations of field reversed configuration formation and sustainment with rotating magnetic field current drive”, Phys. Plasmas **17**, 062502 (2010).

[31] W. N. Hugrass, “The Influence of the Spatial Harmonics on the Rotating Magnetic Field Current Drive”, Australian Journal of Physics **39**, 513 (1986).

[32] A.L. Hoffman, “Rotating magnetic field current drive of FRCs subject to equilibrium constraints”, Nucl. Fusion **40**, 1523 (2000).

[33] H.Y. Guo, A. L. Hoffman, and R.D. Milroy, “Rotating magnetic field current drive of high-temperature field reversed configurations with high zeta scaling”, Phys. Plasmas **14**, 112502 (2007).